# Influence of reactive sputtering process parameters on the structure and properties of $TiO_2$ thin films

Von der Fakultät für Mathematik, Informatik und Naturwissenschaften
der Rheinisch-Westfälischen Technischen Hochschule Aachen
zur Erlangung des akademischen Grades einer
Doktorin der Naturwissenschaften genehmigte Dissertation

vorgelegt von

M.Sc. Azza Amin El-Hamshary
aus Kairo/ Ägypten

Berichter: Universitätsprofessor Dr. Matthias Wuttig
Universitätsprofessor Dr. Dieter Mergel

Tag der mündlichen Prüfung: 11.Juli 2011

# *DEDICATION*

*I dedicate this Thesis to,,,*

*My Father,*

*My Mother,*

*All My Family,*

*Soul of 25 January revolution martyrs, and*

*My entire lovely persons in this world.*

# Contents

# CONTENTS

# 1

# Introduction

A thin film is a layer of material with a thickness ranging from a fraction of a nanometre to several micrometers. Thin film technology plays an important role in our modern live. This importance originates from their wide range of application. Thin film technology enables devices such as solar cells, smart and architectural windows, surface protection, data storage, decorative and wear resistance coatings, optical and microelectronic devices [1]. It has been observed that the required applications rely strongly on the properties of the thin film materials and their properties depend on the deposition processes used. Therefore, understanding the growth mechanism of the different thin film materials has been the inspiration of many research activities [2].

Recently, titanium dioxide ($TiO_2$) thin films have attracted a significant attention and became a major area of research since the discovery of its photocatalytic effect of water [3]. $TiO_2$ is a wide band gap oxide which is characterized by high chemical stability, mechanical hardness and optical transmittance as well as high refractive index. Therefore it is used in a variety of applications including solar energy conversion [4] optical coatings [5] and protective layers [6, 7]. $TiO_2$ thin films can crystallize in two crystalline structures, anatase and rutile [8], anatase is metastable at room temperature while rutile is the thermodynamically stable phase. Each phase is characterized by its physical properties and the related applications. For example, the rutile phase is known for its comparatively high mass density (4.23 $g/cm^3$) [9] and in comparison to other common metal oxides, high refractive index of up to 2.75 at 589 nm [9]. Hence, it is highly desirable for applications e.g. the fabrication of antireflective coatings [10, 11, 12]. The anatase phase in turn is characterized by a very pronounced photocatalytic activity [13, 14] in combination with small water contact angles (hydrophilicity). Consequently, it is applied to fabricate self-cleaning [14, 15], antifogging glass [14] and antibacterial surfaces [14]. It is also used in the purification of water and air through the photolysis of organic and toxic compounds [3].

Many deposition techniques such as sol-gel processes [16], chemical vapour deposition [17], evaporation [18], ion beam assisted deposition [19, 20] and sputter deposition [21, 22] have already been employed to deposit $TiO_2$ thin films. Among these techniques sputter deposition is favoured for a number of reasons. Sputtering is one of the most widely used techniques for preparing compound thin films. It is especially favoured by the large area coating industry because of the excellent scalability of the process, low process temperature and deposition of adhesive and homogeneous films. The capability of controlling film properties and stoichiometry during growth as well as a relative high deposition rate are other attractive features of this technique.

Numerous prior efforts [23-38] have been performed to investigate the structure formation of $TiO_2$ thin films as a function of various deposition parameters such as e.g. total pressure, oxygen partial pressure, substrate temperature, deposition rate and film thickness. These efforts were mainly driven by the interest to apply such films as photocatalysts. It has been demonstrated from these studies that the structure is strongly dependent on the process parameters. For instance, the energetic particle bombardment is one of the most important parameters governing thin film phase formation. However, the nature of the bombarding species and the mechanism of phase formation as a function of bombardment have not yet been investigated. Moreover, little attention has been given to understand the growth mechanism of such films and the reasons why these different phases are formed is poorly understood. Nevertheless, controlling the film structure due to the targeted application is the essential motivation to understand the correlation between different sputtering process parameters and the structure formation of such films. Therefore, this work aims to clarify the growth mechanism of $TiO_2$ thin films prepared by reactive sputtering. This work aims also to draw a conclusion on the influence of the various fundamental process parameters on the structure and the photo-induced properties of such films.

In line with these aims, some of the applications as well as the required properties of $TiO_2$ thin films are described in chapter 2. A literature review on the influence of different process parameters on the structure of $TiO_2$ thin films is presented; in addition the photoconductive properties of such films are reviewed.

In chapter 3, an overview on the theory of sputter deposition and the high power pulsed magnetron sputtering are presented. Also a background on the growth mechanism of thin films as well as the influence of impacting energetic particles (ion bombardment) on the film growth during sputtering is reported. As the formation of residual stress in the film is a consequence of the bombardment; therefore an overview on the residual stress mechanism and some of the stress models are also introduced.

In chapter 4, the experimental techniques used in the fabrication of $TiO_2$ thin films are described. The principle of various techniques utilized to investigate the morphology and structure of the thin films fabricated such as atomic force microscopy, transmission electron microscopy and grazing incidence x- ray diffraction are presented. Additionally, the determination of the residual stress in the sputtered films by means of waver curvature method is described. Finally, the photoconductivity technique which is employed to study the interaction of the film surface with light is introduced.

In chapter 5, the preparation of $TiO_2$ thin films and the investigation of the structure and topography of such films under the influence of the energetic particles by using ion beam assisted sputtering is presented. The effect of target aging on the film structure is also demonstrated. Additionally, the evaluation of film structure by utilizing high power pulse sputtering and the effect of post annealing on the structure of the bombarded films are discussed. At the end, the development of the residual stress in the fabricated films as a function of the different deposition parameters is introduced.

Chapter 6 starts by presenting the influence of the fundamental process parameters (oxygen partial pressure, film thickness) on the structure and morphology of the reactively sputtered $TiO_2$ films. Then the investigation of the microstructure and the homogeneity of such films are described. At the end, a model is proposed which describes the growth mechanism of $TiO_2$ films upon variation of the sputtering process.

In chapter 7, investigations of the photoconductive properties of $TiO_2$ films with different structure at different ambient conditions are discussed. Finally, a summary and outlook of this work are given.

# 2

# Titanium dioxide- properties and applications

Titanium dioxide (often also referred to as "titania") is a naturally occurring oxide of titanium, chemical formula is $TiO_2$. It exhibits some interesting properties and is therefore one of the most widely used materials in many application areas. In this chapter, an overview on the most important physical properties of $TiO_2$ and the resulting applications are presented. Additionally, a literature survey of the influence of the deposition parameters on the structure of $TiO_2$ thin films and of the photoconductive properties of such films is provided.

## 2.1 Applications and properties

Titanium dioxide ($TiO_2$) is chemically inert and occurs in three different crystal forms: anatase, rutile and brookite. The rutile structure (110) is the thermodynamically stable phase for particles above 35 nm in size. The (110) face is quite low in energy and most stable than the other rutile faces (100) and (001). Anatase (101) is the most stable phase for nanoparticles below 11 nm. The (101) face is a low energy surface and is the most prevalent face for anatase nanocrystals. The brookite which is rare and difficult to prepare has been found to be the most stable phase for nanoparticles in the 11-35 nm range [39]. $TiO_2$ thin films exhibit only these two crystalline structures, anatase and rutile upon sputter deposition. These phases are well distinguishable in terms of their physical properties.

The structure of rutile and anatase can be described in terms of chains of $TiO_6$ octahedral. The two crystal structures differ by the distortion of each octahedron and by the assembly pattern of the octahedral chains. A titanium atom is octahedrally coordinated by six oxygen atoms. In the rutile structure each octahedron is in contact with 10 neighbor octahedrons (two sharing edge oxygen pairs and eight sharing corner oxygen atoms), while in the anatase structure each octahedron is in contact with eight neighbors (four sharing an edge and four sharing a corner). These differences in lattice structures cause different mass densities and electronic band structures between the two forms of $TiO_2$. The unit cell structures of the anatase and rutile crystal are illustrated in figure 2.1 (a, b) respectively.

The d $_{Ti-Ti}$ distance in anatase is longer whereas the $d_{Ti-O}$ distance is shorter than in rutile. Moreover, rutile is the high temperature and stable phase, it has a higher index of refraction up to 2.75 at 589 nm, high mass density (4.23 gm/cm$^3$) [9] and lower band gap than anatase. On the other hand, the anatase phase is a low-temperature polymorph and characterized by a very pronounced photocatalytic activity [13] in combination with small water contact angles (hydrophilicity). A transformation from anatase to rutile can be thermally induced at temperatures above 800 °C [8]. Some of the physical properties of anatase and rutile crystal structures of $TiO_2$ are summarized in table 1.

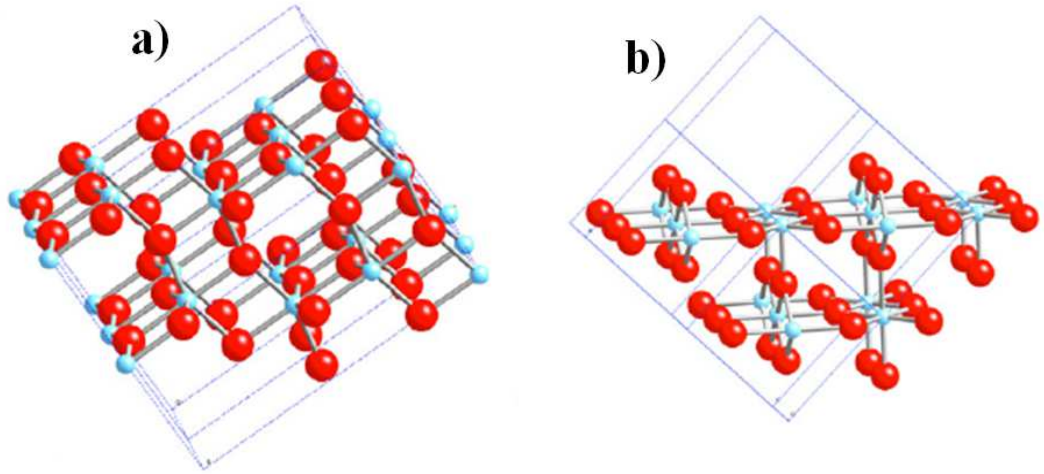

**Figure 2.1:** Crystal structure of a) anatase (101) and b) rutile (110) [14].

| Properties | Anatase | rutile |
|---|---|---|
| Energy gap $E_g$ | 3.3 eV | 3.0 eV |
| Mass density ρ | 3.894 g/cm$^3$ | 4.23 g/cm$^3$ |
| Refractive index n | 2.55 | 2.75 |
| $d_{Ti-Ti}$ | 3.79/3.04 Å | 3.57/2.96 Å |
| $d_{Ti-O}$ | 1.934/1.980 Å | 1.949/1.980 Å |

**Table 1:** Some of the physical properties of anatase and rutile $TiO_2$ structures.

Due to the different physical properties of these two states, $TiO_2$ thin films are employed in a wide range of applications. The anatase phase appears to be the most photoactive and the most practical for widespread environmental applications such as water purification, wastewater treatment, hazardous waste control, air purification, and water disinfection [40].

As mentioned in the introduction, it is also applied to fabricate self-cleaning [14, 15] and antibacterial surfaces [14]. Optical coatings also profit from the wetting behavior of the film which results in an anti-fogging effect [14]. Applications for the rutile structure comprise e.g., the fabrication of antireflective coatings [10, 11, 12] due to its high refractive index. It is evident that the precise control of the film structure is a key requirement to tailor the performance of the film for the targeted application. Therefore, structure control presently constitutes one of the main challenges in the design of adequate coating processes.

## 2.2 Correlation: structure and deposition parameters

During the last decade significant endeavors have been made to understand the structure formation of sputtered $TiO_2$ thin films. These efforts were mainly driven by the interest to apply such films as photocatalysts. Special emphasis has been put on understanding the correlation between process parameters and the formation of the anatase and rutile phases in thin films. Consequently, a large number of studies have been published that investigate structure formation as a function of various deposition parameters such as total pressure, oxygen partial pressure, substrate temperature, film thickness, magnetron configuration and electrical discharge properties including the ion bombardment of the substrate. These parameters can be defined in four main categories: oxygen flow, film thickness, heating temperature and energetic particles. A summary of the most significant findings of these studies will be provided in this section.

### 2.2.1 Growth of $TiO_2$ thin films upon variation of oxygen flow

Various studies [21, 24, 41, 42] have been concerned with the investigation of the structure of $TiO_2$ thin films upon variation of the oxygen content in the deposition process. The films have been fabricated by means of different deposition techniques on unheated substrate, for example by reactive dcMS in [21], reactive r.f. magnetron sputtering [24] and pulsed dcMS [41]. All investigations show that the rutile phase is the dominant phase at lower oxygen partial pressure. The formation of the anatase structure was found to be preferential at higher oxygen partial pressure.

It has been also observed that the anatase phase is formed at higher total sputtering pressures and exhibits a decline in the crystallinity with increasing the pressure or decreasing the (oxygen/total pressure $p_{O2}/p_t$) ratio [21, 24, 41]. This has been attributed to the action of the energy delivered to the growing film [21, 24, 41] in addition to the surface temperature [21]. The formation of rutile at lower pressure and low oxygen partial pressure is attributed to the higher activation energy for the formation of the rutile than the anatase phase. The formation of pure anatase at higher pressures is explained by the loss of ion energy and therefore to a loss of energy necessary to form a high- energy rutile phase [41]. However, the authors have not discussed the exact mechanism of phase formation as a function of increasing the oxygen partial pressure or the nature of bombarding species which influence the growing film.

Further findings: the crystallinity of the films shows improvements upon decreasing the target- substrate distances which has been explained by an increase of the substrate surface temperature [21].

The influence of the total pressure on the microstructure and surface morphology has been studied by SEM (secondary electron microscopy) [24]. All films revealed a columnar microstructure. At low total pressure, relatively dense surfaces with surface particles of polygonal shape are formed. More open surfaces with a lower density, a higher roughness and blocks of surface particles separated by deep voids are the features of the films which have been deposited at higher total pressures. The structure variation of $TiO_2$ thin films as a function of the oxygen ratio and total pressure has been described in a phase diagram, figure 2.2 [24].

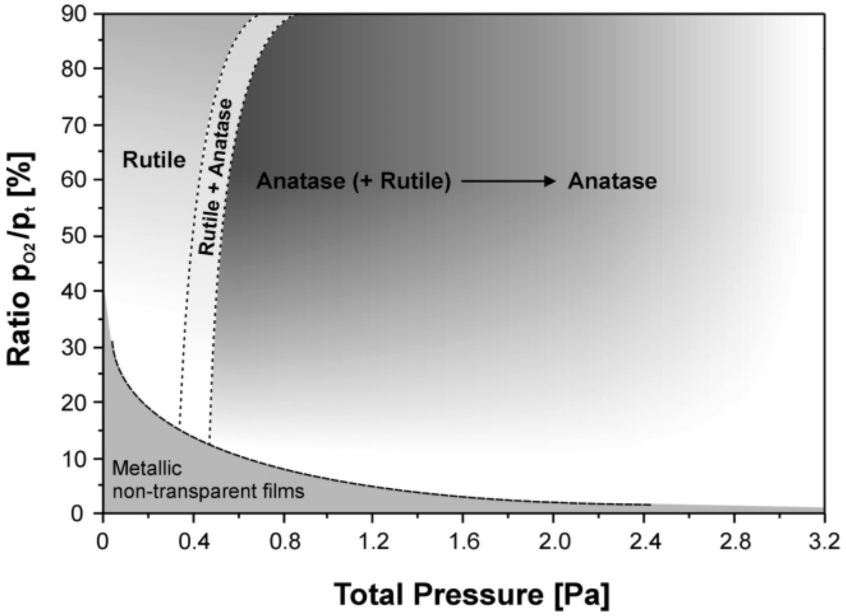

**Figure 2.2:** Schematic phase diagram for reactive r.f. magnetron sputtering of the $TiO_2$ films on unheated substrate as established by Zeman [24].

### 2.2.2 Film thickness parameter

The effect of the film thickness on the structure formation of $TiO_2$ thin films has been examined [21, 25, 26, 27, 41, 43]. The investigations have been carried out applying different deposition techniques and at different deposition conditions. For example, the films were deposited by r.f magnetron sputtering with variable thickness ranging from 70-950 nm at two different pressures of 0.92 and 2.77 Pa [25]. In [26, 27, 43], a series of nanocrystalline films (100 to 2000 nm) have been deposited by reactive bipolar pulsed dcMS on unheated substrates. All studies show that the formation of the anatase phase is improved upon increasing film thickness. This has been explained by increasing the substrate temperature and the energy delivered to the growing film at higher thickness [21].

A gradual conversion of the structure from an amorphous phase close to the substrate at low thickness, to a mixture of rutile and anatase and then a pure anatase film at higher thickness has been observed [41]. The authors attributed the structure conversion only to the energy delivered during growth and not to an increasing substrate surface temperature. They have found that interrupting the deposition every 30 minutes followed by cooling down the substrate surface results in the same film structure as without interruption. This means that the substrate temperature has no effect on the structure formation of thick films.

An investigation of thickness series (100-2000 nm) at constant oxygen partial pressure ($P_{O2}$ = 0.15 Pa) shows that the thin film has a rutile structure while formation of an anatase phase is favored at higher thickness [26]. The authors assumed that rutile grows directly at the substrate interface and is replaced by anatase with increasing distance from the substrate. An XRD scan at several small angles of incidence reveal that the rutile peak is nearly absent for the smallest angles of incidence and is increasing with higher penetration depth. Grain sizes of 6-7 and 10 nm have been estimated for the rutile and the anatase phase respectively.

Annealing of these samples in air at temperatures from 200 to 1000 °C shows no change in the crystallinity up to 600-700°C [27]. Then the transformation of anatase into rutile has been observed at annealing temperature of 800 °C and higher. The authors didn’t draw any relevant conclusions from these results.

Moreover, deposition of thickness series (54 to 2000 nm) at low sputtering pressure of 0.5 Pa and low oxygen partial pressure of 0.03 Pa resulted in amorphous films [43]. Crystallization of the anatase phase has been observed upon annealing in air at 350°C for thinner films of 54 and 100 nm. The crystallite sizes deduced by the Williamson-Hall method indicate crystallite sizes of more than 100 nm for the thin and more than 300 nm for the thick films. The films show tensile stress in all direction with average values of several hundred MPa estimated with an isotropic elastic modulus tensor. Upon annealing to 500°C, stresses disappeared in films with thicknesses above 800 nm.

However, all studies haven't drawn any clear conclusion on the mechanism of structure variation upon increasing the film thickness. Also there are no comprehensive investigations of the surface topography as a function of film thickness.

### 2.2.3 Substrate temperature

It has been found [32, 33, 44, 45] that the substrate heating has a strong effect on the structure of $TiO_2$ thin films. These investigations exhibited that the anatase phase is preferentially formed upon increasing substrate temperature. For example, all films deposited [44] at ambient temperature as well as with increasing of the substrate temperature to 500°C consist of anatase structure. At low temperature the film shows a preferred orientation in the (101) direction and non-uniformity as observed from the SEM images. The preferred orientation changed to the (004) direction normal to the substrate and the uniformity of the film is improved with increasing the substrate temperature above 450°C.

On the other hand, films deposited either by vacuum arc plasma evaporation (VAPE) or reactive dcMS show an amorphous phase with no surface features at room temperature [33, 45]. Upon increasing the substrate temperature to 300°C and more, crystallization of the anatase phase with large surface features and roughness has been observed [33]. Moreover, the formation of the anatase phase with typical surface features in the SEM images has also been obtained upon increasing the substrate temperature to 140° and 220°C [45]. The authors concluded that increasing the temperature leads to an increase of the crystalline grain size. This is explained by the reaction of the sputtered Ti particles with the oxygen atoms on the substrate due to the thermal effect [45].

Furthermore, they [32] have investigated the film structure as a function of substrate temperature (150 and 250°C) in addition to ion assisted deposition at two different ion energies (150 and 300 eV). These results show that formation of rutile is favored at high energetic ion bombardment even with substrate heating, while the anatase phase is preferentially formed at the conditions where is no bombardment or high substrate temperature. This indicates that the influence of substrate temperature on the structure vanished in the presence of high ion bombardment. Also ion bombardment leads to the generation of compressive stress in the film.

- At low substrate temperature (150°) without bombardment, the film structure exhibits anatase with a small rutile portion. With ion assistance of low kinetic energy (150 eV), an amorphous phase with very few crystallites in the matrix is formed. Higher kinetic energy of 300 eV leads to a similar structure with more single rutile crystallites in the amorphous matrix.
- At high substrate temperature (250°C) without ion assistance, the film possesses an anatase phase comprised of small grains of 10 nm and the structure is fibrous columnar. The anatase grains grow with 20 nm grain size and the crystallinity improves largely at low kinetic energy (150 eV). The film exhibits a mountain-like weakly crystallized bottom layer followed by rutile crystallites at later stages of film growth at higher kinetic energy (300 eV). This means that increased ion assistance changes the structure from anatase to rutile.
- No explanation is given for the formation of rutile structure at higher ion bombardment and for the strange interlayer at the substrate surface

## 2.2.4 Energetic particles

Different methods have been utilized to examine the role of energetic particles on the structure formation of $TiO_2$ thin films, such as; using different magnetron configuration [29, 30, 31], ion bombardment [23, 36, 37], and HiPIMS [38, 46, 47]. Some of these investigations will be summarized in this section.

### 1.Different magnetron configuration

The $TiO_2$ thin films have been deposited utilizing balanced and unbalanced magnetrons and at variable magnetic field strength of 150-1000G at different gas pressures of 1.0 or 3.0 Pa [29]. The plasma being directed onto the substrate surface and low–ion energy ion bombardment of the growing film is obtained using an unbalanced magnetron. It has been found that the crystallinity of the films improved with increasing the magnetic field strength due to the decreasing the target voltage. Moreover, better crystallinity (highly anatase structure) is obtained using UBM. The authors attributed that to the increased low energy $Ar^+$ bombardment due to the self-bias. SEM images show that the difference in the surface topography (rutile and anatase) is attributed to the secondary nucleation rate which is assumed to be higher for the rutile films due to the massive oxygen ion bombardment. The secondary nucleation is the formation of new crystals in the presence of crystals of the same nature ("parents"). The secondary nucleation rate depends on the properties of the "parent" crystals.

Moreover, intensification of the magnetic field strength at the target surface to 5000 G by using an auxiliary permanent magnet behind the substrate has been explored [31]. The ion energy was measured to be about 50 eV as compared to 25 eV for non-modified process. It has been observed that at low and high pressure, the rutile phase is dominant in the modified sputtering process, while polycrystalline anatase films grow in conventional sputtering at high pressure and disappeared at low pressure. The surface morphology images show two different types of features (anatase and rutile grains) with different sizes and are consistent with the XRD pattern. The growth of a non-stoichimoetric (Oxygen 1.9) rutile structure has been attributed to the intense Ar ion bombardment which leads to oxygen vacancies.

These investigations show that the rutile phase is energetically favored at high ion bombardment. However, this has been attributed to the action of Ar species and the negative oxygen ions are not considered. The influence of negative oxygen ions on the structure has been shown for a variety of materials [51-53], but it is often disregarded in the structure formation of sputtered $TiO_2$ films.

## 2.Ion bombardment

The effect of ion bombardment on the structure of $TiO_2$ films has been investigated by different methods, e.g. deposition using dc dual magnetron sputtering with high frequency [23] and by simultaneous bombardment with oxygen ions using an auxiliary electron cyclotron resonance (ECR) [36]. Both studies show that increasing the ion bombardment and thereby the energy delivered to the growing film leads to a superior rutile phase. Deterioration of the structure is observed upon increasing the bombardment.

These results can be summarized as follows [23]:

- The authors stated that there are several sources of energy impact onto the growing film: 1) substrate temperature, 2) ion bombardment, 3) heating by the magnetron, 4) heating by chemical reactions during film formation and 5) radiative heating by the plasma.
- The energy delivered to the film is inversely proportional to the deposition rate and proportional to the ion current density at the substrate, i.e. heating depends on the relative arrival ratio of ions to film particles. They stated that this is the reason for the formation of an amorphous structure in the transition regime due to the high rate.
- An increased ion bombardment is achieved by sputtering with high frequency, since the plasma buildup regime dominates the discharge and higher electron temperatures are achieved. However, they only consider in this case the bombardment by positive ions of

low energy which are accelerated near the substrate as the target voltage is also significantly increased during plasma ignition. Hence, I suppose that the energy of the impinging negative oxygen ions is also higher.

- Deterioration of the structure is observed by increasing the pulse frequency and hence the ion bombardment. As a conclusion, the authors attributed the increase of the ion bombardment to an increase of the electron temperature. I believe, however, that increase the energy of the negative oxygen ions is the main reason.

Additionally, simultaneous bombardment of reactively evaporated $TiO_2$ thin films by oxygen ions reveals also the formation of the rutile phase [36]. The peak intensity of the rutile phase increases with increasing bombardment (flux or ion energy). Bombardment by argon ions also promotes the growth of the rutile phase. However, the rutile peak is much weaker as compared with oxygen ion bombardment. This is in line with our results.

Furthermore, Löbel et al [37] have attributed the nucleation of rutile to increasing the process energy (electron and ion bombardment) and the presence of Ti in the vapor phase.

## 3.HiPIMS.

High power impulse magnetron sputtering is characterized by high plasma densities and high ionization of sputtered ions. Consequently, the negative oxygen ions on the target surface have a high kinetic energy. Therefore, HiPIMS is another suitable technique to illustrate the role of energetic particles on the film structure. This technique has been utilized to investigate the structure of $TiO_2$ thin films [e.g. 38, 46, 47]. It has been observed that HiPIMS leads to a superior rutile phase due to the large electron flux reaching the substrate [47].

For example, Stranak et al. [38, 46] have studied the crystallographic and morphological properties of $TiO_2$ thin films prepared by HiPIMS at low substrate temperatures (<65°C). It was deduced from probe measurements that the mean (averaged over the pulse) electron energy decreased and the mean electron density increased with increasing the total pressure. At low sputtering pressure, a pure rutile film is deposited while the anatase phase is solely present at high pressures when the films are very thin (20 to 40 nm). Intermediate pressures yield mixed films. As mentioned before, increasing the sputtering pressure reduces the energy delivered to the growing film and thereby increases the film roughness. The authors assumed that the energetic impact is the main driving force for the phase formation at different pressures. However, the existence of negative oxygen ions is not considered.

## 4. Other investigations

Examination of the nature and the energy distribution of positive and negative ions impinging on the growing $TiO_2$ film as a function of sputtering pressure has been done by Martin et al. [34]. They have found that the flux of positive ions simply decreases when the total pressure increases, whereas the energy distribution remains rather unchanged. In contrast, the flux of negative oxygen ions (low energy) increases with increasing pressure and the mean energy increases as well (18 to 26 eV). A mixed anatase/rutile structure is observed at the lowest pressure while for the higher pressure only anatase films are deposited. The author attributed the structure formation to the action of positive ion bombardment.

A similar structure behavior is also presented by variation of the total working pressure from 0.3 to 1.0 and 3.0 Pa [28]. The authors in this case attributed the formation of a rutile phase at low pressure to the presence of $Ti^+$ and $O_2^+$ species in the plasma process. However, there is no proof for the presence of high energetic electrons which required ionizing these species. They also argued that the high energetic particles impinge on the growing film surface at lower pressures play a role in the formation of rutile. The AFM images show large grains in the film surface for all pressures. Increasing the pressure leads to a change from simple to more complicated features with sub-structures. They assumed that high energy particles bombardment (reflected Ar neutrals and negative oxygen ions) are responsible for the structural variations at different pressures.

The crystal structure and microstructure of $TiO_2$ thin films have been investigated with a variation of the pulse mode (unipolar and bipolar) [35]. All films were amorphous with a columnar microstructure and a rough surface at 7 kW in unipolar and bipolar modes and at 1 Pa. Crystalline films are formed with increasing the sputtering power to 10 kW (both modes) at a pressure of 0.5 Pa. However, the unipolar mode yields highly anatase films while the bipolar mode yields purely rutile structures.

Microstructure: TEM images show amorphous layers of about 200 nm at the substrate interface for both films (anatase and rutile). The rutile films exhibit a much larger dislocation density than the anatase films while the lateral grain sizes are similar. It is concluded that the high dislocation density is responsible for the broad XRD peaks of rutile instead of a small grain size. They attributed the formation of rutile in bipolar mode to the high plasma density in the vicinity of the substrate for this mode. This leads to an increase in energetic particles bombardment. As in other studies, the type of the bombarding species has not been identified.

Also the formation of a crystalline film on the initially amorphous interlayer is explained by an increase of the substrate temperature during deposition.

To sum up, we can conclude from these studies that all process parameters have a significant influence on the structure formation of $TiO_2$ thin films as presented in table 2. The formation of the anatase phase is preferentially favored at high oxygen content as well as large film thicknesses. It also benefits from increasing the substrate temperature and the low energetic bombardment. On the other hand, the rutile phase seems to be enhanced by the energetic particles bombardment during film growth. Several interpretations have been given to explain this structural behavior as a function of the different process parameters.

However, regarding the action of energetic particle bombardment on the phase formation, there is no clear conclusion on the nature of the bombarding species, their respective energies and finally on the exact mechanism of phase formation as a function of particle bombardment. Most of the published works do not at all take into account the action of negative oxygen ions. The growth mechanism of the $TiO_2$ thin films as a function of the oxygen flow and film thickness is not completely discussed. Moreover, little attention has been given to investigate the surface topography and the microstructure as a function of these parameters. Therefore, the mechanism of the structure formation is not completely understood.

| Parameter | Structure | Interpretation |
|---|---|---|
| Low oxygen flow/ low sputter pressure | Rutile | The higher activation energy of the rutile than the anatase phase [21, 24, 41] |
| High oxygen flow/ high sputter pressure | Anatase | The loss of ion energy delivered to the growing film at high pressure [21, 24, 41] |
| Thick films | Anatase [21, 25, 26, 27, 41, 43] | Increasing the substrate temperature and the energy delivered to the growing film [21] |
| Substrate temperature up to 300°C | Anatase [32, 33, 45] | The reaction of the sputtered Ti particles with the oxygen atoms on the substrate due to thermal effect [45] |
| High ion bombardment | Rutile [23, 36, 37] | Bombardment by Ar ions [31, 36] |
| HiPIMS | Rutile [38, 46, 47] | The large electron flux reaching the substrate [47] |

**Table 2: The influence of the various process parameters on the structure of $TiO_2$ thin film as summarized from the literature.**

## 2.3 Photo-induced properties

Due to the wide application field of $TiO_2$ thin films as a photocatalyst, the photocatalytic activity of this material has been investigated by different methods. For instance, the degradation of acetaldehyde with time ($CH_3CHO$) upon UV illumination [29] and the decomposition of methylene blue ($C_{16}H_{18}N_3S\cdot Cl\cdot 3H_2O$) dye solution have been measured [51]. The photo- induced hydrophilicity of $TiO_2$ thin films was also evaluated through measurement of contact angles for pure water after UV illumination [28]. All investigations have shown that the anatase phase has a higher activity than the rutile phase. The reason is that the bottom energy of conduction band of anatase is about 0.2 eV higher than the rutile phase, so the photo-generated electrons in the conduction band of anatase have a higher energy [52]. On the other hand, few studies [53-59] have been concerned with the investigation of the photoconductive properties of such films at different ambient conditions. Hence, the correlation between the structure variations of $TiO_2$ thin films and the photoconductive properties has not been discovered yet. In this section, some of these efforts will be summarized.

### 2.3.1 Photoconductivity

The photoconductive properties of $TiO_2$ thin films show a strong dependence on the ambient atmosphere. In [53, 54], the photoconductive measurements have been carried out in vacuum and air as a function of on-off illumination periods. It has been observed that the photoconductivity in vacuum is much larger than in air. The photoconductivity shows a sudden increment to a maximum and then falls down to a steady state in air as the light is switched on and off. On the contrary, in vacuum the increase is slow and no saturation is observed even for long time exposure. The authors attributed the difference of photoconductivity in vacuum and air to the loss of surface adsorbed oxygen. i.e. removal of conduction electrons by adsorbed $O_2$, the adsorbed oxygen captures electrons from the bulk and creates negatively charged $O^{2-}$ ions. Due to the low concentration of $O_2$ in vacuum, the electron removal rate is low and a large photoconductivity is observed. On the other hand, the removal rate is higher in air and thereby the photoconductivity is low.

Investigations of the photoconductivity of nanocrystalline anatase films show similar results [54]. The dark conductivity has also been measured and shows a low value in vacuum. This has been attributed to the removal of water which adsorbs on the $TiO_2$ surface and leads to formation of $Ti^{+3}$. Regarding the photoconductivity, the authors argue that there are two mechanisms affecting the PC behaviour; surface adsorbed oxygen as explained in [53] and electron-hole recombination by surface hydroxyl groups. They have also observed that the trapping mechanism has an effect on the photoconductivity in vacuum. Therefore, the variation of the photoconductivity as a function of the ambient atmosphere has been attributed to the competition between photo-generation, recombination and trapping mechanisms. Moreover, the second cycle of illumination is attributed to the residual occupancy of traps from the first cycle. Increasing the light intensity leads to an increase of the photogeneration rate and a high trapping rate. Also, the decay of photoconductivity is explained by electron-hole recombination. They have constructed a model which explains the behavior of the photoconductivity in terms of adsorbed oxygen coverage in addition to the hole trapping mechanism. Other mechanisms have been also included as illustrated in figure 2.3.

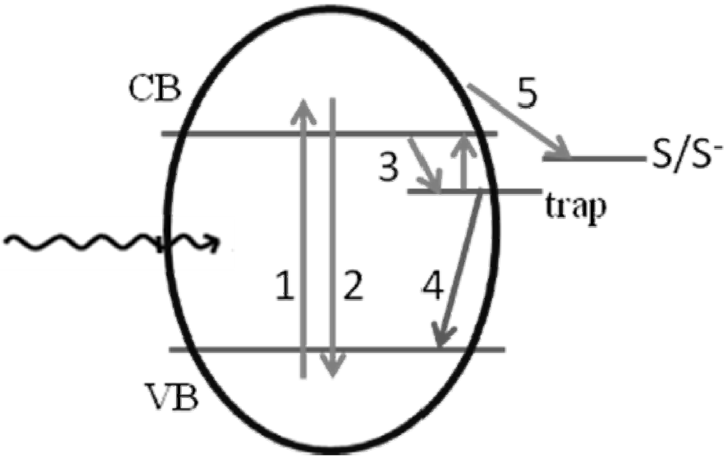

**Figure 2.3:** Photoconductivity model. The diagram represents the energy level of the trap state and an electron scavenger state S/S$^-$ on the surface. The arrows represent the different possible electron transitions. (1) photogeneration, (2) band-to-band recombination, (3) electron trapping, (4) hole trapping, (5) electron scavenging [53].

Several studies have been carried out by Golego et al. on the photoconductivity of $TiO_2$ thin films deposited at different conditions [55-58]. For example, they have investigated the photoconductivity of polycrystalline anatase films (0.7 μm thickness) and $Nb_xTi_{1-x}O_2$ as a function of ambient conditions, light intensity and temperature [55]. The results can be summarized in several points:

- The dark conductivity is explained by trapping holes; the photoconductivity in this model is attributed to the excess of free electrons.
- The dark conductivity shows a difference according to the ambient atmosphere; in oxygen, air and argon it was determined to$1*10^{-8}$, $5*10^{-8}$ and $7*10^{-7}$ $(\Omega cm)^{-1}$ respectively. This has been explained by a loss of adsorbed surface oxygen.
- They observed that the photoconductivity increases (when the ambient is changed from air to argon) due to change of the surface oxygen coverage.
- The decay in the dark conductivity was determined by the surface barrier height, which increased with time due to increasing the negative charge as the electron trapped at $O_2$ (ads).

- ➢ Increasing the temperature at constant light intensity leads to a decrease of the conductivity. This has been explained by increasing the energy barrier due to an increasing electron density.
- ➢ The higher the light intensity, the faster the saturation of the photoconductivity; in addition, an increase of the electron-hole pair generation and the hole trapping rate are observed. As the light intensity decreases, the surface charge decreases and as a result, the surface barrier is large.

Moreover, they have presented in [56] that changing the atmosphere from oxygen to argon leads to a decrease of the photoconductivity. The photoconductivity returns to the original value upon introducing argon again. Upon replacing the argon by oxygen for the second cycle, the drop in the photoconductivity was faster than the first cycle as shown in figure 2.4. They attributed this variation to the probability of photoannealing of oxygen surface defects during the first illumination cycle. i.e. illumination in presence of oxygen leads to incorporation of oxygen into the oxygen vacancies at the surface. They have also observed that the magnitude of the photoconductivity is proportional to the square root of light intensity. i.e. the total electron density that corresponded to the steady-state photoconductivity condition increased and no saturation of the steady-state photoconductivity was observed over the whole range of intensity.

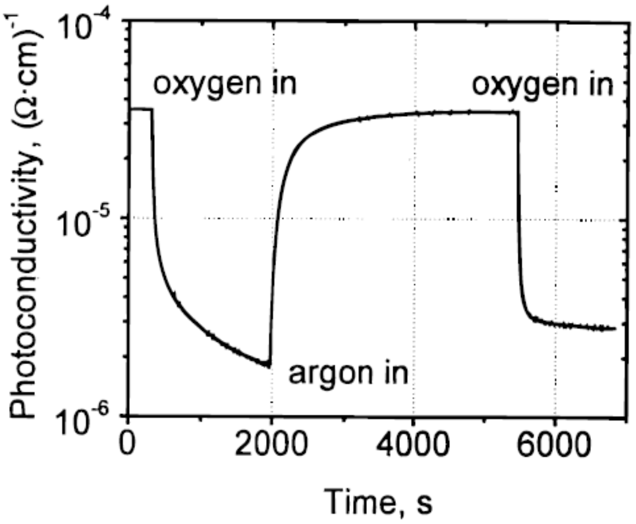

**Figure 2.4:** Sensor response of steady-state photoconductivity in thin-film $TiO_2$ containing 10 atom % Nb under 1780 W/m$^2$ white-light illumination at 120° C [56].

Furthermore, the thermally stimulated current (TSC) was measured to obtain information about the trap levels in the $TiO_2$ thin films by Takeuchi [59]. TSC was measured as a function of temperature after irradiation the sample for 30 min. These measurements show the existence of trapping levels in the $TiO_2$ films, some of these levels are considered to be assigned to structural defects associated with oxygen vacancies. They have also found that the concentration of these defects decreases with increasing the oxygen concentration in the sputtering gas.

To conclude, all studies have focused on investigation of the photoconductivity of the $TiO_2$ films as a function of the ambient atmosphere. However, no attention has been given to perform the photoconductivity measurements on $TiO_2$ thin films with different structures.

# 3

# Sputter deposition and film growth

In the course of this work, the sputtering technique has been employed to fabricate $TiO_2$ thin films. Therefore, an overview on the sputtering technique will be provided in this chapter. Background information on the thin film growth mechanism and the role of energetic particles during the film growth will be given. Moreover a summary of the proposed theories which discuss the origin of the residual stress generated during film deposition is presented.

## 3.1 Sputtering process

### 3.1.1 Concept of sputtering

Sputtering is a process whereby portions of a coating material (target) are ejected through bombardment by energetic species, i.e. if ions impinge on the target, it causes ejection of target atoms and condensation on a substrate to form a thin film. The rate of the material leaving the target depends on the number of the bombarding ions. Therefore it is desirable to increase the plasma density in front of the sputtering source. Other interactions can also occur due to the bombardment (figure 3.1). Some of these interactions are:

(i) Secondary electrons, (ii) reflected ions and neutral species at the target surface, (iii) implantation ions, with buried ions under the target surface, and (iv) rearrangement of the target structure and also electromagnetic radiation.

Each of these interactions depends on the type of ions (mass, charge), the nature of the surface atoms, and on the ion energy.

Moreover, sputtering can be defined as a non-thermal vaporization process where surface atoms are physically ejected from a solid surface by momentum transfer from an atomic-sized energetic bombarding particle which is usually a gaseous ion, accelerated from the plasma. Incidence of these ions with sufficient energy on the target leads to an atomic collision cascade within the target material. When these cascades recoil and reach the target surface with energy above the surface binding energy of target atoms, an atom can be ejected.

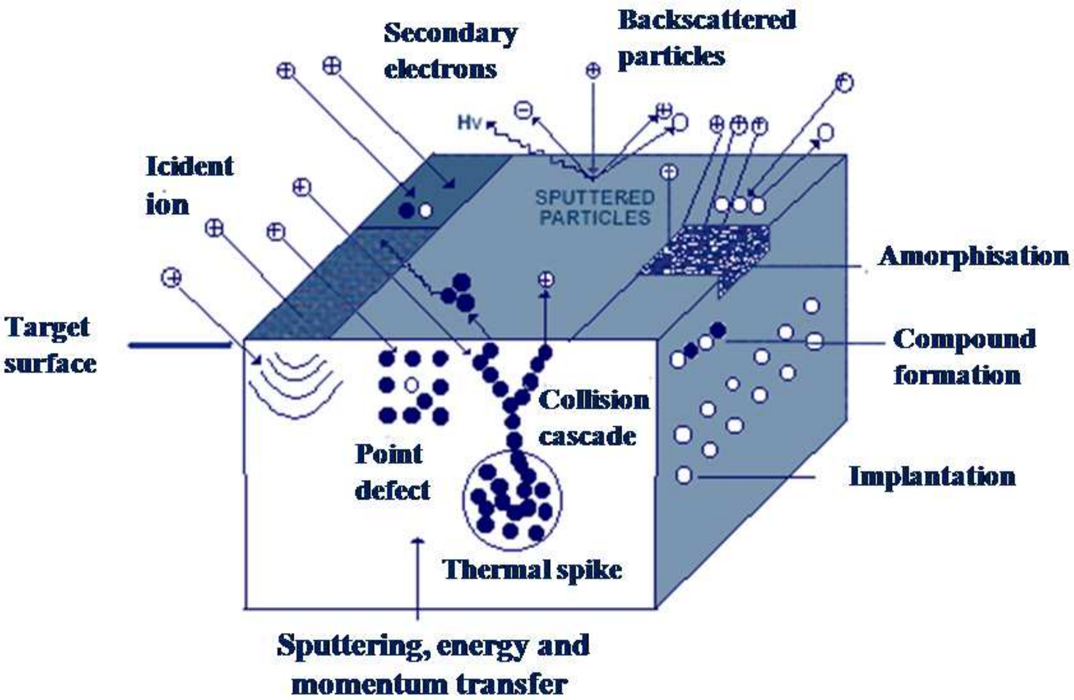

**Figure 3.1:** Depiction of processes generated on the surface being bombarded by energetic particles [60].

The sputtering yield (Y) is the most important parameter that characterizes the sputtering process. The sputtering yield can be defined as the average number of atoms ejected from the target per incident ion and is a measure of the efficiency of sputtering.

$$Y = N_{\text{ejected particles}} / N_{\text{incident particles}}$$

The sputtering yield depends on many parameters such as the mass of the bombarding particle as well as its energy, the mass of the target atoms, the surface binding energy of target atoms and the energetic distribution of the incident particles. It is also sensitive to the angle of incidence of the bombarding particle. In the case of very high energies, the sputtering yield decreases since the ions loose much of their energies below the surface and re-sputtering of the deposition material.

A theoretical description for the sputter yield has been given by Sigmund [61]; the sputter yield is expressed as a function of energy of the impinging ions on a planar surface. For low energy particles (E< 1 keV), the sputtering yield is defined as:

$$Y = \frac{3\alpha}{4\pi^2}\frac{4m_i m_t}{(m_i + m_t)^2}\frac{E}{U_o} \qquad 2.1$$

Where $m_i$ and $m_t$ are the mass of target atom and impinging ion, respectively. $E$ is the energy of the incident ion and $U_o$ is the surface binding energy of the target material. The parameter $\alpha$ is a measure of the efficiency of the momentum transfer in the collision and is a monotonically increasing function with value ranging from 0.17 to 1.4 as $m_t / m_i$ ranges from 0.1 to 10. Another formula has been derived to predict the sputtering yield in the case of high energy particles (E> 1 keV):

$$Y = \frac{0.042 \cdot \alpha \cdot S_n(E)}{U_o} \tag{2.2}$$

Where $S_n(E)$ is the energy loss per unit distance by incident ion.

By knowing the sputtering yield, the sputtering rate which is the velocity of ablation of the target can be determined. Theoretically, the sputtering rate $S_r$ (nm/min) is the summation of the sputtering rate due to ion $S_{ions}$ and neutral $S_{neutrals}$ bombardment. $S_{ions}$ can be determined from [62]:

$$S_{ions} = \frac{6.23 \cdot J \cdot W \cdot (Y)}{\rho} \tag{2.3}$$

Where $W$ and $\rho$ are the atomic weight (g/mol) and density (g/cm$^3$) of the sputtered material, $J$ is the current density at the cathode (mA/cm$^2$) and *(Y)* is the mean sputter yield. The energy distribution of the neutrals should be known for the determination of $S_{neutrals}$. It is reported [63-64] that the neutral bombardment contributes about 30% to 50% of the total sputtering rate in a glow discharge plasma. Hence with the calculation of $S_{ions}$, $S_r$ can be evaluated.

### 3.1.2 Principle of glow discharge for sputtering

The glow discharge can be approximately described as a plasma which is a partially ionized gas composed of ions, electrons and neutral species exhibiting a collective behaviour [65]. The density of charged particles must be large enough compared with the dimension of the plasma so that significant Coulombic interaction occurs. This interaction enables the charged species to behave in a fluid like fashion and determines the plasma properties.

A dc glow discharge is formed by applying of a potential between two electrodes. In the sputtering technique, the material to be sputtered (target) is operated as the cathode because it is connected to the negative terminal of the power supply. The substrate which faces the target plays the role of the anode and both are installed in an evacuated chamber. The glow discharge process is created by introducing the sputtering gas which is typically an inert gas (Argon) with a pressure ranging from a few to 100 m Torr into the chamber. Then an electric voltage in the kV range is applied to the target. This results in ionization of the sputtering gas when the existing native electrons in the chamber are energetic enough. The resulting $Ar^+$ ions are accelerated towards the cathode and lead to one or several of the physical processes which are described in section 3.1.1, in addition to generation of secondary electrons. These electrons cause the generation of new ions, which in turn result in emission of new secondary electrons. This ionization-emission cascade leads to the ignition of a self-sustained glow discharge between the cathode and the anode. This discharge is accompanied by a sharp rise in the current and drop in the voltage and this deposition technique is known as direct current (dc) diode sputtering.

The minimum potential difference $V_b$ (often referred as the breakdown voltage) between the cathode and the anode for the generation of a self- sustaining glow discharge depends on the pressure p of the gas and the anode to cathode distance d and can be defined as:

$$V_b = A\frac{pd}{\ln(pd)} + B \qquad 2.4$$

The constants A and B are parameters which describe the gas properties [66].

The area between the cathode and the anode has the most positive potential (the plasma potential). In the vicinity of the two electrodes sheaths develop with a net positive space charge, so that the electric field is restricted to these areas. The corresponding zones in the sputtering chamber are referred as the cathode sheath and anode sheath. The voltage distribution in a dc glow discharge is schematically shown in figure 3.2.

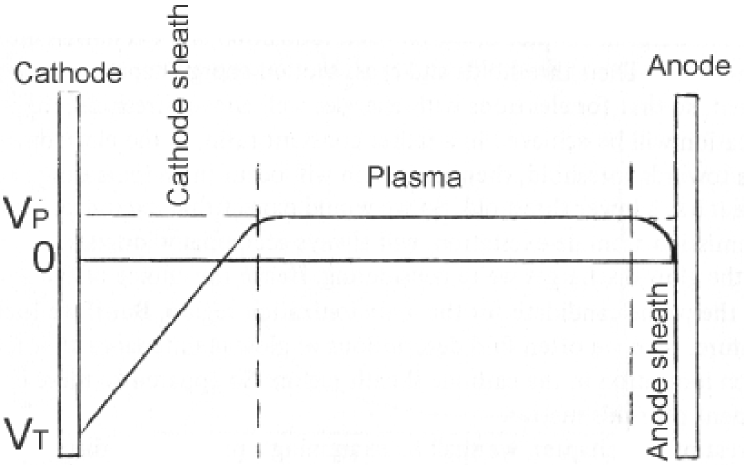

**Figure 3.2:** Voltage distribution in a dc glow discharge [67].

Generally in a dc glow discharge, there is a loss of energy due to the impingement of the energetic plasma on the electrodes and the walls of the chamber. This loss is compensated by the applied electric filed. Additionally, there is a loss of electrons due to recombination with the ions at the walls and into the external circuit at the anode. This loss of electrons is compensated by the emission of secondary electrons by bombardment of the cathode by positive plasma ions.

### 3.1.3 Magnetron Sputtering

Dc diode sputtering has the disadvantages of low deposition rates and low ionization efficiencies of the plasma due to the high working pressure. Additionally, as a consequence of the high target voltage, the growing films are heated by fast electrons which are repelled from the cathode. This in turn can affect the obtained film properties. Therefore it is desired to increase the plasma density in front of the sputtering target to maintain the glow discharge at low pressures and voltage and overcome these obstacles. This can be achieved by combining the existing electric filed with a magnetic field through attachment of a ring magnet below the target. The magnet is placed in such a way that one pole is positioned at the central axis of the target, and the second pole is placed in a ring around the outer edge of the target. In this case the moving electrons experience the well-known Lorentz force:

$$\vec{F} = \frac{mdv}{dt} = -q(\vec{E} + \vec{v} \times \vec{B}) \qquad 2.5$$

Where q, m and $\vec{v}$ are the electron charge, mass and velocity respectively while $\vec{E}$ and $\vec{B}$ are the electric and magnetic field vectors.

In the case when the electric field lies perpendicular to the magnetic field, the electron repelled by the negative cathode potential are trapped near the target and move in cycloidal curves over the target surface, as shown in figure 3.3. The electrons are confined in the vicinity of the target resulting in an increased ionization and this is the principle of the magnetron operation. As a consequence, the plasma density increases and thereby the sputtering rate. Also, the sputtering gas pressure can be reduced resulting in an increase of the incident particles energy and the possible momentum transfer. This is an advantage since less material is lost to the chamber wall and back to the target through scattering in the discharge gas.

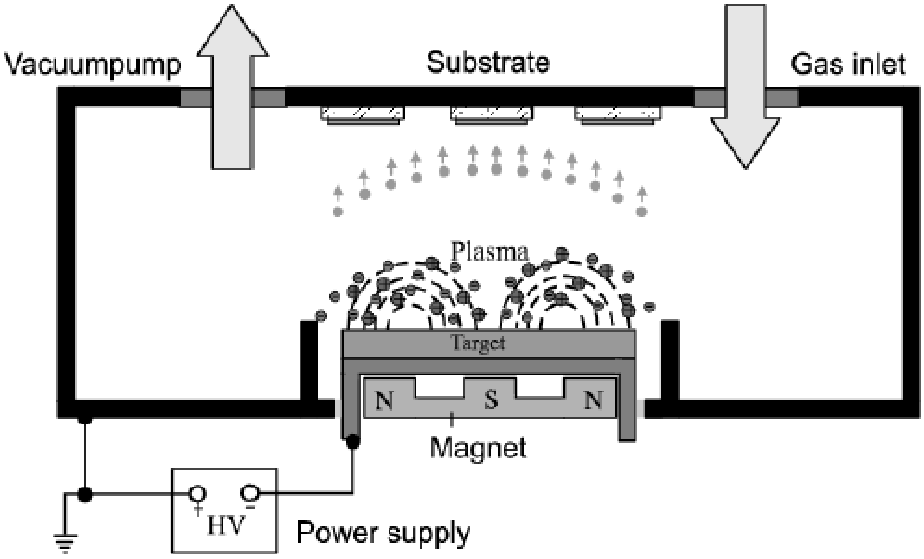

**Figure 3.3:** Basic principle of sputter deposition, ions generated in the plasma and accelerated towards a target of sputter material.

Due to the confinement of the electrons, the shape of the magnetic field efficiently erodes the target where the magnetic field lines are parallel to the target surface; a so-called race-track is created. An example of a sputtered circular target is shown in figure 3.4.

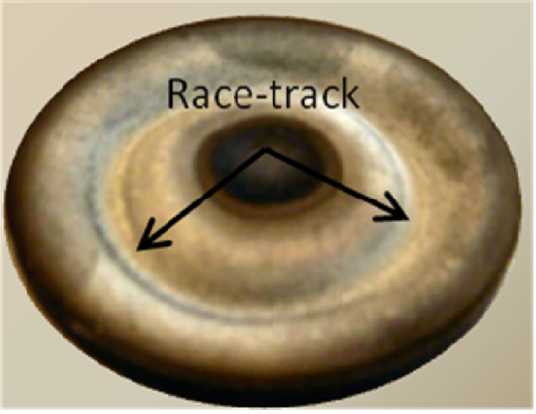

**Figure 3.4:** A typical circular sputter target. The race-track is created due to the erosion of the target attached to a magnetron.

### 3.1.4 Reactive magnetron sputtering

The sputter deposition can be used to deposit films of compound materials by sputtering either from a compound target or from an elemental target in the presence of a reactive gas “reactive sputter deposition”. The disadvantage of sputter deposition from a compound target is the confinement of the films stoichiometry to values similar to the target composition. In the case of a pure metal target used in combination with a reactive gas, the reaction between the sputtered material and the reactive gas can take place at the film surface and a compound film can be grown. This is the principle of reactive magnetron sputtering. The change of the sputtering gas composition affects the target stoichiometry (target coverage), since a part of the target's surface is covered by the same compound. The coverage of the target with compound molecules is referred as 'target poisoning'.

When a single reactive gas is supplied to the processing chamber, it reacts with the target and the collecting area of the chamber. The relationship between the film composition and the supply of reactive gas is non-linear and this process may exhibit hysteresis behavior. Figure 3.5 shows an example of the hysteresis phenomenon which is observed during reactive dc sputtering of zirconium oxide ($ZrO_x$) from a metallic target [68]. The variation of the oxygen partial pressure, target voltage and the mass deposition rate have been investigated at constant target current and constant working pressure with a variation of the oxygen flow from 0 to 4 sccm.

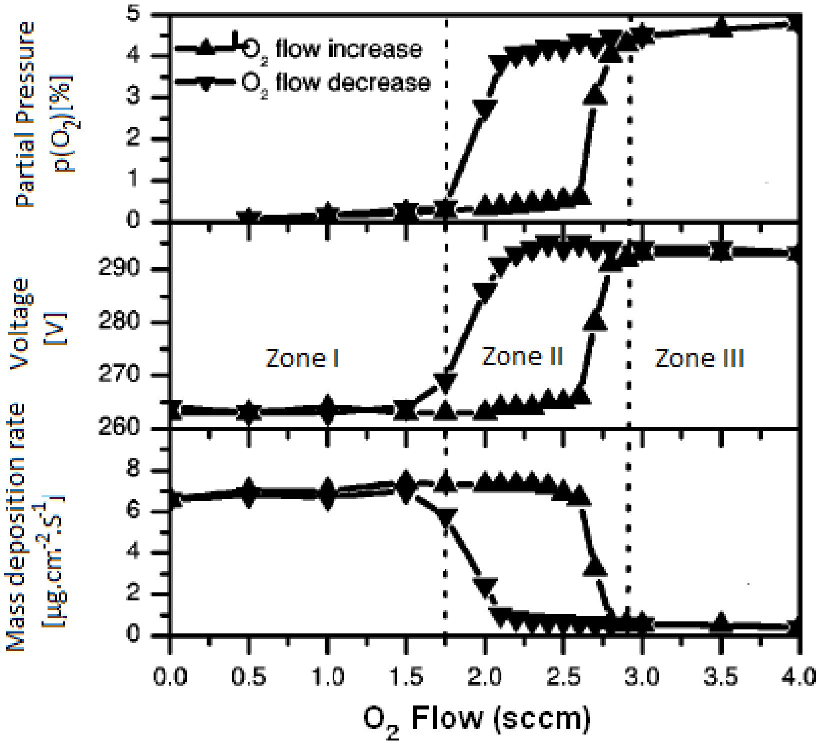

**Figure 3.5:** Influence of oxygen flow on: the oxygen partial pressure, target voltage and the mass deposition rate of reactively sputtered $ZrO_2$ films. The variation with increasing and decreasing oxygen flow shows a pronounced hysteresis effect [68].

Depending on the oxygen flow range three different regions can be distinguished. All properties remain constant in the regions I and III and these regions are separated by a hysteresis zone (II).

1. At low oxygen flow rate, no significant partial pressure of oxygen is formed since the molecules of the reactive gas are gettered by the sputtered atoms [69]. This sputtering regime is known as the metallic mode (Zone I) and is characterized by a high deposition rate and a low target coverage.
2. When the oxygen flow rate exceeds the gettering rate of the reactive gas molecules, more oxygen molecules become available for chemical reaction at the target surface. This leads to an increase of the oxygen partial pressure (Zone II). This regime is known as the transition mode which is characterized by a drop in deposition rate because of the increase of the target coverage which leads to a growth of a stoichiometric oxide films. This can be explained by the lower sputtering yield of the compounds than the corresponding metals due to the high strength of the covalent/ionic bonds present at the poisoned target surface [70]. The transition from metallic (region I) to compound mode (region II) is accompanied by a pronounced hysteresis effect. This transition is also found for the target voltage. An increase of the target voltage in the transition regime is attributed to an increase of the plasma impedance. This is explained by the effect of lower secondary electron emission yield of the oxide in comparison to the corresponding metal [71].
3. For higher oxygen flows, no pronounced change is observed for the target voltage and the mass deposition rate due to the stability of the target’s chemical condition (full poisoning), while the partial pressure increase linearly with the oxygen flow. This zone (Zone III) is referred as the oxidic mode.

In the reverse direction with decreasing of oxygen flow rate, the getter effect is not effective in this stage since the chamber walls are covered by the compound material. In addition, the sputtering rate of the material has to be higher than the oxidation rate at the given oxygen flow rate to get back to the metallic mode. As a consequence, a hysteresis loop occurs. This hysteresis effect is material dependent since it does not occur for all materials. In the transition regime, the process is unstable due to the hysteresis effect. However, the sputter deposition is possible in this regime but requires active process control.

### 3.1.5 Berg's model (Theoretical modeling of reactive sputtering)

A theoretical model for the reactive sputtering process (DC or RF) from an elemental target using one reactive gas has been developed by Berg et al. [70, 72]. This model is referred as "Berg's model" and describes the relationship between most parameters in the sputtering process. It also helps to understand the influence of the processing parameters on the overall behaviour of the sputtering process. A schematic description for Berg's model is presented in figure 3.6.

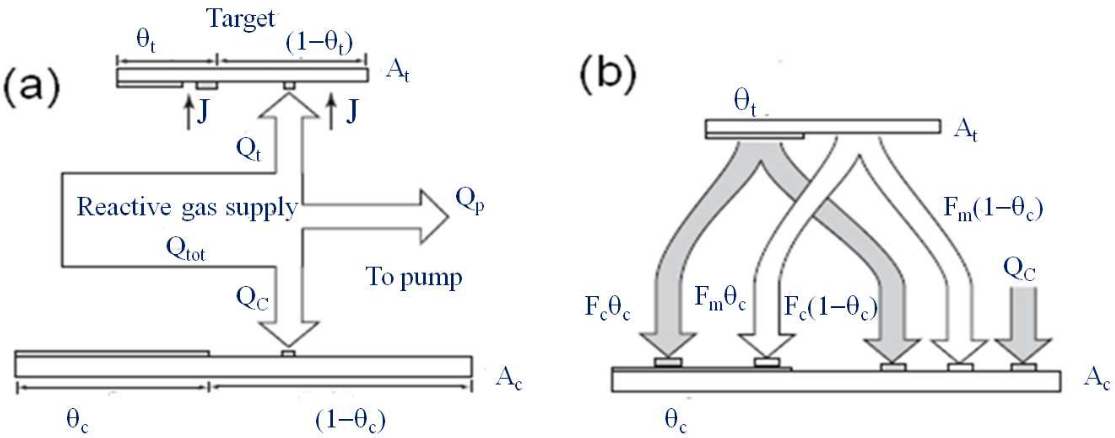

**Figure 3.6:** Theoretical model for a reactive sputtering process as explained by Berg. (a) Collecting area $A_c$ including substrate. (b) Abstract model for the flux of the sputtered material to the collecting area. $A_t$: target area. $Q_{tot} = Q_t + Q_c + Q_p$ is the sum of the respective reactive gas flows to the target, the substrate, and the pump. $\theta_c$, $\theta_t$ are the fraction of the substrate area and the target respectively, which is covered by compound molecules. $F_m$, $F_c$: total number of the sputtered elemental and compound particles respectively per unit time. J is the ion current density [70].

As assumed by the model, the whole sputtering system is divided into the target area ($A_t$) placed in front of a collecting area ($A_c$) in the vacuum chamber which is consisting of the substrate and the chamber walls. Both areas are assumed to be either free or covered by a monolayer of compound molecules. A reactive gas supply is connected to the chamber. Based on these simplifications, a broad range of process parameters is predictable.

- As there is a reactive gas, the reactions between elemental target atoms and the reactive gas will cause a fraction of the target to consist of compound molecules $\theta_t$. This compound formation is uniformly distributed over the whole target surface. This fraction of the target $\theta_t$ has a different composition than the remaining fraction (1-$\theta_t$). The fraction of the target surface (1-$\theta_t$) consists of elemental non-reacted atoms.

- The same situation exists at the receiving area $A_c$, where all sputtered material is assumed to be uniformly collected. The compound fraction at this surface area (deposited film) is denoted $\theta_c$.
- On the target surface, it is assumed that no reaction between elemental target atoms and the reactive gas can take place on the compound fraction of the target area $A_t$. On the other hand, it is assumed that at steady state on the substrate area, the composition of the added film material must be identical to the existing film composition.
- The total sputter erosion rate R, the deposition rate D, $\theta_t$ and $\theta_c$ can be calculated as a function of the partial pressure as shown in figure (3.7 (a, b)). The deposition rate curve may have a maximum value before reaching complete target poisoning. The curves of the compound fractions of the target $\theta_t$ and of the collecting surface $\theta_c$ show that fully stochiometric films can be obtained when the target compound fraction is only $\theta_t \sim 0.8$. This effect is possible because a number of already sputtered and deposited target atoms can react with reactive gas atoms on the substrate surface. The difference between the compound fractions of the target $\theta_t$ and the collecting area $\theta_c$ is thus strongly dependent on the ratio of the respective total surfaces $A_t / A_c$.
- It has been pointed out that the characteristic "S-shape" of the curves in the transition regime corresponds to the hysteresis width, figure (3.7 c).
- A mathematical expression has been derived to illustrate the origin of the hysteresis. Also the presence or absence of a hysteresis can be predicted from the derivation $dQ_{tot}/dP$. If in some region $dQ_{tot}/dP < 0$, this means that the process will exhibit a hysteresis. If $dQ_{tot}/dP > 0$ over the whole region, then the hysteresis will not exist in this process. It can be determined using the relation:

$$\frac{dQ_{tot}}{dP} = \frac{dQ_t}{dP} + \frac{dQ_c}{dP} + \frac{dQ_p}{dP} \qquad 2.6$$

- The hysteresis cannot be eliminated by applying a high power to the target which leads to reducing the target poisoning effect by a high sputter erosion rate. Increasing the argon ion current causes a magnification of the curves as shown in figure (3.7 d).

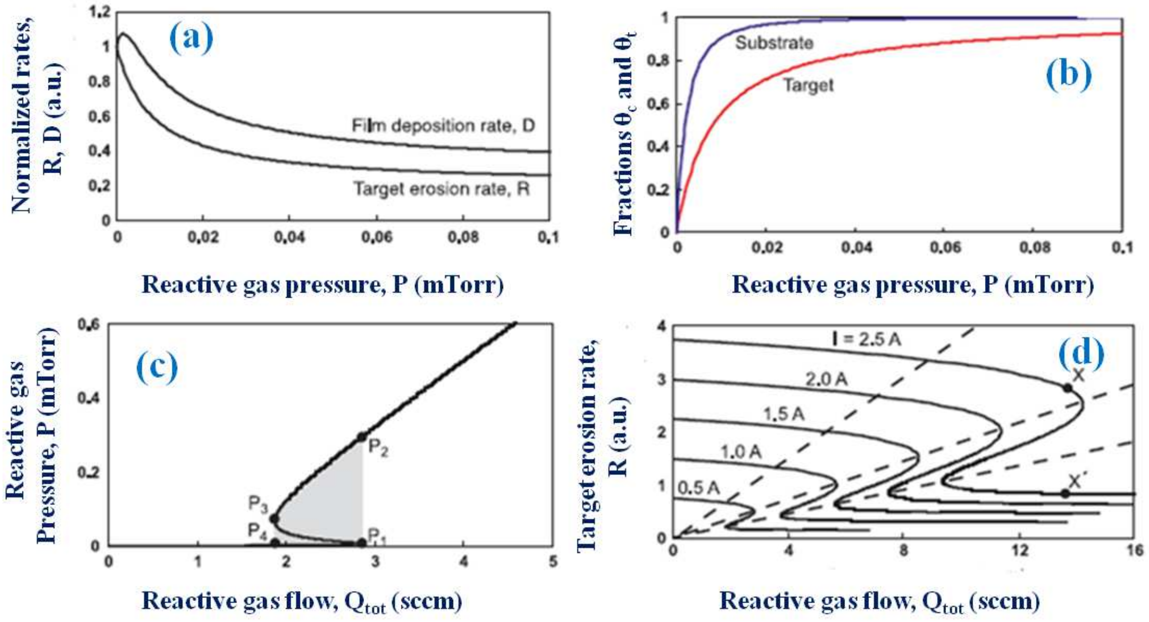

**Figure 3.7:** Behaviour of various process parameters during reactive sputtering as simulated by Berg‘s model. (a, b) Calculated target erosion rate R, substrate deposition rate D and the compound fractions $\theta_c$, $\theta_t$ at the target and substrate as a function of the reactive gas partial pressure P. (c) Calculated partial pressure P, (d) argon ion current as a function of the reactive gas flow $Q_{tot}$.

Berg’s model is not a complete model to describe the reactive sputtering process. The simplifications made in the model restrict the validity of the calculated results. Berg’s model considers the getter effect to be the physical process which governs the target voltage. On the contrary, Depla et al [73] could experimentally detect that the discharge voltage behavior originates from the formation of an oxidized layer which is 1-2 nm thin on the target surface during the sputtering process. In addition, the influence of ion implantation on the process behavior has been considered [74].

### 3.1.6 High power Impulse magnetron sputtering

HiPIMS stands for High Power Impulse Magnetron Sputtering. This technique is based on increasing the plasma density in front of the sputtering source and thereby decreasing the mean ionization distance for the sputtered particles. Increasing the plasma density can be achieved by applying high power density to the target of several kW $cm^{-2}$ in short unipolar pulses of low duty cycle (on/off time ratio <10%) and pulse repetition frequency (<10 kHz), as schematically shown in figure 3.8. As a consequence of the generation of a high density plasma, the ion–to–neutral ratio increases by increasing the ionization probability of the sputtered material [75]. These features provide the possibility to tailor the film properties, depositing dense and smooth metallic [76] and compound films [77]. Also as a result of increasing the ion bombardment and implantation [78], the adhesion of the coatings will be enhanced.

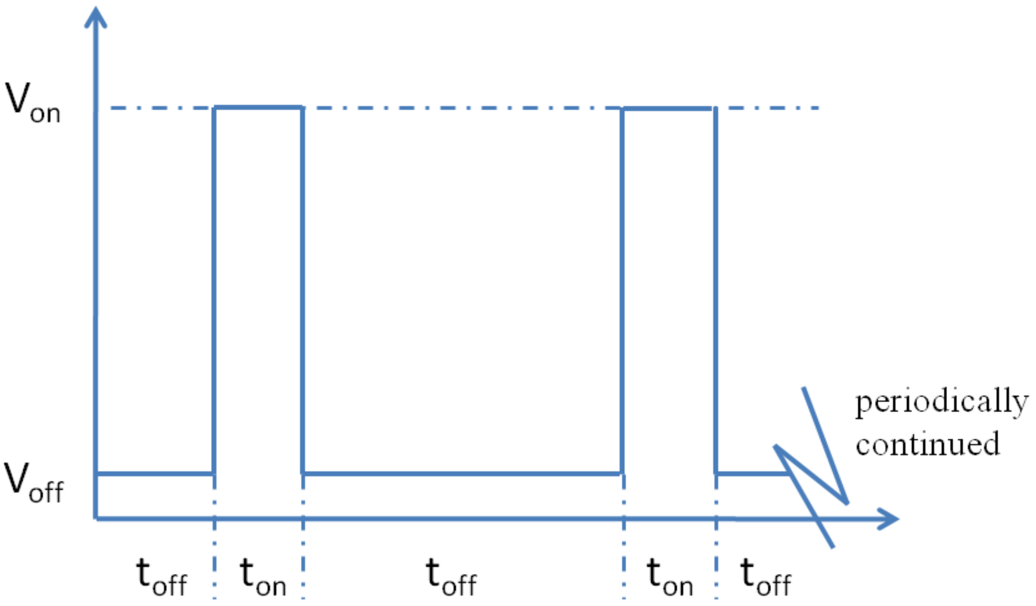

**Figure 3.8:** A schematic representation of the target voltage during HiPIMS, $t_{on}$ and $t_{off}$ are the pulse on- and off-time respectively.

The power density supplied to the target is limited by thermal load that the target can receive. Most of the energy of the positive ions accelerated to the target is transformed into heat. Therefore, the average target power density should be low (a few W $cm^{-2}$) to prevent the target from overheating and damage of the magnets and the target. A schematic of a HiPIMS power supply is shown in figure 3.9.The electrical pulses are generally generated by discharging a capacitor bank via a semiconductor-based switch. The capacitors are charged by a DC power supply which is connected to the magnetron. The capacitors are discharged in a repetitive manner. They release the stored energy in pulses of defined width and frequency using fast switches in the µs range, located between the capacitors and the cathode. The size of the capacitor bank is typically 1-50 µF, depending on the size of the target.

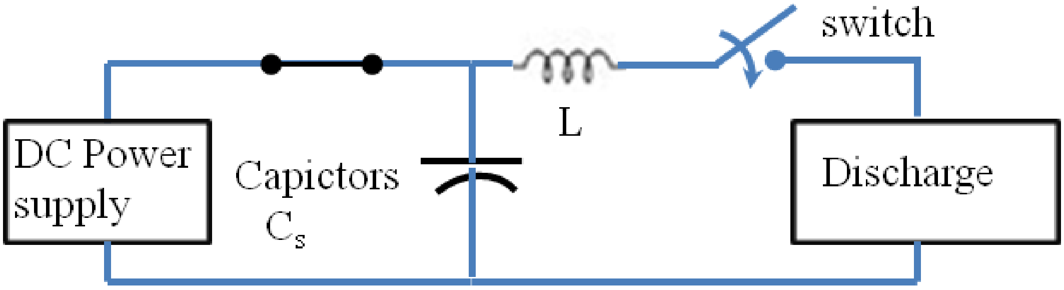

**Figure 3.9:** A schematic of HiPIMS processes.

One of the major drawbacks of this technique is the lower deposition rate in comparison to DC sputtering. This reduction is mainly due to the self-sputtering phenomena [79]. Some of the ionized material in the dense plasma is recaptured on the cathode surface by the high negative voltage. In the presence of a magnetic field, a fraction of the applied voltage will penetrate the bulk plasma and create a potential gradient. As a consequence, if the sputtered atoms cannot overcome this potential and reach the substrate surface, it is drawn back to the target and causes self-sputtering and the deposition rate drops. Another problem in the HiPIMS process is the occurrence of arcs on the cathode surface. This phenomenon occurs during deposition from conducting targets covered by insulating layers. It has been observed that dielectric particles on the target surface may be the source of arcing, since they can be charged up to a high voltage and then discharge. To avoid this problem, HiPIMS can be operated using short pulses in the range from 5 to 20 µs [80].

## 3.2. Mechanism of film growth

The fundamentals of the sputtering deposition process have been presented in the previous section. The growth process of thin layers on the substrate will be discussed in this section. The film growth as well as the nucleation process determines many film properties such as film density, surface area, surface morphology and grain size. As presented, the sputtering leads to formation of a thin film by deposition and condensation of atoms from the vapor phase on a substrate. This process can be described as a sequence: the initial stage (nucleation) at first; where single atoms or molecules are adsorbed on the substrate and then several atoms can combine to form clusters (nuclei). Then these nucleation centers converge together to form a fully covering film in the so-called (coalescence) stage. Finally in the advanced stage of film growth a closed (continuous) film can be formed. The growth mechanisms during these stages are presented in this section.

### 3.2.1. Nucleation

During the earliest stages of film formation a sufficient number of vapor atoms or molecules condensed. Condensation occurs when the impinging atoms transfer their kinetic energy ($E_{kin}$) to the substrate and dissipate it into lattice vibrations. To keep the atoms on the surface, their kinetic energy has to be lower than their adsorption energy ($E_{ad}$). The sticking coefficient is the probability that an impinging atom is incorporated into the substrate surface. It is measured by the ratio of the amount of condensed material on the surface to the total amount of material impinged. Once the atom has been adsorbed (called an "ad-atom") it migrates along the substrate's surface and jumps from one lattice site to another (diffusion) [81]. Diffusion is a thermally activated process; it provides the migration mechanism of the ad-atoms to find their required positions to reproduce the correct crystal structure. Finally, the formation of an atomic layer has to proceed through the aggregation of mobile ad-atoms into stable clusters (nucleation) which grow by accumulation. On the other hand, far from equilibrium growth, the ad-atoms aggregate together and form nuclei which either tends to grow in size or dissociate. When the critical nucleus size reaches atomic dimensions, the atomistic theory of nucleation has to be used.

Based on the thermodynamic consideration, Bauer [82] introduced a classification of epitaxial growth modes. The term epitaxy is used for the growth of a crystalline layer upon a crystalline substrate, where the crystalline orientation of the substrate imposes an order on the orientation of the deposited layer [83]. Three different growth modes are distinguished according to the balance between the surface free energy of the deposit $\gamma_D$, the surface free energy of the substrate $\gamma_S$ and the interface free energy $\gamma_{int}$. This is known as Bauer's criterion, which is shown in figure 3.10.

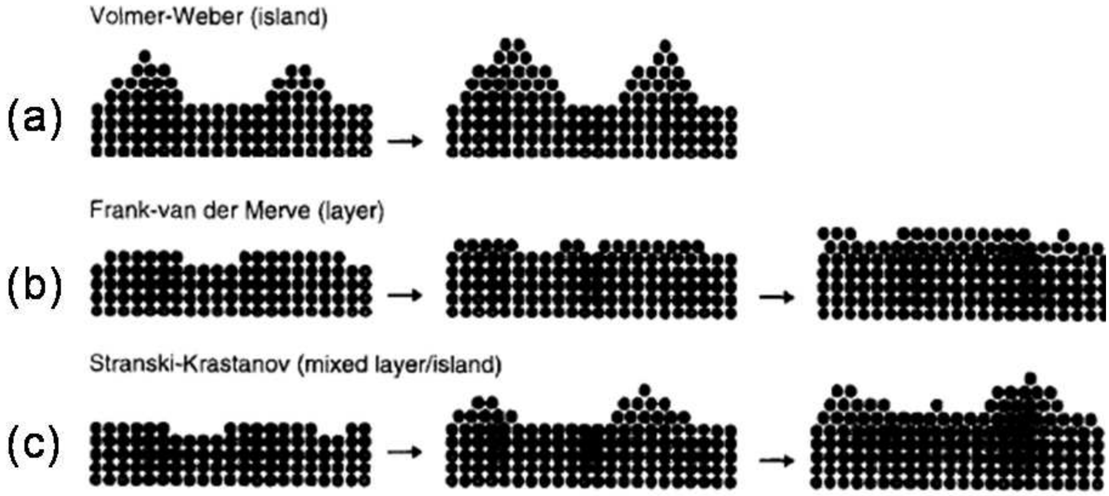

**Figure 3.10:** The three epitaxial growth mechanisms close to thermodynamic equilibrium: (a) Volmer-Weber mode, (b) Frank-Van-der-Merve mode and (c) Stranski-Krastanov growth mode [84].

- When $\gamma_S < \gamma_D + \gamma_{int}$, the energy balance requires to minimize the area covered by the deposited material and the deposit will grow in the form of three dimensional islands on the substrate. This mode is referred as *Volmer-Weber* growth, figure 3.10 a.
- In the case of the limiting condition, $\gamma_S = \gamma_D + \gamma_{int}$, this growth mode is referred as *Frank-Van-der-Merve*, figure 3.10 b. This is an ideal mode for homoepitaxial growth system (growth of crystalline layer on a chemically identical crystalline substrate).
- If $\gamma_S > \gamma_D + \gamma_{int}$, the area covered by the deposited material should be minimized and the deposit will grow smoothly forming one layer at a time. The growing layer will be strained. After deposition of a few layers, the influence of the substrate's free energy vanishes and the energy tends towards zero. This will break the condition for layer-by-layer growth and leads back to the island growth. This growth mode is known as *Stranski-Krastanov* growth mode, figure 3.10 c.

### 3.2.2. Coalescence

As a consequence of the progressive growth of the nuclei, coalescence of individual nuclei with each other proceeds until a closed film is formed. The coalescence phenomenon has a strong effect on the structure and the properties of the resulting film; since recrystallization, grain growth, and orientation changes occur as a consequence of coalescence [85].

The coalescence phenomenon has been discussed in terms of “sintering” of two particles in contact with each other. The coalescence occurs only when islands touch each other physically; this mechanism is similar to the sintering of two spheres. When two nuclei touch each other at a contact point, a thin neck forms first and then grows in width until both nuclei are fused completely with each other. The driving force for neck growth is simply the natural tendency to reduce the total surface energy of the system. Hence a flow of atoms moves toward the neck. The general behavior of the necks has been explained on the basis of mass transport resulting from the tendency to minimize the surface energy.

### 3.2.3. Advanced layer growth

The influence of deposition parameters on the film growth can be understood in terms of their effects on the sticking coefficient, the nucleation density, and the surface mobility of ad-atoms. Agglomeration of a film increases with increasing the surface mobility and decreasing the nucleation density. Also deposition of layers at different deposition parameters yields very different structural properties. This section deals with the origin of the structure of the growing layers. A model referred as the structure zone model (SZM) is constructed to describe the influence of the deposition parameters on the microstructure of the growing film [86]. This model predicts three structural zones as a function of the homologous temperature $T_h=T/T_m$, where T is the substrate temperature and $T_m$ is the coating- material melting point. From figure 3.11, the three zones are characterized as:

1. Zone I ($T/T_m < 0.3$): Columnar growth, the film is composed of fibers of small diameters. The crystalline fibers grow out of the primary nuclei and proceed to the top of the film. The crystal diameter increases with $T/T_m$, the crystal contains a high density of defects and the grain boundaries are porous.
2. Zone T ($0.3 < T/T_m < 0.5$): The film growth is controlled in this region by the ad-atom surface diffusion. The structure consists of columnar grains separated by distinct dense, intercrystalline boundaries. The grain sizes increase with $T/T_m$. The structure is fine crystalline at the substrate, composed of V-shaped grains while columnar grains can be grown in the upper part of thick films. The development of V-shaped crystals is a result of the competition taking place among the differently oriented neighboring crystals which concludes in a columnar morphology at higher thickness.
3. Zone II ($T/T_m > 0.5$): Textured growth, the bulk diffusion is significant. The structure consists of equiaxed grains with a bright surface. This structure is attributed to the high

substrate temperature range. The grain diameters increase with T/$T_m$. This strong restructuring is controlled by the minimization of the interface and the surface energy and leads to the growth of a film with pronounced texture.

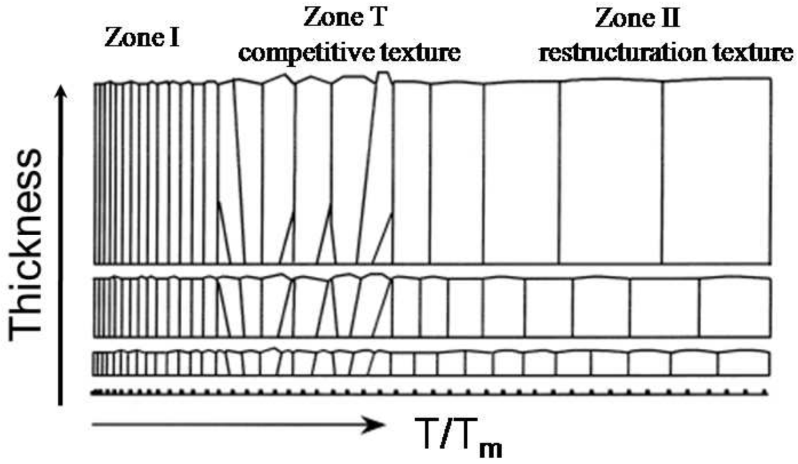

**Figure 3.11:** Basic structure zone models as a function of the homologous temperature T/$T_m$ and the film thickness [89].

Thornton [87, 88] has extended the structure zone model to magnetron sputtered films by adding an axis for the sputtering gas (Ar) as shown in figure 3.12. The pressure affects the direction and the energy delivered to the surface by sputtered species and energetic bombarding species. A high pressure means an increase in collisions of the sputtered particles and simultaneously a decrease in the average energy of the particles arriving at the substrate. This model predicts that a decrease of sputtering pressure will shift the transition from Zone T to Zone II to lower values of T/$T_m$, due to the increase of the energy transferred to the film by the energetic plasma species. Zone 1 is characterized by a high argon pressure, voided structure and the occurrence of tensile stress. Zone T (transition zone) consists of a dense array of poorly fibrous grains without voided boundaries. At high T/$T_m$, the film surface is smooth.

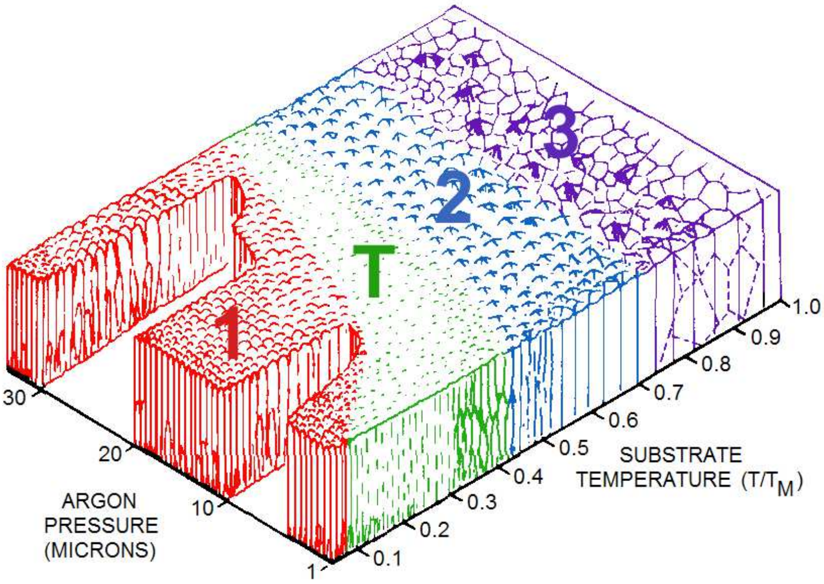

**Figure 3.12:** Structure Zone model by Thornton, schematic representation of the dependence of the coating structure on a substrate temperature and argon pressure. T is the absolute temperature and $T_m$ is the melting temperature of the coating material [90].

Gaseous impurities and atoms of the reactive gas could have drastic effects on the microstructure, so the concentration of these species should be considered. Thus active species such as oxygen have been found to reduce adatom mobility and therefore can promote Zone 1 structures. In addition, the intense energetic ion bombardment during deposition can suppress the development of the open zone 1 structures at low $T/T_m$. Since the energy flux carried to the substrate by the neutralized and reflected ions depends on the target mass relative to that of the working gas, and the working gas pressure. The atoms reach the substrate with a substantial fraction of their initial energy at low working pressures. The bombardment by energetic particles is an important parameter during film growth. The effect of these species will be discussed in the next section. Moreover, bombardment by such energetic particles can lead to stress development. A study of stress development during film growth can provide evidence of the presence, energy and nature of bombarding particles. The residual film stress in sputtered films will be presented in section 3.4.

Thornton [91] has also observed that Zone T emerged upon decreasing the sputtering gas pressure. It is considered to be the internal structure of Zone 1. Also Zone 1 and the T boundary is non-linear and varies in a fashion similar to the film bias potential as a function of gas pressure. Therefore, Messier et al. [92] has modified Thornton's model by replacing the gas pressure with $V_s$. This $V_s$ induced mobility seems to be the more fundamental process which affects the physical structure rather than pressure.

## 3.3. Influence of energetic particles on the film growth during sputtering

Bombardment of the growing film during the sputtering process by energetic species is one of the most important parameters governing the phase formation. In addition, it exerts a strong influence on the microstructure of the film. The energetic particles transfer energy and momentum to atoms in the film as they slow down. The effect of such particles on the growing film depends on its energy and its flux. In particular, the interaction of the energetic species with the atoms of the target material depends on the ion energy [84].

Films grown at low energetic bombardment exhibits a columnar structure with closed grains. An increase of the bombarding energy leads to re-nucleation with interruption of columnar growth. In addition, the high energies of the bombarding particles damage a surface by creating near-surface defects due to the implantation of the energetic species in the growing film and partially destroy the growing film. This phenomenon leads to the generation of residual compressive stress in the thin film. Compressive stresses can also be generated by incorporation of rare gas. Other effects can appear due to implantation of energetic particles in the growing film such as resputtering and channelling mechanism (penetration of highly charged species deeply in the growing film). Not all the energetic particles that strike a substrate are implanted in the film. Some of them are backscattered.

In the case of reactive sputtering of metal oxides from metallic targets, high energy $O^-$ ions are generated at the target surface and bombard the growing film. These ions have implications on the film growth. The existence of $O^-$ ions has been verified by employing the time-of-flight method during sputtering from ceramic ZnO and $BaTiO_3$ targets [93]. They have proven that the oxygen ions with energies equivalent to approximately the full cathode potential strongly influence the structure formation [94]. These ions are created at the target surface from collisions with the sputtering species. Also Mráz et al. [48] has explained the relationship between the target voltage and the energy distributions of $O^-$ ions of transition metal oxides. Three ion populations were detected in the plasma. The low energy ions may be formed in the cathode sheath. The medium and high energy ions with energies corresponding to half and full of the target potential may be sputtered from the target as $O_2^-$ and $O^-$ and are accelerated over the cathode sheath. In addition, Ngaruiya et al. [49] have deduced that large fluxes of medium and high energy $O^-$ ions comparable to the fluxes of low energy $O^-$ ions enable formation of crystalline transition metal oxide thin films at low temperature. They have also concluded that at low flux of high energetic ions which is typical for groups V and VI leads to amorphous films. The ion energies in this case are sufficient to produce thermal spikes to release stress and also cause backsputtering at low total pressures. On the other hand, high fluxes at low energies for group IV lead to film crystallization and rearrangement of deposited atoms, thereby creating high compressive stresses.

These negatively charged ions are generated at the poisoned fraction of the target surface and are accelerated within the cathode dark space towards the growing film, where the electric potential gradient is almost perpendicular to the target surface even at the racetrack. In this very narrow area the entire target voltage drops. The trajectories of these ions are strongly governed by the geometry of the racetrack and therefore the age of the target [50]. As sketched in figure 3.13, in the case of a new target without any pronounced erosion trace; the ions are mostly accelerated directly towards the edge of the substrate. In the case of an old target the opposite behavior is observed. The centre of the substrate is bombarded by a large flux of highly energetic oxygen ions.

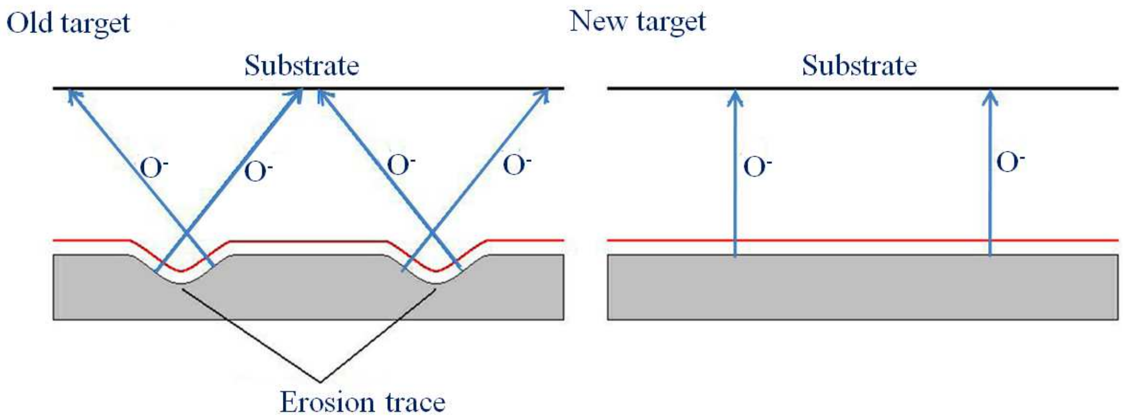

**Figure 3.13:** Trajectories of $O^-$ ions for an old target with a strong erosion trace and a new target with planar surfaces. For new targets, the ions are accelerated towards substrate positions directly opposite the erosion trace. For aged targets, the distribution of ion trajectories strongly depends on the shape of the erosion trace, which typically results in bombardment predominantly of the sample centre [90].

## 3.4. Generation of stresses in thin films

Intrinsic stresses are the cumulative result of chemical and microstructural defects incorporated during the film condensation process. As discussed in the preceding section, the growing films experience an intense energetic bombardment. This leads to the formation of films with high defect density and residual stresses. The intrinsic stresses in the deposited thin films can lead to severe problems including adhesion failures, defects in the substrate, fracture and undesirable formation of holes. Additionally, film stresses influence the electronic properties and lead e.g. to semiconductor bandgap shifts. In general, the intrinsic stresses can be tensile or compressive. The tensile stresses are considered to be positive while the compressive stresses are considered to be negative. A model for the generation of internal stress (a) tensile and (b) compressive in thin film/substrate during the deposition of a film is illustrated in figure 3.14. As shown in the case of tensile stress (a) due to surface tension forces, the growing film shrinks relative to the substrate. To achieve equilibrium in the bending moments, the substrate is bent concavely upward. In similar fashion, compressive stress bends the substrate convex outward.

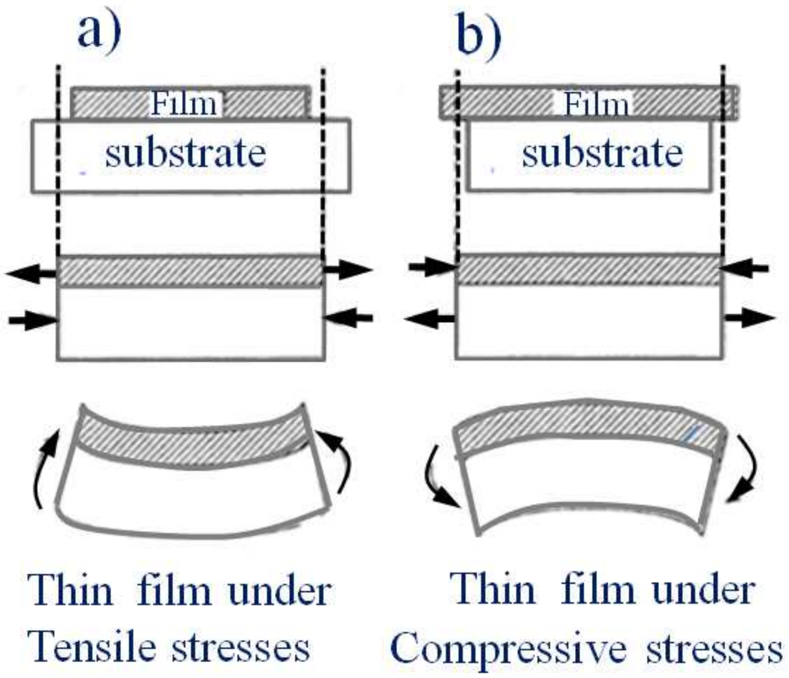

**Figure 3.14:** Sequence of events leading to (a) residual tensile stress; (b) residual compressive stress in a film [67].

The nature and magnitude of stress depends on the energy of the deposition process (the particle flux and energy striking the condensed film) which is linked with the film microstructure. The intrinsic stresses in sputtered films are related to the structure zones. Tensile stress is observed in zone 1- type, porous films, with a void rich microstructure and is explained in terms of the grain boundary relaxation model [95]. Compressive stress is observed in zone T-type, dense films and is interpreted in terms of the atomic peening mechanism [96, 97]. In the magnetron sputtering process, the presence of highly energetic particles leads to the formation of compressive stresses in the film. The different models which explain the origin of this phenomenon will be discussed in this section.

### 3.4.1 Atomic peening model

D' Heurle [97] suggested that the compressive stress observed in sputtered films is caused by bombardment of the film surface by energetic particles species in a process similar to "shot peening". During sputtering, when the impinging ions have energies of tens to hundreds of eV, their collision with the growing film will result in a displacement of atoms into the film, i.e. into spaces smaller than the normal volume per atom. This leads to an expansion of the film outward from the substrate. Since the film is not free to expand, the entrapped atoms cause macroscopic compressive stress.

This model [98] assumes that (i) atoms are displaced from their equilibrium positions by a series of collisions which produce a distortion in the volume; (ii) at low deposition temperature ($T/T_m$ <0.25), the mass transport and the defect mobility are low to freeze the volumetric distortion in place; and (iii) the relative volumetric distortion (strain) is proportional to the fractional number of atoms n/N displaced from equilibrium sites. The compressive stress can be expressed by:

$$\sigma = k\phi\sqrt{E_p Q},$$

$$Q = \frac{EM}{(1-v)D} \qquad 2.7$$

Where $\Phi$ is the ion flux, $k$ is a factor that contains Avogadro's number and other numerical constants. $E_p$ is the particle energy. $Q$, M/D is the elastic energy per mole and the target material's atomic volume respectively. $E$, $v$ is Young's modulus and Poisson's ratio respectively. This expression shows that:

- The compressive stress depends on the molar volume. This indicates that the strain produced due to the interaction between the particles and the film target is related to the atomic arrangement.
- In addition, the stress is dependent on the physical properties of the target, the energy, flux and angle at which particles bombard the film.
- The forward sputtering linear cascade theory suggests that the stress should be scaled with the momentum rather than energy due to the dependence of the compressive stress on the particle energy.

Müller [99] has shown that ion incorporation and recoil implantation of surface atoms led to film densification caused by a momentum transfer process i.e. the structure modification is affected by the particle energy. The microstructure evolution for Ni as a function of particle energy is illustrated in figure 3.15. At low adatom kinetic energy, the structure is rich in defects- large micropores, open voids and microcolumns are noticeable with correspondingly low tensile stress, figure 3.15 (a). As the energy increases, the pores become smaller and the atomic network is more interconnected, the tensile stress increases and reaches a maximum value (b). At lager incident energies, the defects gradually disappear and a well-layered crystal structures evolves. This is accompanied by tensile stress reduction as pores collapse (c).

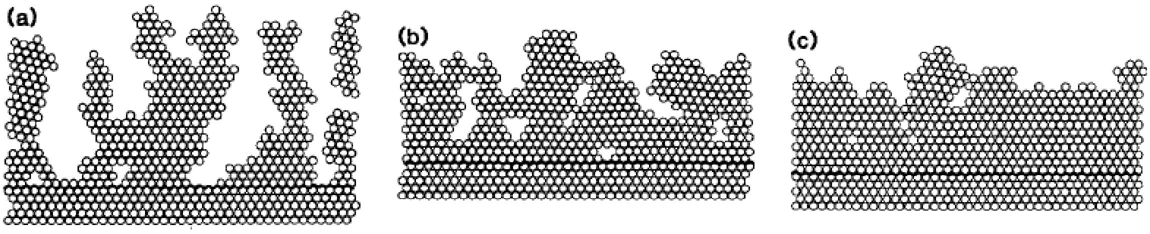

**Figure 3.15:** Typical microstructure evolution as a function of incident energy, a) low particle energy, b) intermediate energies, and c) higher energies [99].

## 3.4.2 Momentum transfer model

As discussed in the preceding section, the stress is momentum dependent. The bombarding ions can transfer momentum to the colliding atoms. Therefore, the momentum transferred into the film by bombarding ions per depositing atom is given by [96]:

$$P_n^* = \phi\sqrt{2ME} \tag{2.8}$$

Where $\phi$ is the bombarding ion flux, M is the ion mass and E is its energy. The variation of the intrinsic stress with the normalized momentum $P_n^*$ for any sputtering or ion-assisted evaporation process is shown in figure 3.16. The stress profile consists of three regimes:

1. At low $P_n^*$: films are characterized by Zone 1 microstructure which is unable to support high tensile stress. This low momentum might exist at high pressure sputtering, or using a light mass target with a heavy mass inert gas, or oblique deposition.
2. Increasing the momentum $P_n^*$: the atomic- peening mechanism becomes operative which leads to porosity annihilation by recoil implantation and knock-on processes. This results in densification of the microstructure, transition from zone 1 to zone T. Consequently, the tensile stress decreases as it is compensated by compressive stress. In this region, the atomic peening mechanism is predominant and the forward sputtering model predicts a linear dependence on particle momentum.
3. At high $P_n^*$: the compressive stress reaches maximum as the yield strength of the material is attained. A Further increase in the momentum leads to plastic flow.

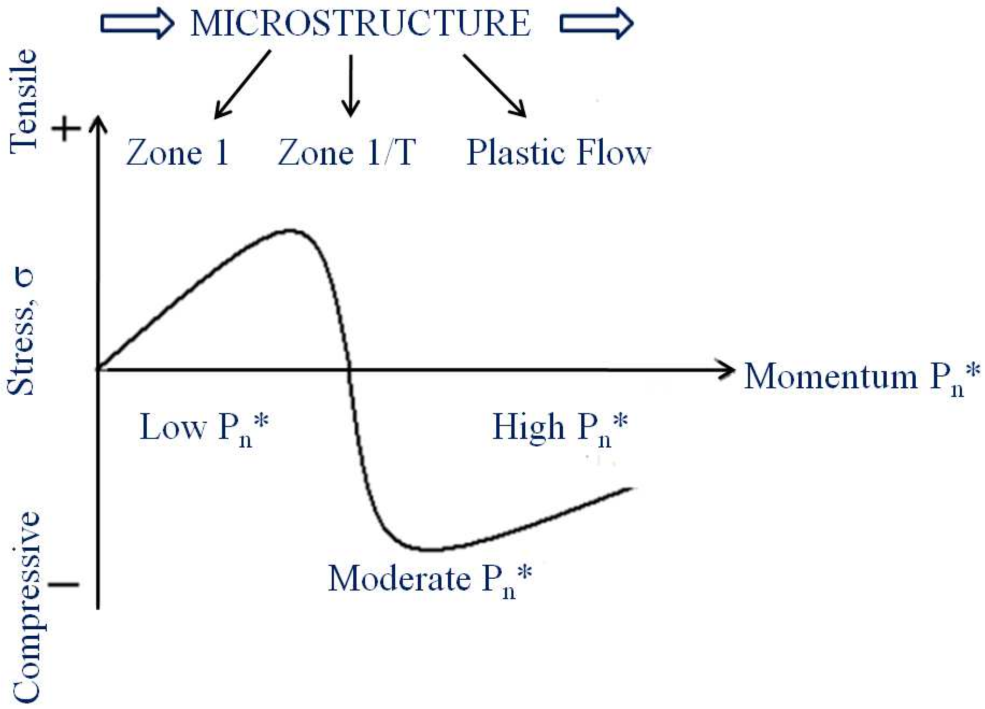

**Figure 3.16:** Idealized intrinsic stress vs. Normalized momentum $P_n^*$. The corresponding microstructure with increasing momentum is also shown [98].

### 3.4.3 Knock-on implantation and thermal spike (Davis model)

A successful description of the origin of compressive mechanical stress in sputtered film has been put forward by Davis [100]. This model explains that the net compressive stress results from a balance between the stress induced by “knock-on implantation” of the film atoms and stress relaxation by “thermal spike migration”. Knock-on implantation occurs when an energetic ion with energy above a certain threshold $E_{crit}$ transfers sufficient energy to the film atoms to implant them below the surface of the film. As the volume occupied by the displaced atoms is smaller than the normal atomic volume, the film is placed in a strained state by the knock-on implantation. Formation of a compressive stress is associated with this strain. A reduction in the stress by movement of the implanted atoms to the film surface is energetically favoured. To do so, an implanted atom must acquire a certain threshold energy $E_0$ to overcome the energy from the surrounding atoms and escape from its metastable position to the surface of the film. The required energy can be received from the bombarding energetic particles. When these hit the surface of the film, their energy is transferred to the surrounding atoms. This produces a local heating which is referred as “a thermal spike”.

Based on the assumption of this model that there is a balance between implantation and relaxation, so that the density of implanted atom is constant with time and the magnitude of the compressive stress σ is proportional to:

$$\sigma(E) \propto \frac{Y}{1-v}\frac{E^{1/2}}{R/j+kE^{5/3}}, \qquad k=0.016\rho E_0^{-5/3} \tag{2.9}$$

Where E is the ion energy, R the net depositing flux, j is the bombarding flux and k is a material dependent parameter. Y is the Young’s modulus of the film material and *v* is the Poisson ratio. The variation of compressive stress as a function of the kinetic energy of the incident particles for different values of R/j can be predicted as shown in figure 3.17.

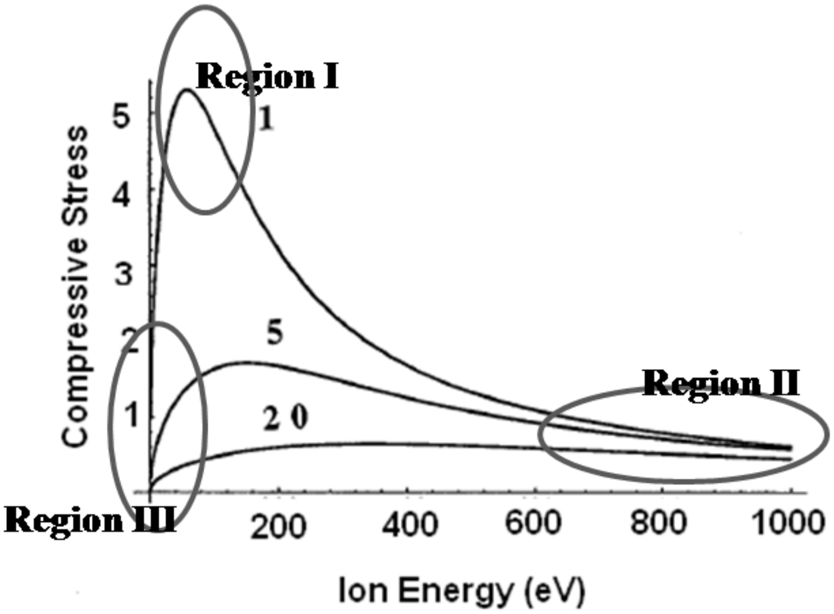

**Figure 3.17:** Variation of compressive stress as a function of the kinetic energy of the impinging particles at different values of R/j =1, 5 and 20 as predicted by Davis model [100].

In general, the compressive stress increases to a maximum with increasing ion energy and then decreases for all fluxes. For higher values of E, the compressive stress slowly decreases (Region II). Also the magnitude of the maximum compressive stress is highly dependent on R/j (Region I). The lower the values of R/j, the larger the compressive stress is observed. While the lower values of compressive stress are found at high values of R/j. Two cases for stress reduction can be identified from equation 2.9:

1) When the energetic flux is low, then R/J is large compared *to* $kE^{5/3}$. The compressive stress can be expressed as:

$$\sigma(E) \propto \frac{Y}{1-\nu}\frac{jE^{1/2}}{R} \qquad 2.10$$

2) When the energetic flux is large enough, so that R/j is small compared to $kE^{5/3}$, the compressive stress can be approximated by:

$$\sigma(E) \propto \frac{Y}{1-\nu}\frac{1}{kE^{7/6}} \qquad 2.11$$

From equations 2.10 and 2.11, the simple methods for reducing the compressive stress upon sputtering are:

- For low normalized fluxes: the stress is proportional to the square root of the ion energy and is determined by the magnitude of the kinetic energy of the incident particles as implied from equation 2.10. Low compressive stress is found for small ion energies E (Region III in figure 3.17).

- For large fluxes j: equation 2.11 shows that the mechanical stress can be reduced by increasing the ion energy (Region II in figure 3.17).

On the other hand, large stresses can be produced when a large flux of particles of low energy is incident on the film (Region I in figure 3.17). In general, it can be concluded that the bombardment by energetic particles leads to a buildup of compressive stress that increases with increasing ion energy. Therefore the energy and flux of sputtered particles are necessary to explain the deposition stress observed.

# 4

# Experimental techniques

In this chapter, the experimental techniques used for the fabrication and characterization of $TiO_2$ thin films are discussed. An overview on the conventional dc Magnetron Sputtering (dcMS), Ion-Beam Assisted Deposition (IBAD), and High Power Impulse Magnetron Sputtering (HiPIMS) deposition techniques are presented. In addition, analytical and characterisation methods including X-ray diffraction (XRD), atomic force microscopy (AFM), the determination of in-situ stress by the wafer curvature method, and the photoconductivity are also explained.

## 4.1 Sputter deposition techniques

The utilized system in this work is a home made [101] magnetron sputtering deposition setup which is illustrated in figure 4.1. The sputtering chamber is a cylindrical stainless steel chamber evacuated by a Pfeiffer turbo molecular pump backed by a Leybold vacuum pump. The base pressure achieved was approximately $10^{-6}$ mbar. The chamber can be equipped with up to 6 targets each with a size of 75 mm diameter and 6 mm thickness. The rotatable substrate holder plate attached to the top cover opposite to the targets allows for loading of 24 substrates with a maximum size of 76 × 24 mm. A metallic plate (Shutter) with a single hole above the centre of the target is located between the substrate holder and the target. The distance between target and substrate is typically 55 mm. High voltages can be applied to the target through an advanced Energy Pinnacle dc power supply. One channel of the supply is combined with a Melec SPIK 2000 pulser for the HIPIMS process. A *LEM* LA205-S current transducer and a *LEM* CV3-1500 voltage transducer are used to measure the target voltage and the target current respectively. A TDS2014 digital oscilloscope is used to monitor the target current and voltage. The films can be produced in constant current mode; constant power or constant voltage mode. The total pressure is kept constant by varying the argon flow while the desired oxygen flow rate is fixed; the purity grade of both gases is 5N. The gas composition in the chamber is determined by a quadruple mass spectrometer (QMS) connected to the chamber via a differential pressure valve.

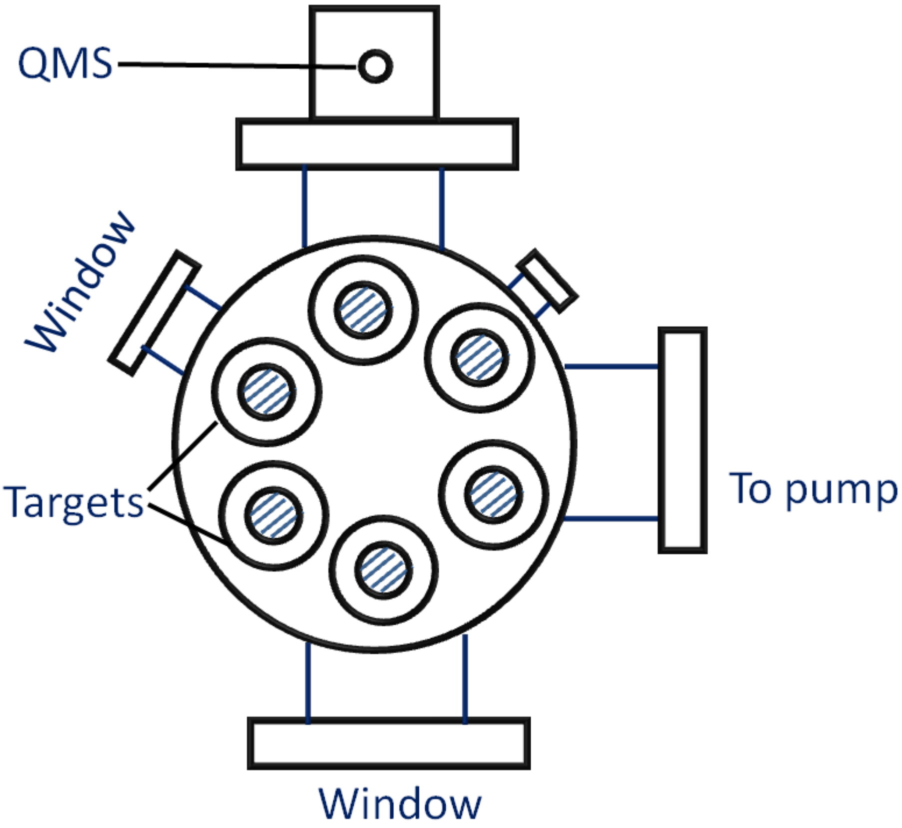

**Figure 4.1:** Schematic drawing of the magnetron sputter chamber. The chamber can be equipped with up to 6 sputter targets.

## 4.2 Ion beam assisted setup

The second deposition tool used to fabricate the $TiO_2$ thin films is the Ion Beam Assisted Deposition (IBAD). The geometry of this technique is shown in figure 4.2. In this system an auxiliary electron cyclotron resonance (ECR) ion source (Tectra Gen II) [102] with an additional pumping stage is installed in the sputter deposition system. It enables simultaneous bombardment of the growing film with ions during the deposition. The ion gun is installed at approximately 45° to provide precise control of energetic ion bombardment. The target to substrate distance is slightly higher in this system (80 mm). A low total pressure of 0.3 to 0.4 Pa is employed for film deposition in this process to ensure appropriate conditions for the operation of the ion gun and a large mean free path for the ions produced. The bombarding species is fed directly into the plasma cup of the ion source. This improves the efficiency of the ionization and the purity of the ion beam. A flat probe is used to measure the ion current at the substrate position, neglecting the small portion of secondary electrons generated by the collision of ions with the probe. This helps to determine the ion flux density $N_{ion}$ using the expression [90]:

$$N_{ion} = \frac{I_{ion}}{F \times \sqrt{2} \times e} \tag{4.1}$$

Where $I_{ion}$ is the measured ion current, e is the elementary charge, F is the area of the flat probe and the factor $\sqrt{2}$ is a geometrical correction taking into account the tilting angle of 45° of the impinging ion beam with respect to the substrate. The flux density of $TiO_2$ molecules $N_{TiO2}$ can be derived from the deposition rate:

$$N_{TiO_2} = R \times \frac{\rho_{TiO_2} \times N_A}{a_{TiO_2}} \tag{4.2}$$

Where R is the deposition rate, $N_A$ is Avogadro’s number, $\rho_{TiO_2}$ is the mass density and $a_{TiO_2}$ is the molar mass of $TiO_2$ respectively. The ratio between the bombarding ion flux density and the flux density of the $TiO_2$ molecules is the relative arrival ratio and is defined as: $r = \frac{N_{ion}}{N_{TiO_2}}$ 4.3

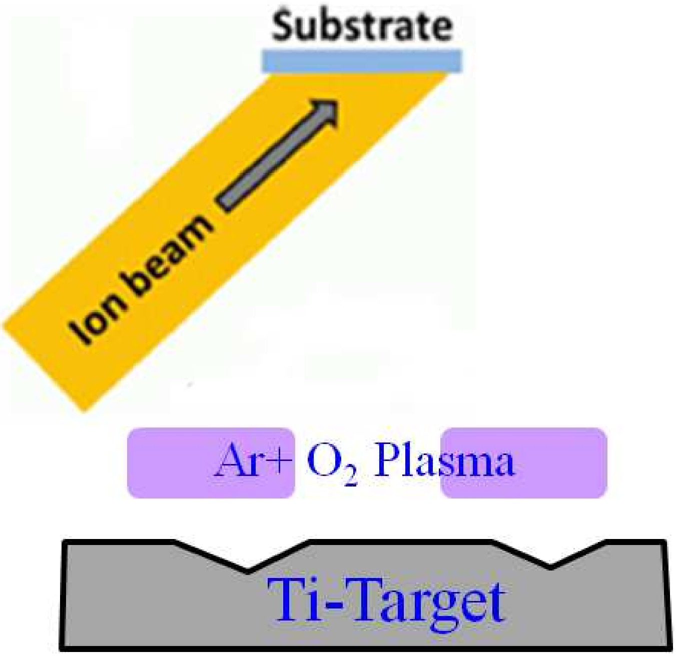

**Figure 4.2:** Geometry of the IBAD process, an auxiliary ion beam gun is installed at an inclination angle of 45° to enable control of the ion bombardment.

## 4.3 Film preparation

$TiO_2$ thin films have been deposited in this work on microscope glass slides and on silicon wafers with (100) orientation. The system has been pumped down to the base pressure of $10^{-6}$ mbar after loading the samples and the required target bonded to the cathode. The target was pre-sputtered in Argon (sputtering gas) for at least 10 minutes to remove any surface oxide from the target.

The determination of the working point, i.e. the appropriate flow rate of the reactive gas, is a prerequisite for sample deposition. Therefore target characterization is required prior to deposition. The characterization has been performed by examining the target behaviour upon increasing and decreasing flow of the reactive gas (oxygen in this work). Sputtering has been performed in a constant current mode. The temperature of the shield between the cathode and the substrate stage was measured for the $TiO_2$ materials used and was found to increase up to 170°C after about 3 h in oxide mode and saturate. Hence in this work, sputtering started after a waiting time of 3 h in the oxide mode to ensure the stability of the temperature during deposition and avoid the influence of temperature variations on the sample structure. By adjusting the suitable sputtering conditions, oxygen flow and the corresponding sputter time, the sputter session was programmed using the sputter software and coating is started.

## 4.4 Analysis of film structure

Investigation of the film properties such as the crystal structure, the crystalline quality, as well as the film topography have been performed utilizing different analytical techniques: XRD, AFM and transmission electron microscope (TEM). An overview on these systems is presented in this section.

### 4.4.1 GI-X-Ray diffraction

The X-ray diffraction pattern provides detailed information about the structural properties of the sample. When crystalline or molecular structures consist of a set of N+1 atomic planes of spacing d exposed to X-rays with incidence angle $\theta$, each atomic plane reflects a small fraction of the incident amplitude. Due to the phase difference between the X-ray photons scattered at each individual lattice plane, a diffraction patterns obtained (constructive and destructive interference). The interference is constructive when the path difference of two parallel beams diffracted by parallel crystal planes is an integer multiple of their wavelength. This condition is expressed by:

$$n\lambda = 2d\sin\theta \tag{4.4}$$

Where n is an integer, d is the spacing between the planes in the lattice, and θ is the angle of the lattice planes with respect to the incident X-ray beam of wavelength λ. Equation 4.4 is referred as Bragg's equation (W.L. Bragg (1912)) [103]. A schematic representation of Bragg diffraction is shown in figure 4.3.

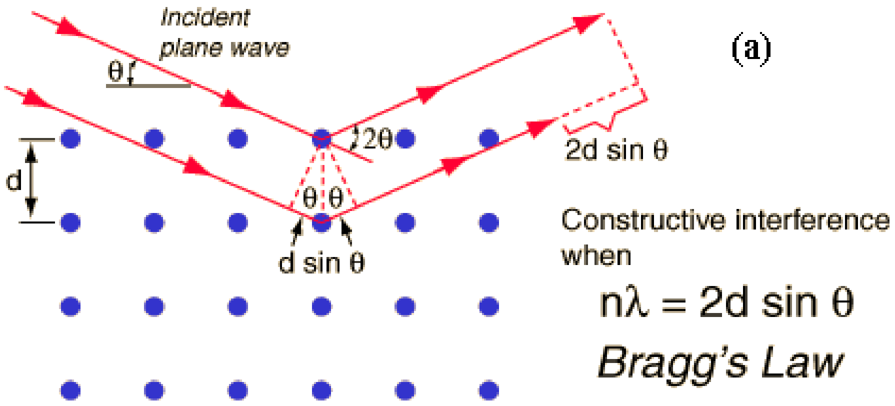

**Figure 4.3:** Schematic representation of Bragg diffraction at crystal planes with inner planar spacing $d_{hkl.}$

The lattice constants or d-spacing, the lattice symmetry and the dimensions of the unit cell are determined by inserting the measured angular position θ in Bragg's equation. From the d-spacing, phases are identified by using the JCPDS (Joint Committee for Powder Data Standards) Powder Diffraction File. The reflections can then be indexed by Miller indices.

X-ray diffraction can be used for the determination the grain size in the polycrystalline film. When the size of the individual grain is less than $10^{-5}$ cm (100nm), this leads to peak broadening, and the extent of the broadening given by:

$$B = \frac{0.9\lambda}{t\cos\theta} \tag{4.5}$$

Equation 4.5 is known as Scherrer equation [104], *B* is the broadening of the diffraction peak given by the full width at half maximum (FWHM) and *t* is the grain size.

X-ray diffraction is a very important experimental technique which is used to address all information related to the crystal structure of the material, including lattice constants, identification of unknown materials, preferred orientation of polycrystals and stresses.

Different x-ray diffraction geometries can be employed to investigate the film structure. In the course of this work, a Philips X’ Pert Pro MRD diffractometer (45kV, 40 mA) equipped with a Cu Kα radiation source that provides an X-ray beam of wavelength ~ 1.54 A° (figure 4.4) has been utilized. The x-ray source is fixed and both the detector and the sample stage are automatically moved to allow for different measurement geometries. The diffractometer’s setup can be grouped into three parts: at the incident beam line (right hand side), the x-ray beam is produced and its divergence is adjusted in an appropriate way for the respective measurement. The Eulerian cradle (middle) is used for the positioning of the sample whereas the secondary optics allows the adjustment of the detector’s position. The GI-XRD scans were performed by using the PW 3011/2 detector, which is a Xe filled proportional counter and provides high angular resolution

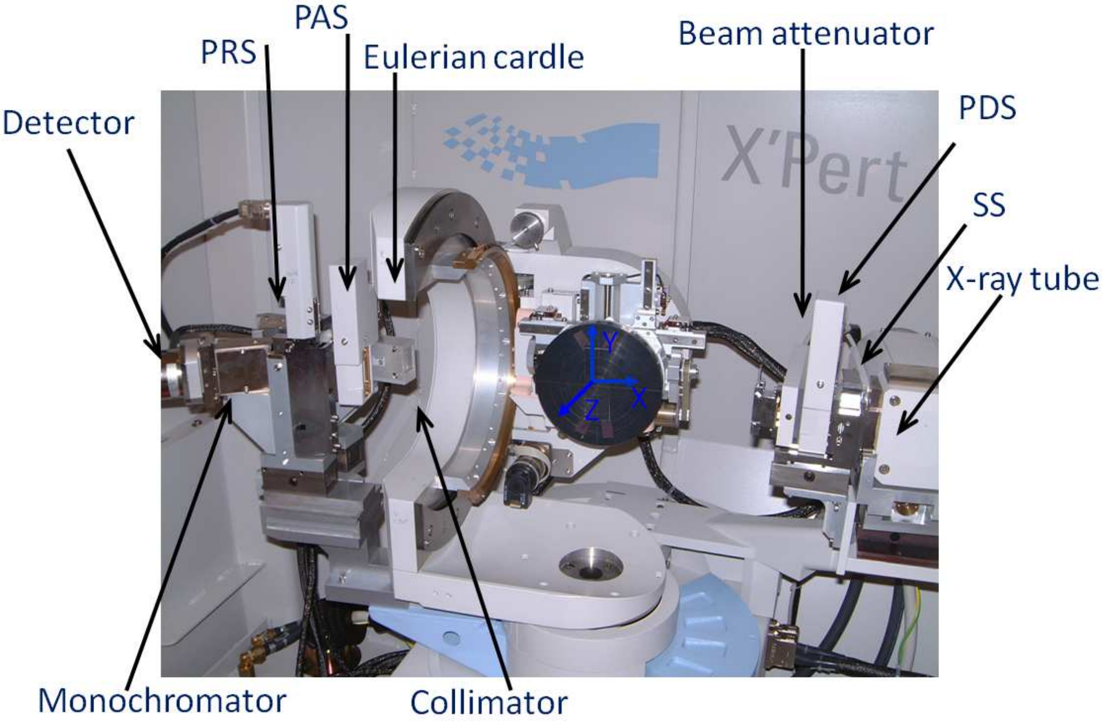

**Figure 4.4:** The *Philips* X’PERT PRO x-ray system. The acronyms designate the Soller slit (SS), the programmable divergence slit (PDS), the programmable receiving slit (PRS), and the programmable anti-scatter slit (PAS).

The machine has been utilized in two different geometries to investigate the structure of the $TiO_2$ thin films in this work:

(i) Grazing incidence geometry (GI): in this case, the sample angle is kept constant ($\omega = 0.7°$ for $TiO_2$ films) and the detector is moving around the detector circle’s centre, i.e. $2\theta$ is varied.

This allows for the irradiation of a very large area of the sample and most of the beam is diffracted inside the film. This geometry is widely used for the investigations of polycrystalline films with low orientational order, figure 4.5(a).

(ii) Rocking curve geometry: the diffraction angle of a specific peak is fixed (e.g. anatase (101) and rutile (110) phases in $TiO_2$ films) by the position of the detector. The sample angle is varied around $\omega = \theta$, as shown in figure 4.5(b).

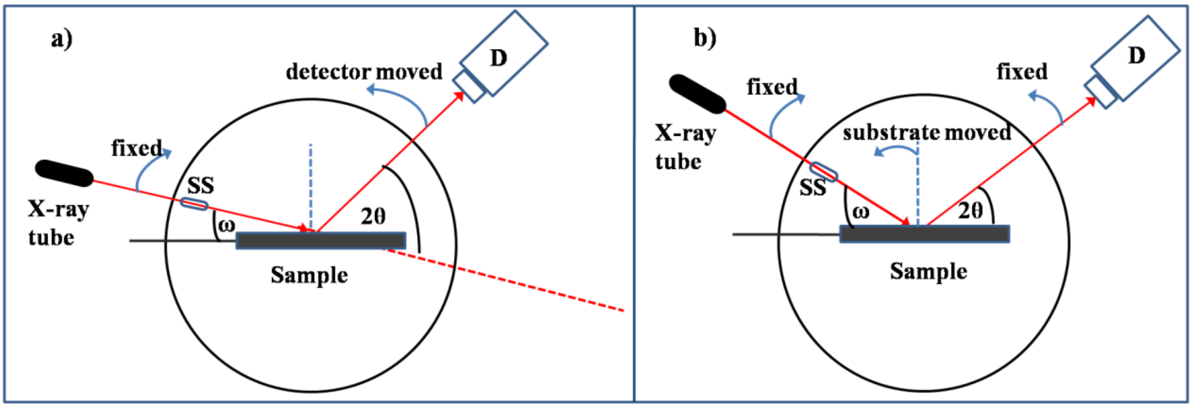

**Figure 4.5:** Schematic representation of the (a) grazing incidence geometry: the angle between the incident beam and the substrate is fixed (0.7° for $TiO_2$ films) and the detector is moved only (b) rocking curve XRD geometry: the sample is rotated while the detector is fixed at the diffraction angle of a specific peak (anatase (101) and rutile (110) in $TiO_2$ films). The letter D represents the detector and (SS) stands for the Soller slit.

### 4.4.2 Atomic Force Microscopy (AFM)

Atomic force microscopy is a very high-resolution type of scanning probe microscopy. AFM provides a 3D profile of the surface on a nanoscale by measuring forces between a sharp tip and the surface at very short distance (0.2-10 nm probe-sample separation).The surface topography of the $TiO_2$ samples in this work was investigated employing a Digital Instruments Dimension 3100 Nanoscope in the tapping operation mode. The scanning has been performed by using a nanoscopic tip with a radius of 10 nm which is located at the end of a cantilever as shown in figure 4.6. The scan head is moved along the x-y-z direction by piezo transducers.

When the tip is brought into proximity of the sample surface, forces between the tip and the sample lead to a deflection of the cantilever according to Hooke's law. A detector measures the cantilever deflection as the tip is scanned over the sample. The deflection is measured using a laser spot reflected from the top surface of the cantilever into an array of photodiodes. The measured cantilever deflections allow a computer to generate a map of surface topography. Several forces typically contribute to the deflection of an AFM cantilever. The most commonly present force associated with an AFM is an interatomic force called the van der Waals force. This force depends critically upon the distance between the tip and the sample.

There are three primary imaging modes in AFM (contact mode, tapping mode and non-contact mode). In tapping mode, the probe-surface separation is very small (0.5-2 nm). The cantilever is driven to oscillate up and down at near its resonance frequency by a small piezoelectric element mounted in the tip. The interaction with forces acting on the cantilever when the tip comes close to the surface causes the amplitude of this oscillation decrease as the tip gets closer to the sample. By maintaining a constant oscillation amplitude, the tip-sample interaction is kept constant and an image of the surface is obtained.

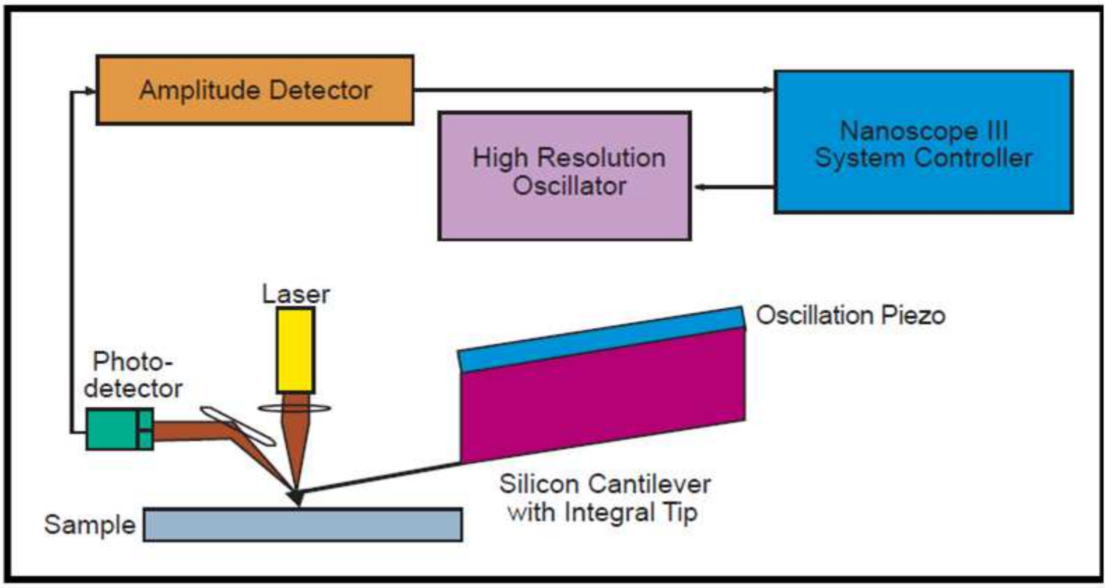

**Figure 4. 6:** Principle of AFM operation in the tapping mode. The surface is scanned by using a tip with a radius of around 10 nm. The tip oscillates and scans the film surface in x-y-direction.

### 4.4.3 Transmission Electron Microscopy (TEM)

Transmission electron microscopy (TEM) is used to obtain structural information from the samples that are thin enough to transmit electrons. In the course of this work, TEM measurements of selected $TiO_2$ films have been performed with a Tecnai F20 operated at 200 kV at the Ernst Ruska Center for Electron Microscopy at the Forschungszentrum Jülich. Preparation the TEM sample has been performed by standard techniques, involving mechanical grinding, dimpling and Ar ion milling. Bright-field images and dark-field diffraction contrast images have been recorded to investigate the microstructure of the sample.

TEM uses electrons and their much lower wavelength makes it possible to get a resolution a thousand times better obtained with a light microscope. Electrons are thermally emitted from the gun and are accelerated to 100keV or higher. The electron beam is projected onto the specimen by a condenser lens system as shown in figure 4.7. The electrons experience a variety of scattering processes during their passage through the sample. Elastic scattering which gives rise to diffraction patterns is important for TEM. The diffracted electron beams and the primary beam pass through a series of post-specimen lenses which leads to the production of the image of the sample. Images can be formed in several ways. The first mode is the bright-field image which is obtained by blocking all diffracted beams by placing apertures in the back focal plane of the objective lens and allowing the central transmitted beam only. The second mode is the dark-field image which is formed by selecting one of the diffracted beams for imaging.

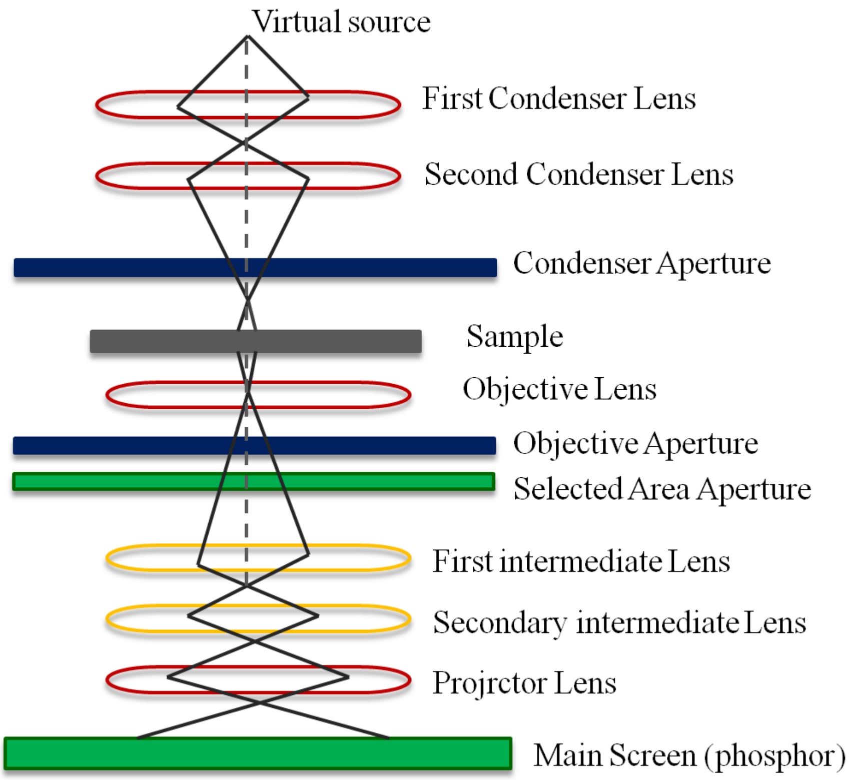

**Figure 4.7:** Principle of the transmission electron microscopy (adopted from [105]).

## 4.5 Optical properties and film thickness

In this work, the optical spectra have been used to determine the thickness of the sputtered $TiO_2$ thin films. This has been done by measuring the ellipsometric optical spectra, the transmittance and reflectance spectra. Then by applying an adequate description of the dielectric function utilizing the SCOUT software, these spectra have been modelled. This leads to determination of the optical properties and the thickness of the investigated films. In this section, the techniques used and the modelling method for the determination of the film thickness are discussed.

### 4.5.1 Spectroscopic ellipsometry

Spectroscopic ellipsometry is a very sensitive optical technique devoted to the analysis of the surfaces and the determination of the optical constants, roughness, thickness of the thin films and other properties with an impact on the optical response. It is based on the measurement of the variation of the polarization state of the light after reflection from a planar surface. The light reflected at the sample surface is generally elliptically polarized. The reflected light undergoes phase changes that are different for different electric field components; polarized parallel (p) and perpendicular (s) to the plane of incidence. Ellipsometry measures this state of polarization; the measured response depends on optical properties and thickness of individual materials. The amplitude and phase shift of the *p* and *s* components are described by two ellipsometric angles $\psi$ and $\Delta$. These angles are correlated with the Fresnel coefficients for the *s*- and *p* polarized fractions ($R_s$, $R_p$) of the reflected light by [106]:

$$\tilde{\rho} = \frac{\tilde{R}_p}{\tilde{R}_s} = \tan\psi . \exp(i\Delta) \qquad 4.6$$

The Fresnel coefficients are related to the optical constants of the surface and expressed by:

$$\tilde{R}_p = \frac{\tilde{n}_2 \cos\phi_1 - \tilde{n}_1 \cos\phi_2}{\tilde{n}_2 \cos\phi_1 + \tilde{n}_1 \cos\phi_2}, \tilde{R}_s = \frac{\tilde{n}_1 \cos\phi_1 - \tilde{n}_2 \cos\phi_2}{\tilde{n}_1 \cos\phi_1 + \tilde{n}_2 \cos\phi_2} \qquad 4.7$$

Where $\tilde{n}_1$ and $\tilde{n}_2$ are the complex indices of refraction of two media, while the angles $\phi_1$ and $\phi_2$ are the angle of incidence and refraction, respectively.

In this work, the ellipsometric measurements of $TiO_2$ thin films were performed using a Wollam M2000-UI rotating compensator ellipsometer. The instrument employs electromagnetic radiation in the spectral range of 0.53-5.13 eV (1700 nm to 250 nm), utilizing halogen (NIR/VIS) and deuterium (UV) lamps for illumination. Detection is performed by an InGaAs diode array (NIR) and CCD array camera that enables the simultaneous measurements of all wavelengths in the spectral range. The fixed polarizer has an azimuth angle of 45° with respect to the plane of incidence and polarizes the incident light equally to the *s* and *p* directions. The compensator is a retarder which induces a phase shift between the two components of the electric field. A second fixed polarizer (analyzer) is used after the sample in order to polarize linearly the reflected beam. The arrangement of the optical components in the beam path is shown in figure 4.8. The resulting spectra have been fitted by the OJL model using a SCOUT program (section 4.5.3).

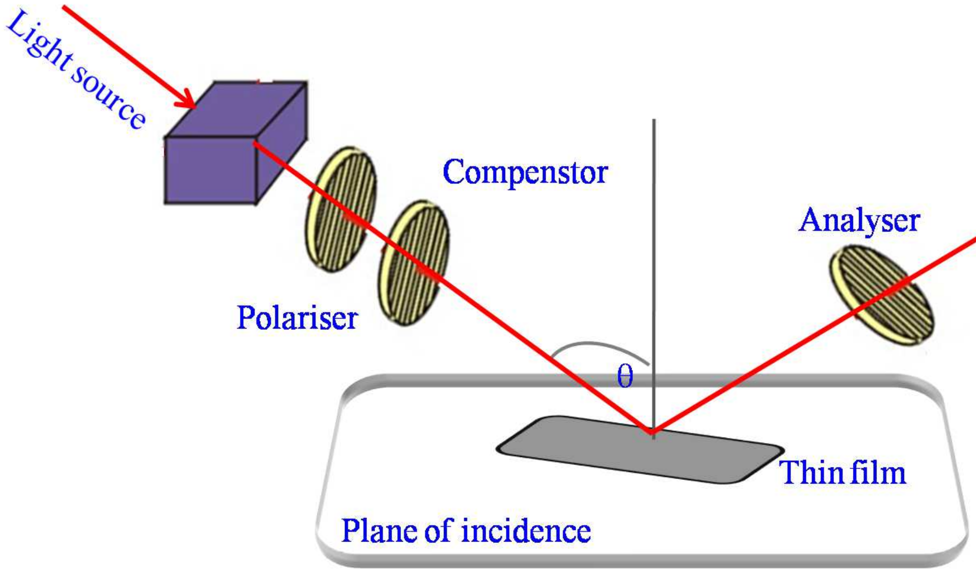

**Figure 4.8:** Arrangements of the optical components in Woollam M2000-UI rotating compensator ellipsometer.

## 4.5.2 Reflectance and transmittance

The reflectance and transmittance spectra in this work have been measured using a Perkin Elmer Lambda 25 UV/VIS spectrometer in the range from 190 to1100 nm (1.13- 6.53 eV) [107]. The instrument is equipped with Deuterium and Tungsten light sources. A sputtered aluminum film has been used as a reference sample for the reflectance measurements.

The measurement of the reflectance and transmittance in the NIR/Vis/UV range is based on the interaction of electromagnetic radiation with the electrons of the material. When a light beam impinges on an optical medium, some of the incident light is reflected from the front surface, while the rest enters the medium and propagates through it. The reflection is defined by the coefficient of reflection (R) which is the ratio of the amplitude of the reflected wave to the amplitude of the incident wave. Also, the transmission coefficient (T) which is used to define the transmission is the ratio of the amplitude of the transmitted beam to the amplitude of the incident one. This can be described by: $R+T=1$ if there is no absorption or scattering. The propagation of the beam through the material is accompanied by a change in the wave velocity and this is described by the refractive index which depends on the frequency of the light beam.

### 4.5.3 Modeling of the dielectric function

Modeling the ellipsometry spectra as well as the reflectance and transmittance data has been performed with an adequate description of the dielectric function (OJL interband transition) model [108] by the SCOUT software [109]. OJL is an elementary empirical model for the distribution of electronic states of an amorphous semiconductor, which captures the basic features expected. In an amorphous semiconductor, a tail in the absorption spectrum extends into the gap region. On the other hand, in a defect-free crystalline semiconductor, the absorption spectrum terminates abruptly at the energy gap.

It is recognized that the distribution of states exhibits a square-root functional dependence in the band region and an exponential functional dependence in the tail region. Hence, expressions for the density of states (DOS) are assumed which contain tail states exponentially decaying into the band gap, as shown in figure 4.9. The original parameters of the OJL density of states model are the energies $E_V$ and $E_C$, the 'damping constants' of the valence and conduction band $\gamma_V$ and $\gamma_c$ respectively as well as the masses of the valence and conduction band $m_V$ and $m_C$. The mobility edges of the valence and conduction band are expressed as [108]:

$$E_{MobV} = E_v - \frac{1}{2}\gamma_V, E_{MobC} = E_c + \frac{1}{2}\gamma_c, \qquad 4.8$$

The mobility in the OJL model is therefore given by: $E_c + \frac{1}{2}\gamma_c - \left(E_v - \frac{1}{2}\gamma_V\right)$

In the case of an amorphous semiconductor, the momentum is a poor quantum number. Hence the optical absorption coefficient can be expressed as:

$$\alpha(\hbar\omega) = D^2(\hbar\omega)J(\hbar\omega) \qquad 4.9$$

Where $J(\hbar\omega)$ denotes the joint density-of-states (JDOS) which combines the density of states of the valence and conduction band. $D^2(\hbar\omega)$ is the optical transition matrix element. At low temperatures and by assuming independent conduction-band and valence-band potential fluctuations, this JDOS function may be expressed as:

$$J(\hbar\omega) = \int_{-\infty}^{\infty} N_c(E) N_V(E - \hbar\omega) dE \qquad 4.10$$

The integration collects all possible transitions from the valence –to- conduction band with energy separation equal to the energy of the absorbed photon.

In an amorphous semiconductor, the absorption tail is often assumed to exhibit a linear-exponential functional dependence on the photon energy, i.e.

$$\alpha(\hbar\omega) = \alpha_0 \exp\left(\frac{\hbar\omega - \hbar\omega_0}{E_0}\right) \qquad 4.11$$

Where $\alpha_0$ and $\hbar\omega_0$ are numerical constants. $E_0$ is referred to as the absorption tail width which is commonly used to characterize the absorption edge of an amorphous semiconductor.

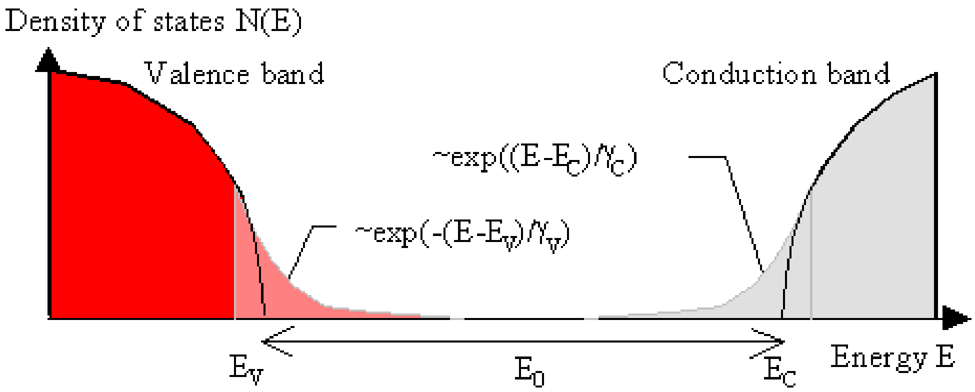

**Figure 4.7:** Description of OJL interband transition model, it is assumed to possess parabolic bands with tail states exponentially decaying into the band gap.

SCOUT [109] is software for the analysis of optical spectra by comparison of measurements and models. It is mostly used to analyze many measured spectra simultaneously. It has the advantage of automatic fitting of model parameters like film thickness or gap energies to adjust simulated to measured spectra.

## 4.6 In-situ stress measurements by wafer curvature method

The precise determination of the magnitude of the residual stress in thin films provides valuable information on the growth mechanism. The wafer curvature method which is based on measurement of the substrate's curvature enables the direct determination of the stress in the film [110]. The biaxial (plane) stress in the film can be calculated using Stoney's equation:

$$\sigma = \frac{1}{6}\frac{E_s t_s^2}{(1-v_s)t_f}\left(\frac{1}{R}-\frac{1}{R_0}\right) \qquad 4.12$$

Where, $R$ and $R_0$ represent the curvature of the substrate before deposition and during deposition, respectively. $t_s$, $t_f$ are the thicknesses of the substrate and the film respectively and $E_s/(1-v_s)$ denotes the biaxial elastic modulus of the substrate.

In the course of this work, the mechanical stress of the $TiO_2$ thin films has been investigated by means of an in-situ wafer curvature method [111]. A homemade setup is utilized where two parallel laser beams are used to determine the curvature of the substrate. The principle of the setup is schematically shown in figure 4.10.

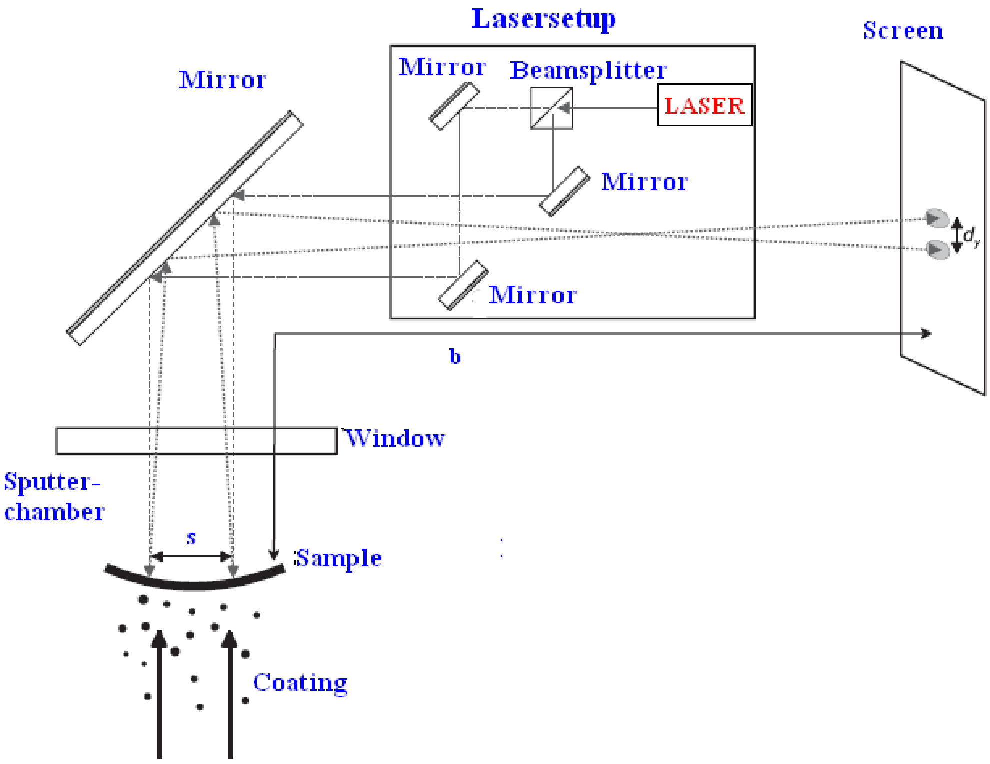

**Figure 4.8:** Schematic drawing of the wafer curvature setup. The laser beam is split into two individual beams and directed onto the backside of the sample on which a film is deposited.

In the setup, a laser beam is generated by a single HeNe laser diode. The laser beam is separated by a beam splitter into two individual beams, which are parallelized by a set of three mirrors. The two parallel laser beams are then guided into the chamber and are reflected by the back of the sample. The reflected laser beams are analyzed by a standard webcam outside the machine which records the laser beam on a screen every tenth of a second. The screen consists of a wood frame in which a smooth transparent paper is stretched and mounted on an optical bench located a few meter from the setup. A camera (Logitech QuickCam Pro 4000) with a charge-coupled device (CCD) chip with noise reduction was used. The position of the two laser spots on the screen is determined by image processing software realized in LABVIEW. The curvature of the sample can then be calculated from the distance of the laser beams on the screen using the geometrical properties of the system. The stress measurements have been carried out on ultrathin silicon substrates (180 µm) covered by a layer of silicon oxide.

## 4.7 Photoconductivity

Irradiation of the $TiO_2$ film with light of energy above the energy gap leads to the generation of electron hole pairs and a significant increase of the conductivity. The generation of the charge carriers takes place within a few femtoseconds ($10^{-12}$ s) [112]. These free charge carriers can recombine with each other within a few nanoseconds ($10^{-9}$ s) or are trapped at defects. Oxygen defects are the most common impurity in $TiO_2$ and act as attractors for the photo-generated holes. The trapped holes exert only a small electromagnetic attraction to the free electrons and thus trapped at the negative oxygen defects. However, there are other imperfections that result from lattice defects or interstitials which have different energy levels and charges. They can also serve as traps or as recombination centers. The gradual occupation of the impurities with holes (trapping) leads to the saturation behavior of the photocurrent. The saturation rate depends on the number of available traps compared to the carrier concentration in the film. Increasing the carrier concentration can be done by increasing the light intensity [55], since high intensity leads to the generation of more charge carriers. When the trapped holes are excluded from recombination with the electrons, the concentration of free electrons is increased and thereby the conductivity of the $TiO_2$ films increased. It has been found that the photoconductive properties of $TiO_2$ are strongly depending on the ambient environment. This has been explained by a loss of adsorbed oxygen from the surface. Oxygen acts as a scavenger for the photogenerated electrons and its removal extends the electron lifetime and leads to large saturation of the photocurrent, i.e. removal of conduction electrons by adsorbed $O_2$ to form adsorbed $O_2^-$ [53, 54, 55], as illustrated in the following equilibrium:

$$O_2(g) \Leftrightarrow O_2(ads)+e^-(solid) \Leftrightarrow O_2^-(ads) \tag{4.13}$$

In the course of this work, the photoconductivity measurements have been carried out using a 4200-SCS Keithley setup. The electrical contacts to the film have been achieved through two metallic needles connected to the sample edges where two Ti contact electrodes have been deposited by sputtering. The temperature of the sample can be changed using Peltier elements in the range from -50°C to 120°C which allows measurements of the photoconductivity at different temperatures. To avoid condensation on the sample surface and to create a reproducible experimental environment during the measurement, the sample is covered by an acrylic glass. This cover is made of a glass plate and during the measurement flushed with argon or oxygen to study the effect of different atmospheres on the photoconductivity. The absorption spectrum of this glass shows good transparency in the visible range down to 300 nm and therefore the photocatalytic activity of $TiO_2$ is not affected. The setup is shown in figure 4.11.

.

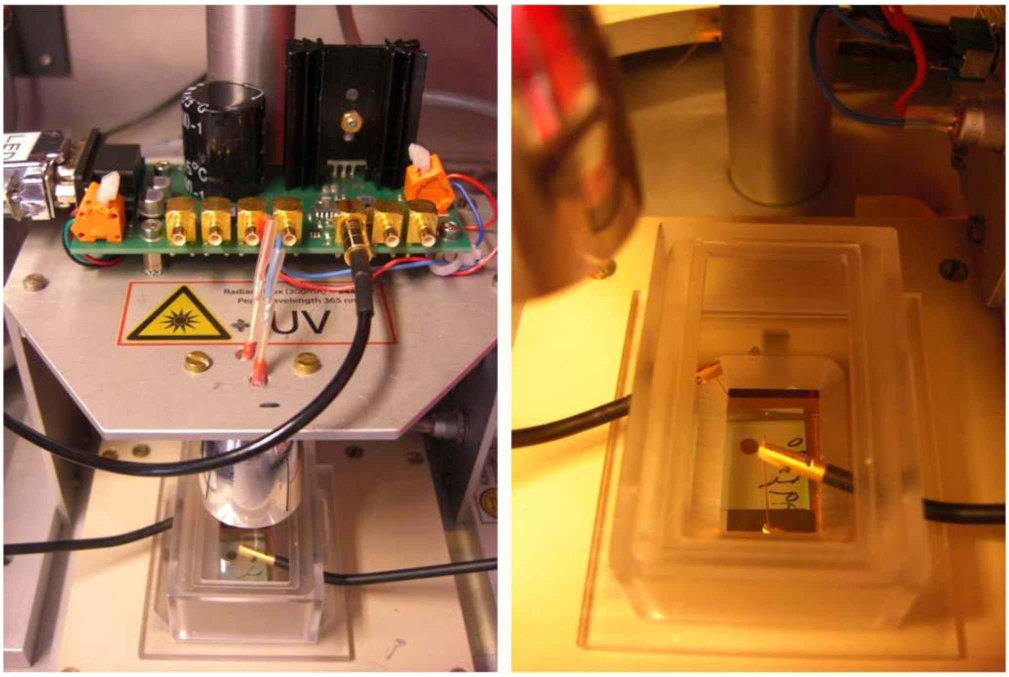

**Figure 4.9:** The photoconductivity setup. The needles which are connected to the top electrodes of the sample appear in the right side while on the left side the UV-LED lamp is visible which is used to irradiate the sample.

A LED lamp (OLTH-0480-UV, laser components) is used as the UV source to irradiate the films. It consists of 50 individual LEDs, which are combined in an array. To reduce the large viewing angle of the LED, a parabolic collector is used to focus the light in an angle of +/-30°. The LED and the controller board are mounted on a holder which can be positioned over the sample. The distance to the sample is selected so that the total light intensity will be incident on the sample. The maximum light intensity is 244 mW. This light intensity is switched on or off electronically via an electrical input. Finally the (photo-) current is measured as a function of time.

# 5

# The influence of energetic particles on the structure of reactively sputtered $TiO_2$ thin films

In the preceding chapters, we have mentioned that $TiO_2$ thin films have a wide range of applications which depend on the crystalline structure of this material. Therefore, the precise control of the film structure is a key requirement to tailor the performance of the film for the targeted application. As also mentioned, this work aims to understand the mechanism of the structure evolution as a function of the different process parameters. The investigation of the structure of the sputtered $TiO_2$ thin films as a function of the energetic particles parameter is presented in this chapter.

## 5.1 Target characterization and deposition characteristics

In order to achieve our task, $TiO_2$ thin films have been deposited using different sputtering techniques such as conventional dcMS and HiPIMS. The determination of the working point and the appropriate conditions for each process are required. This has been performed by recording the variation of the target voltage as a function of increasing and decreasing oxygen flow “Target characterisation”. Figure 5.1 shows the hysteresis curve for a Ti target using conventional dcMS and HiPIMS at different pulse configurations 50/450 and 50/950 µs. The total sputtering pressure was kept constant at 0.8 Pa and the discharge current at 0.9 A. As mentioned in section 4.3, pre-sputtering for 3 hr in the oxidic mode is required to ensure stability of the temperature during deposition. From these measurements, the following remarks can be made:

- A pronounced hysteresis is observed by employing the dcMS process, while it is reduced by applying HiPIMS.
- For dcMS, the cathode potential is gradually increased until a certain critical oxygen flow is reached (transition point at 4.5 sccm) which corresponds to a fully oxidized target. This transition is accompanied by a sudden increase of the secondary electron emission yield [113]. Beyond this transition the discharge voltage remains almost constant.

- On the other hand, the transition point is shifted to a lower oxygen flows for HiPIMS. The width of the hysteresis area is reduced and almost eliminated as also observed for an Al target [114].
- The change in the voltage from metallic mode to oxidic mode is smaller for HiPIMS in comparison to dcMs mode. Also, the target voltage increased when the duty cycle was decreased, i.e. when the pulse –off time was increased from 450 to 950 µs. This is attributed to the change in the target's surface stoichiometry (target coverage), i.e. increase in the Ti fraction on the target surface. This is explained by the effect of gas rarefaction which is the depletion of Ar and $O_2$ species in the target vicinity due to collisions with energetic sputtered atoms. The gas rarefaction in HiPIMS increases with the peak target current which results in less available $O_2$ for oxidization of the target during the pulse on-time. The increase in the target voltage upon changing the pulse configuration leads to an increase in the mean ion energy which may affect the target sputtering yield [115].

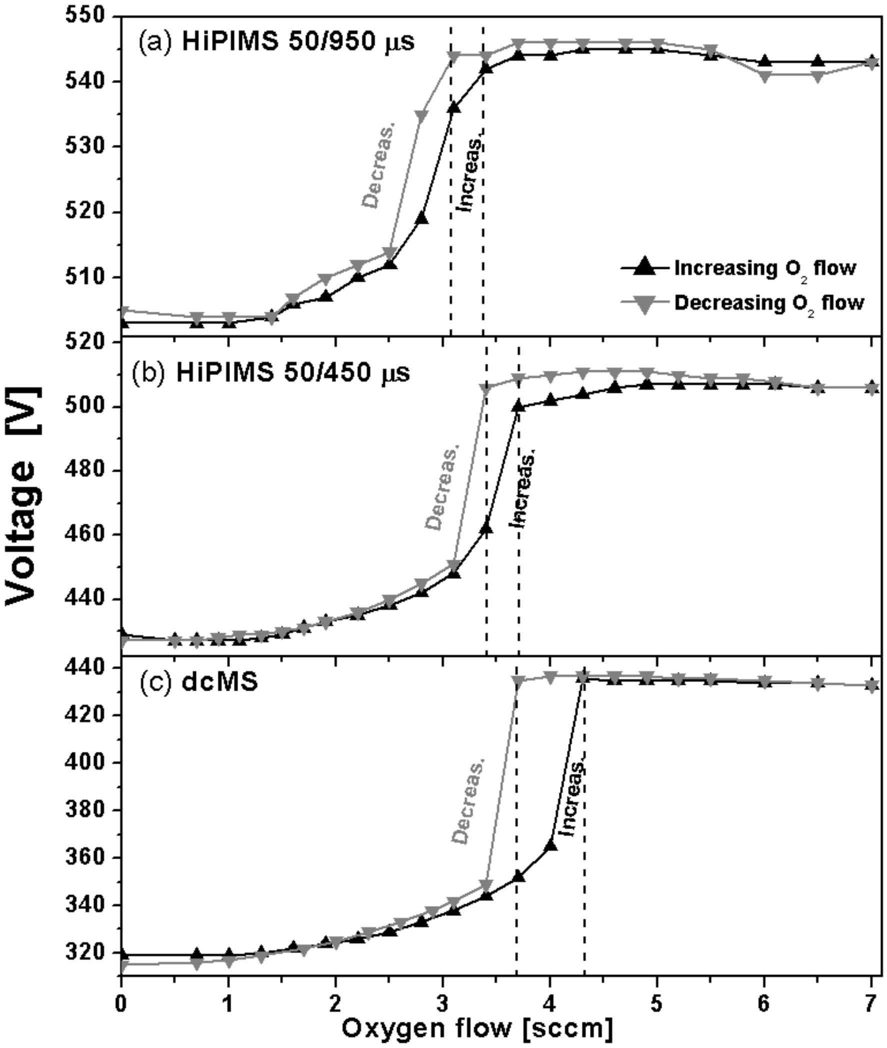

**Figure 5.1:** Influence of the oxygen flow rate on the discharge voltage of $TiO_2$ films at constant discharge current of 0.9 A and working pressure of 0.8 Pa by employing (a) dcMs, (b)HiPIMS 50/450 μs and (c) HiPIMS 50/950 μs processes. The dashed lines represent the width of the hysteresis region. The hysteresis is almost eliminated by HiPIMS while a pronounced hysteresis is observed for dcMS process.

The actual deposition rate which is determined by dividing the film thickness by the sputter time shows significant differences for the different sputtering processes, as presented in figure 5.2. For dcMS mode, as the oxygen gas is introduced, the deposition rate initially increases gradually in the metallic mode. This is followed by a sudden drop during the transition region to approximately ≈ 0, 2 nm/s. As the oxide compounds starts to form on the target surface, a gradual decrease is observed until it a low value of ≈ 0, 08 nm/s is reached at high oxygen flow. This is attributed to a drastic decrease in the sputtering yield.

On the other hand, a lower deposition rate values with the same behaviour is observed by using HiPIMS mode with different pulse configurations. The loss of deposition rate in HiPIMS is attributed to the self-sputtering phenomenon, i.e. sputtering of the target by ionized sputtered species [79].

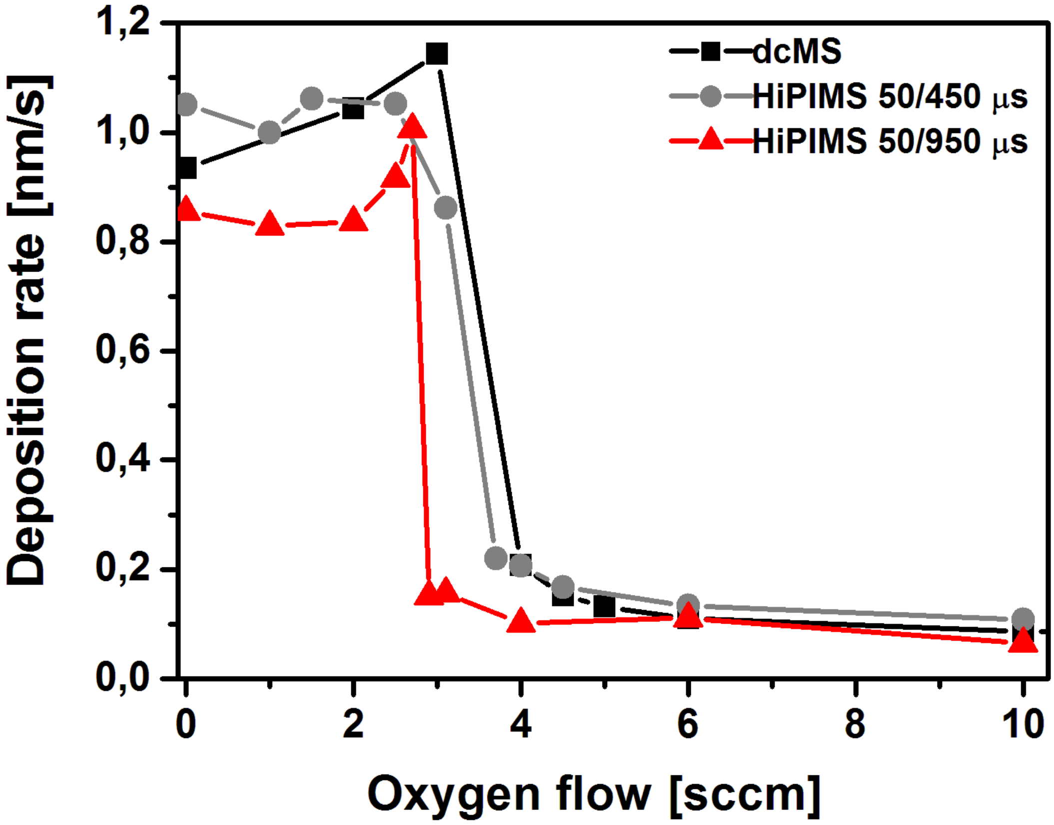

**Figure 5.2:** Variation of the deposition rate as a function of oxygen flow of $TiO_2$ thin films deposited at constant working pressure of 0.8 Pa and discharge current of 0.9 A employing dcMs and HiPIMS 50/450 µs. A lower deposition rate is observed for HiPIMS process than dcMS.

## 5.2 Role of energetic particles during film growth

As already presented in section (2.2), significant efforts have already been undertaken to understand the structure formation of sputtered $TiO_2$ thin films. These studies have focused on an investigation of the structure formation as a function of various process parameters such as total pressure, oxygen partial pressure, substrate temperature, film thickness, magnetron configuration and electrical discharge properties including the ion bombardment of the substrate. Regarding the influence of the deposition parameters on the structure formation there is a consensus throughout most publications that energetic particle bombardment is one of the most important parameters governing phase formation. However, there does not seem to be a consensus about the bombarding species, their required energies and finally about the exact mechanism by which the phase formation is triggered as a function of bombardment. Moreover, most studies even ignore the role of highly energetic negatively charged oxygen ions. Although the marked influence of negative oxygen ion bombardment inherent in the sputter discharge has been shown already for a variety of materials [48-50, 116-118], it is often disregarded in the structure formation of sputtered $TiO_2$ films.

Instead, many authors conclude that low energy ion bombardment due to positive ions accelerated by the differences in plasma and substrate potentials is the main contributor to phase formation. On the other hand, several investigations of deposition processes different from sputtering exist that clearly show the importance of the high-energy ion bombardment on $TiO_2$ structure formation. Amongst these studies are investigations of oxygen ion-assisted evaporation of $TiO_2$ [32], ion beam dynamic mixing [36] and reactive ion cluster beam evaporation [119,120] which have in common a strong energetic ion bombardment of the growing films. In contrast, other techniques such as electron beam [37, 121] and vacuum arc plasma evaporation [33] typically lack strong energetic particle bombardment. Hence, comparing the resulting film structure if methods of deposition are chosen where the energetic bombardment is either pronounced or very low enables the conclusion that, if the films are crystalline, anatase films are grown without intense ion bombardment, while strong ion bombardment promotes the growth of the rutile phase. However, only very few studies exist on sputtering of $TiO_2$ that discuss the existence of highly energetic oxygen ions created at the sputter target surface and their possible influence on film properties (e.g. [28, 37, 122]). Therefore, it is our main goal to demonstrate:

(i) The influence of energetic ion bombardment (i.e. with energies significantly larger than typical plasma potentials) and to show that it is responsible for the effects that are often attributed to low energy bombardment,

(ii) that there are distinct fingerprints in the properties of reactively sputtered $TiO_2$ films which provide both an unambiguous proof for the existence of highly energetic negative ions and clarify the influence of these particles on film properties and

(iii) that the action of these negative oxygen ions can be controlled to yield desired film properties by means of, e.g., ion-assisted reactive dcMS, tailoring of target or chamber geometry and HiPIMS.

To achieve this goal, we first investigate the properties of $TiO_2$ films fabricated by the ion-assisted dc magnetron sputtering (IBAD) process under additional tailored ion bombardment. From these experiments we deduce the typical fingerprints of the influence of energetic ion bombardment on structure formation. This allows for identifying the possible action of energetic particle bombardment in the dcMS and HiPIMS processes.

Unambiguous proof that $O^-$ is the dominant bombarding species in these processes is possible since the existence of these ions in reactive sputter processes has been confirmed and their impact on the structure formation in reactive sputter processes has been investigated for a variety of materials. It was first proven by Tominaga *et al* by utilizing time-of-flight measurements during sputtering of ZnO that oxygen ions with energies equivalent to approximately the full cathode potential [93] strongly influence structure formation [94]. These ions are created at the target surface from collisions with the sputtering species. A possible formation mechanism is discussed in [123]. This mechanism characterizes the sputtered $O^-$ ions and the secondary electron emission from Al by describing the low-energy sputtering process in terms of an electronic excitation followed by desorption. This excitation/desorption mechanism together with the collision cascade generate an ion kinetic energy distribution of the secondary electrons and the sputtered $O^-$ as a function of the oxygen coverage and impact energy. It also implies a correlation between the emission yield of negative oxygen ions and secondary electrons. This correlation has been shown in a comprehensive investigation of oxygen ion energies and emission intensities for a large variety of sputtered metal oxides by utilizing energy-resolved mass spectrometry [124]. The existence of highly energetic negative oxygen ions for sputtering group IV transition metal oxides has been demonstrated for Ti [125], Zr and Hf [48] where in the latter case it has also been shown that the emission intensity is strong compared, e.g., with group V transition metal oxides. The strong influence of energetic oxygen ion bombardment on structure formation has been demonstrated, e.g., for $ZrO_2$ [116, 126]. Interpreting the results summarized in [124] there seems to be a trend that oxygen ion emission is largest for alkali and alkaline earth metal oxides and decreases with increasing valence for the transition metal oxides. Since Zn has a low valence of 2 this trend is also consistent with the fact that sputtered ZnO films show strong damage due to energetic oxygen ion bombardment. For this material it was also demonstrated that the trajectories of the negative oxygen ions are strongly governed by the geometry of the racetrack and therefore by the age of the target [50]. This is a consequence of the creation of these ions directly at the target surface and the subsequent acceleration in the very narrow cathode sheath where the electric potential gradient is almost perpendicular to the target surface even at the racetrack. Consequently, this correlation between negative ion trajectories and the target profile is universally valid and not restricted to ZnO. For this reason, any dependence of $TiO_2$ film properties on the age of the target provides strong evidence for an influence of energetic negative ion bombardment originating from the target surface.

## 5.3 Crystal structure and surface topography of sputtered $TiO_2$ thin films

$TiO_2$ films have been firstly deposited employing different sputtering techniques such as ion beam assisted IBAD, conventional dcMS under different geometrical conditions and by HiPIMS at various sputtering conditions. Then the crystal structure and the surface topography of the fabricated films have been investigated in order to demonstrate the influence of the energetic ion bombardment on structure formation. In this section, the investigations of the film structure using grazing incidence X-ray diffraction and the surface topography by atomic force microscopy for the sputtered $TiO_2$ films at different conditions are discussed.

### 5.3.1 Prepared by ion- assisted reactive dcMS

Ion bombardment can influence film growth by a variety of different mechanisms. Preferential damage of specifically oriented grains for example would strongly depend on the angle of incidence and the texture of the film. The energy and inertia of the bombarding species should generally determine the balance between implantation, densification and sputtering effects. Even chemical reactions can occur if a reactive ion species is used such as in the case of oxygen ion bombardment of $TiO_2$ films.

Since the deposition tool utilized does not allow for a change of the angle of incidence of the ions, the impact of preferential damage has not been investigated systematically. However, typical sputter deposited $TiO_2$ films do not exhibit pronounced crystallographic texture. Hence, any effect that is based on the interaction between the ion beam and specifically oriented grains is not expected to depend on the angle of incidence. To identify a possible influence of chemical interaction we have used both oxygen ions and inert xenon ions in our experiments.

The ion-beam assisted setup which was described in section 4.2 has been utilized. Low total pressures of 0.3 to 0.4 Pa have been employed for film deposition to ensure appropriate conditions for the operation of the ion gun, producing of a large mean free path for the ions. Additionally, discharge currents of 1.2 to 1.6 Amperes were used to compensate for the slightly increased target to substrate distance of 80 mm necessary for the simultaneous bombardment. To investigate the influence of ion bombardment on film growth, deposition conditions were used that typically promote the formation of mixed anatase and rutile film structures in the as-deposited state. Additional ion bombardment was then applied and the change of film structure was investigated. Two reference samples produced without auxiliary bombardment were usually deposited at the beginning and at the end of each bombardment series, respectively, to confirm process stability.

Figure 5.3 shows grazing incidence XRD patterns of films grown with additional $O^+$ ion bombardment. For the bombarded films the ion energy was increased from 150 to 300 eV while the power of the microwave source of the ion gun was kept fixed. As a consequence, the current density of the ion beam also increased with ion energy from approximately 0.7 µA / $cm^2$ to about 2.3 µA / $cm^2$, as measured with a flat probe at the substrate position prior to deposition. These current densities correspond to relative arrival ratios of ions to $TiO_2$ molecules of about 1.1 % (0.7 µA / $cm^2$) to 3.7 % (2.3 µA / $cm^2$) as derived from the deposition rate of the films. It is evident that even at low arrival ratios and for ion energies that are small compared to the typical energies of negatively charged oxygen ions generated at the target surface (~ 400 - 500 V) there is a significant influence on the film structure upon the bombardment. Particularly striking is the selective deterioration of the anatase phase. While the rutile phase is almost unaffected by the additional ion bombardment, the anatase phase completely disappears from the spectra at high current densities and ion energies. This difference might be due to the higher density of the rutile phase, which leads to an increased stability against ion erosion.

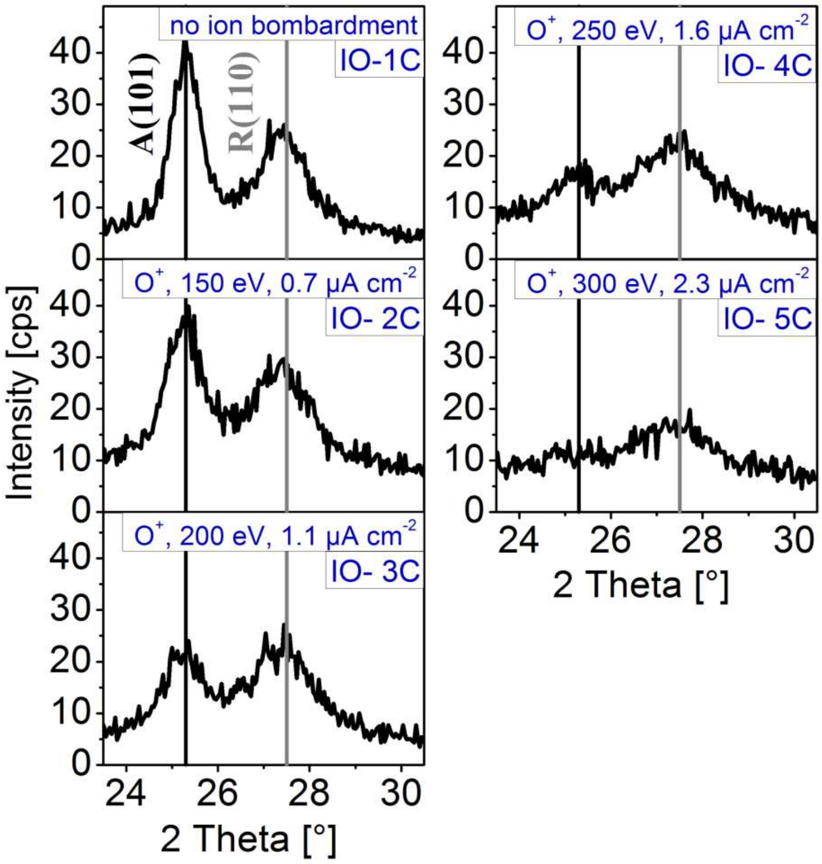

**Figure 5.3:** Grazing incidence XRD patterns of $TiO_2$ films sputtered under additional $O^+$ ion bombardment with different energies and intensities. The impact of energetic bombardment leads to a selective degradation of the anatase phase. However, at very intense bombardment also the rutile phase deteriorates.

The impact of oxygen ion bombardment also clearly manifests itself in changes of surface topography as shown for two films in figure 5.4. The un-bombarded reference film exhibits surface features with two different lateral length scales. To some extent it seems that the surface can be described by regularly arranged small-grained features constituting a background on which an open structure of rather irregular features with significantly larger mean widths has grown. Upon ion bombardment the large features completely vanish and the surface consists of the small-grained features alone. To simplify the discussion of AFM images we will henceforth refer to the regular small-grained surface structure, such as observed for sample IO-5C, as a *type 1 surface* while a *type 2 surface* denotes the irregular structural features observed for sample IO-1C. A very similar dependence of surface topography on phase composition of $TiO_2$ films has already frequently been reported in the literature [e.g. 21, 24, 28, 29, 31, 45, 127], where it is typically found that a type 1 surface is related to growth conditions that yield rutile films while anatase structures seem to exhibit a type 2 surface. It should be mentioned here that our investigations also revealed a correlation between surface topography and film thickness. However, since the crystal structure similarly depends on film thickness (see for example [21, 26]). Hence respective changes of the observed surface type coincided with the change of the crystal structure (rutile or anatase) present at the film surface.

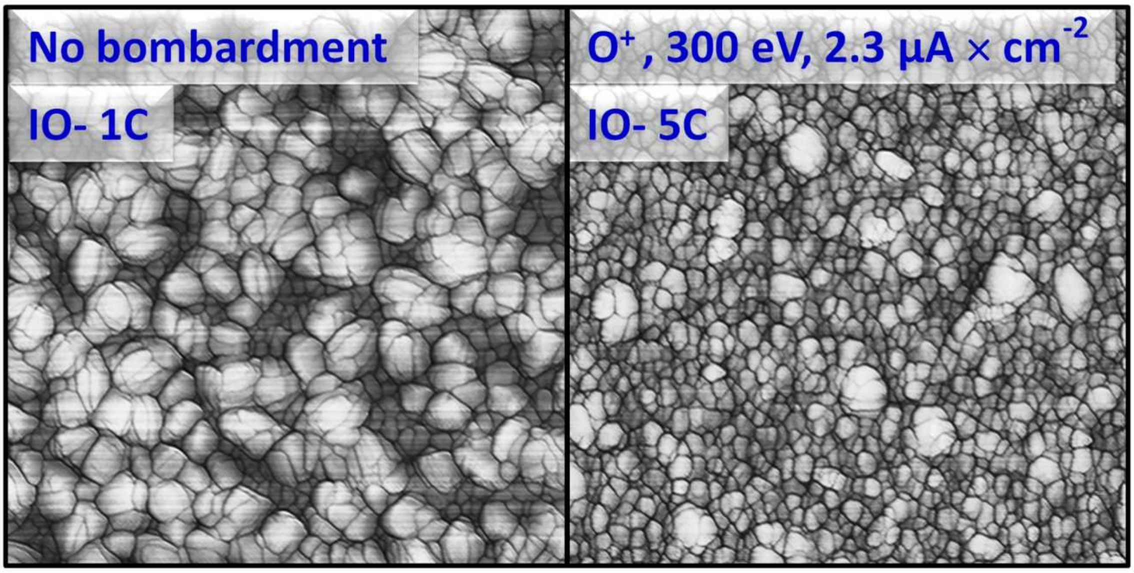

**Figure 5. 4:** Surface topography of a $TiO_2$ film bombarded with $O^+$ ions. XRD spectra of these films are shown in figure 5.3. The left image shows the un-bombarded reference which features a mixed type 1 and type 2 structure. The sample grown under intense ion bombardment is characterized by a pure type 1 surface structure. The scan size is 1 µm × 1 µm. Images are post-processed to enhance surface corrugation.

In [45] it was found for reactive ion beam mixing of $TiO_2$ that the crystal quality strongly depends on the ion species. To investigate possible differences between reactive and inert species in ion-assisted sputtering we have performed experiments also with an inert ion species. Therefore, xenon was used as the bombarding species. While the ion energy was kept fixed at 180 eV, the current density was increased from approximately 0.6 to 1.2 µA / $cm^2$, which corresponds to arrival ratios of 0.9 % and 1.8 %. Figure 5.5 shows grazing incidence XRD patterns from which it is evident that again a striking change in film structure occurs upon increasing intensity of the ion bombardment. It is especially noteworthy that at low current densities of 0.6 µA / cm$^2$ the formation of the rutile phase is noticeably promoted while the anatase phase generally deteriorates upon additional ion bombardment. The surface topography (fig. 5.6) also shows changes very similar to those found for the oxygen bombardment. A clear trend from a type 2 surface with very small type 1 contribution without ion bombardment towards a pronounced type 1 surface with increasing intensity of the ion bombardment is evident.

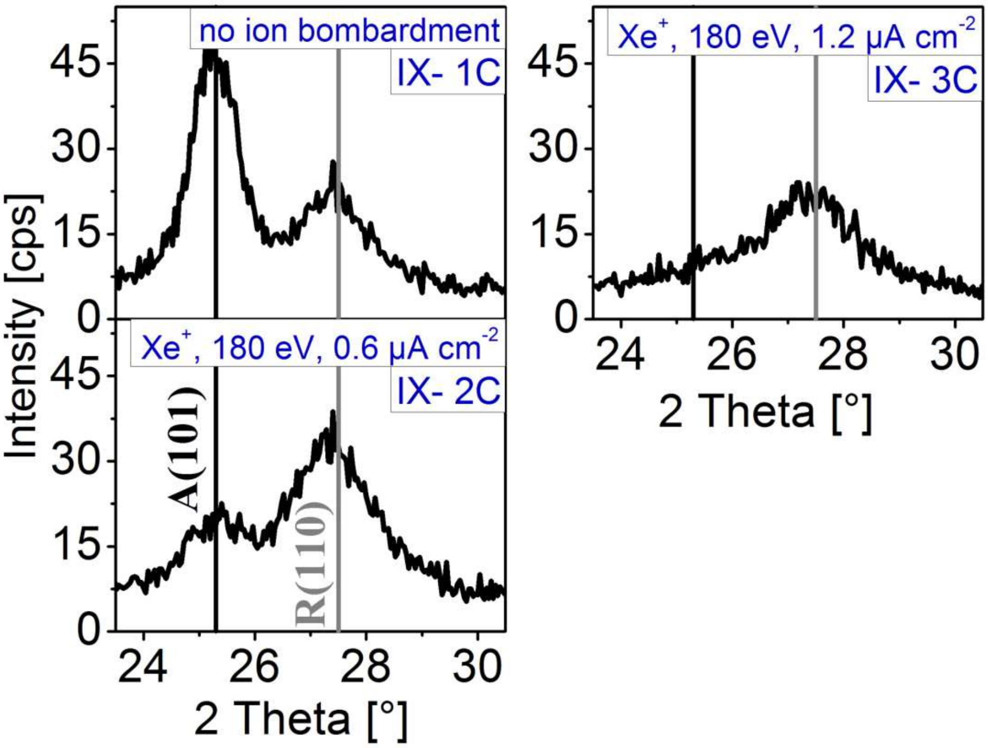

**Figure 5.5:** Grazing incidence XRD patterns of $TiO_2$ films sputtered under additional $Xe^+$ ion bombardment with two different intensities at a fixed ion energy of 180 eV. The impact of energetic bombardment leads to a selective degradation of the anatase phase. At small currents of the auxiliary $Xe^+$ ion bombardment the growth of the rutile phase is promoted by the bombardment.

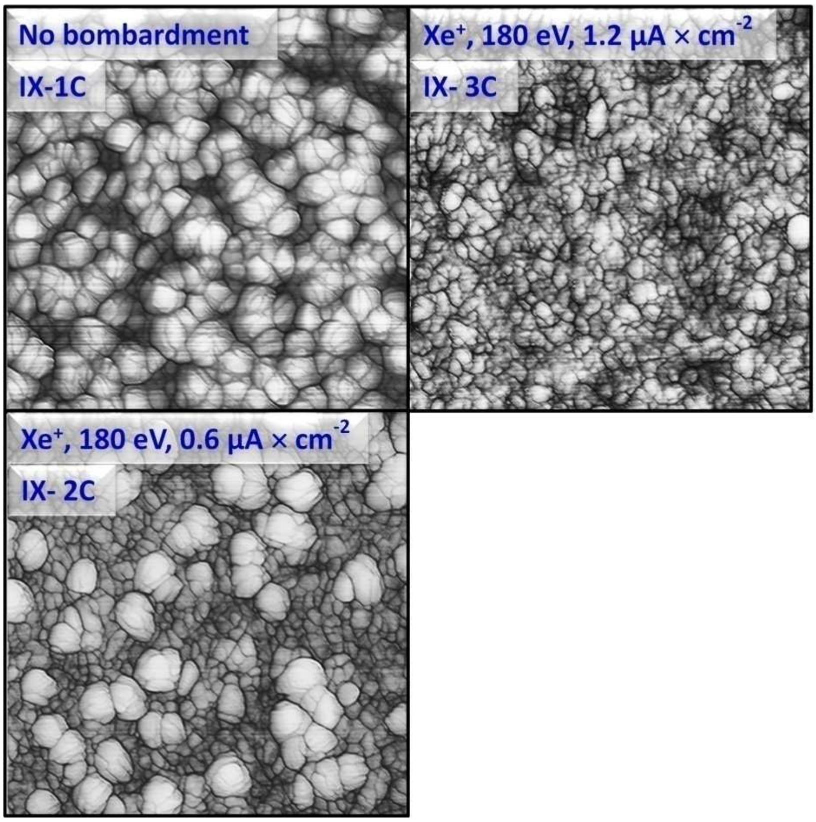

**Figure 5.6:** Surface topography of $TiO_2$ films bombarded with $Xe^+$ ions. XRD spectra of these films are shown in figure 5.5. The un-bombarded reference features a mixed type 1 and type 2 structure with strong tendency to a pure type 2 structure. Under medium intensity bombardment the type 2 content is significantly reduced while the sample grown under intense ion bombardment is characterized by a pure type 1 surface structure. The scan size is 1 µm × 1 µm. Images are post-processed to enhance surface corrugation**.**

From comparison of the results from oxygen and xenon ion bombardment we can conclude that the nature of the bombarding species (reactive or inert) does not play a major role in determining the film structure upon ion bombardment.

To summarize the results from experiments with controlled additional ion bombardment it can be stated that ion bombardment selectively hinders the formation of the anatase phase. At low intensity it was also found that growth of the rutile phase can be promoted by adequate ion bombardment. Furthermore, besides the XRD patterns, the resulting surface topography also clearly indicates the change in structure and hence the consequences of ion bombardment. These results are now applied to discuss the influence of the racetrack geometry of a reactively sputtered Ti-target (dcMS) on structure formation, since the racetrack of the target itself constitutes a source of highly energetic ions in reactive sputtering. Films will also be shown that have been deposited under conditions where this oxygen ion bombardment from the target surface has been reduced by geometrical means. Finally, structure formation of $TiO_2$ will be discussed for reactive HiPIMS discharges where a significantly stronger influence of ion bombardment is expected compared to dcMS.

### 5.3.2 Influenced by racetrack geometry

As discussed in section 5.2, during reactive deposition of $TiO_2$ negatively charged oxygen ions are created at the oxidized fraction of the target surface due to collisions with the sputtering species. These oxygen ions are accelerated and typically hit the growing film with a kinetic energy approximately equivalent to the full cathode voltage [48, 117, 125]. Since the extent of the cathode dark space is usually much smaller than the lateral scale of the target racetrack, the trajectories of the negatively charged oxygen ions strongly depend on the shape of the target surface [50]. Hence the distribution of oxygen ion bombardment along the substrate depends on the geometry of the deposition system but also on the age of the target. Therefore the films fabricated in our lab coaters are typically inhomogeneous in terms of the lateral distribution of oxygen ion bombardment and pronounced changes are observed upon aging of the target [50]. As sketched in figure 5.7, new targets without any pronounced erosion trace produce oxygen ion bombardment predominantly towards the edge of the substrate while the use of aged targets results in focusing the ion bombardment onto the centre. Films were deposited utilizing a new and an old Ti target respectively at a typical working pressure of 0.8 Pa at a discharge current of 0.9 and a target to substrate distance of 55 mm. The film properties were investigated at the centre and the edge of the substrates respectively. Regarding the influence of film thickness on crystal structure [cf e.g. 21] films have been deposited with different thicknesses for these investigations.

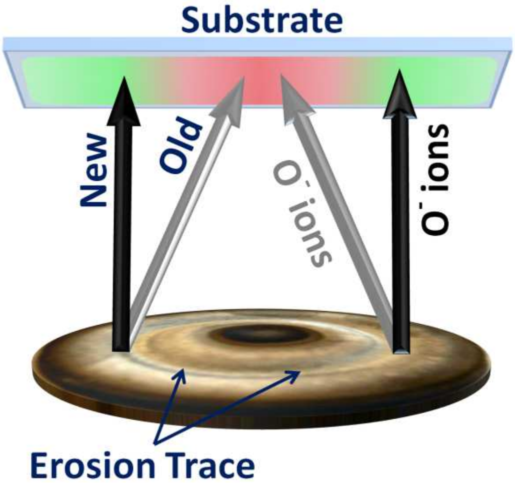

**Figure 5.7:** Influence of racetrack geometry on the ion trajectories for new and old targets. Oxygen ions that are created at the target are accelerated in a direction perpendicular to the local target surface area. For new targets the ions are accelerated towards substrate positions directly opposite the erosion trace. For aged targets the distribution of ion trajectories strongly depends on the shape of the erosion trace, which typically results in bombardment predominantly of the sample centre in the coating systems utilized for this work (cf [50]).

Figure 5.8 shows the XRD patterns recorded for films that have been deposited from a new target. AFM images for these films are presented in figure 5.9. There are a number of pronounced differences between film properties at the sample centre and at the edge. Starting with the crystal structure it is apparent that for all investigated films the rutile structure is more distinct at substrate positions above the racetrack of the target, even though films are thinner by about 10-15% at this position. Since a new target has been used, the area above the racetrack is subject to the most intense bombardment by negatively charged oxygen ions from the cathode as compared to other areas on the substrate. Qualitatively, this result is very similar to the structure formation under additional xenon ion bombardment at medium intensity (fig. 5.5). Hence, it seems that the formation of the rutile phase benefits from the bombardment. Regarding the anatase phase there is a small increase in intensity (except for the thinnest film) of the (101) peak at positions above the racetrack accompanied by an increase in peak width.

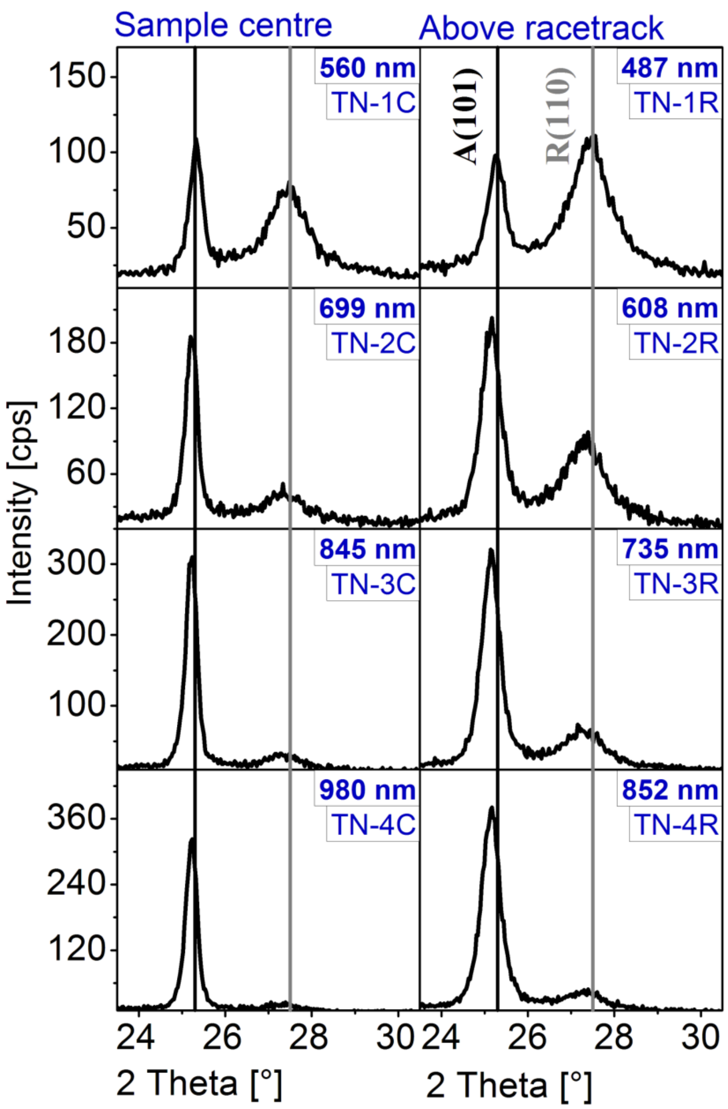

**Figure 5.8:** Grazing incidence XRD patterns of $TiO_2$ films deposited utilizing a new target. At positions above the target's racetrack the rutile phase is more dominant as compared to the sample centre. Also, the anatase peak shows a larger FWHM and a small shift towards lower angles compared to the centre, which is indicative of a smaller average grain size and increased compressive stress, respectively.

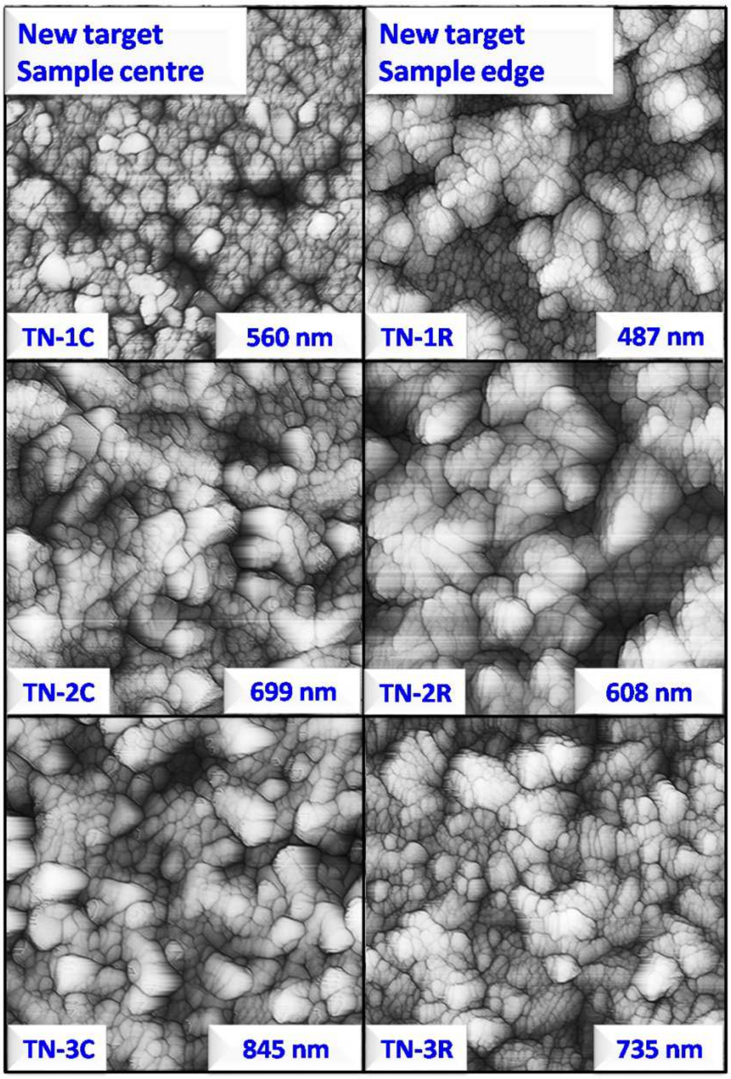

**Figure 5.9:** Surface topography of a $TiO_2$ film deposited using a new target. Above the target's racetrack (sample edge) the surface features a mixed type 1 and type 2 structure. At the sample centre a closed type 1 structure appears to dominate the surface. Corresponding XRD spectra of these samples are shown in figure 5.8. The scan size is 1 μm × 1 μm. Images are post-processed to enhance surface corrugation.

In conclusion, since the integral intensities of both the anatase (101) peak and the rutile (110) peak increase above the racetrack the films apparently exhibit better crystallization in this area. Additionally, in the same area the formation of the rutile phase seems to be favored with respect to the anatase phase. From the peak positions (literature values marked by vertical lines) it is evident that the crystal lattice is significantly strained in the bombarded regions (above the racetrack) of the substrate. The AFM images show that at the centre of the film there is a closed type 2 surface structure. At the edge, where negative oxygen ion bombardment is most intense, a type 1 surface topography can be clearly seen which is only partially covered by an open type 2 structure.

Investigating $TiO_2$ films sputtered from an aged target confirms our assumption that negative oxygen ion bombardment is the main reason for the structural inhomogeneities. Figures 5.10 and 5.11 clearly show that the pattern of typical fingerprints of oxygen ion bombardment has changed, which is in-line with the expected change in distribution of the ion bombardment due to altered target geometry (cf fig. 5.7). Now the sample centre shows an increased intensity of the rutile phase in combination with a larger width of the anatase (101) peak.

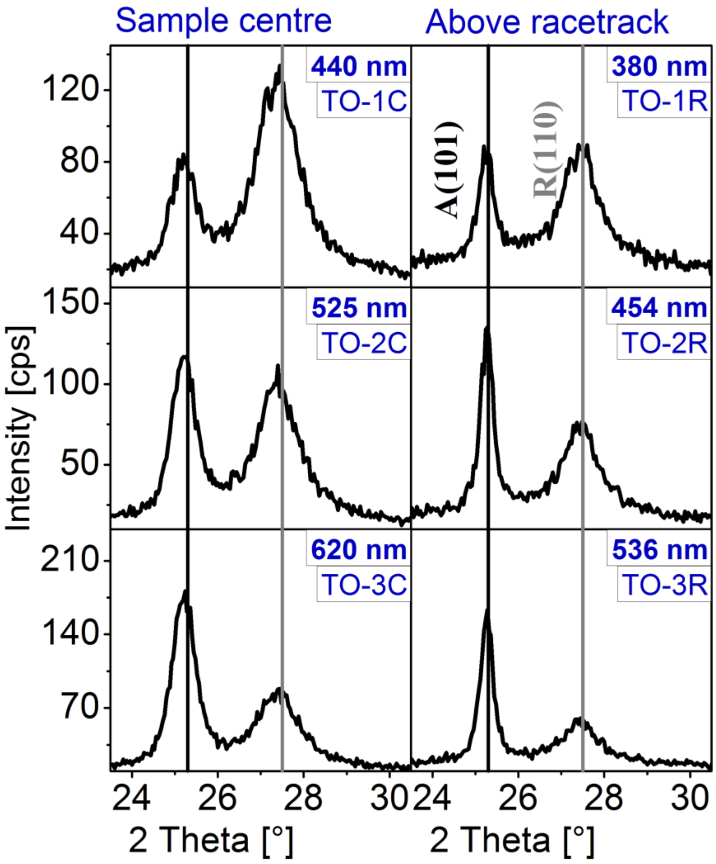

**Figure 5.10:** Grazing incidence XRD patterns of $TiO_2$ thin films deposited at intermediate oxygen flow from an old target. The samples were scanned at the sample centre and at positions directly above the target's racetrack, respectively. In the sample centre the rutile phase is more pronounced compared with the position above the racetrack. Also, the anatase peak shows a small shift towards lower angles at the centre position in comparison. The increasing width of the anatase peak indicates that the average anatase grain size is smaller at the substrate centre.

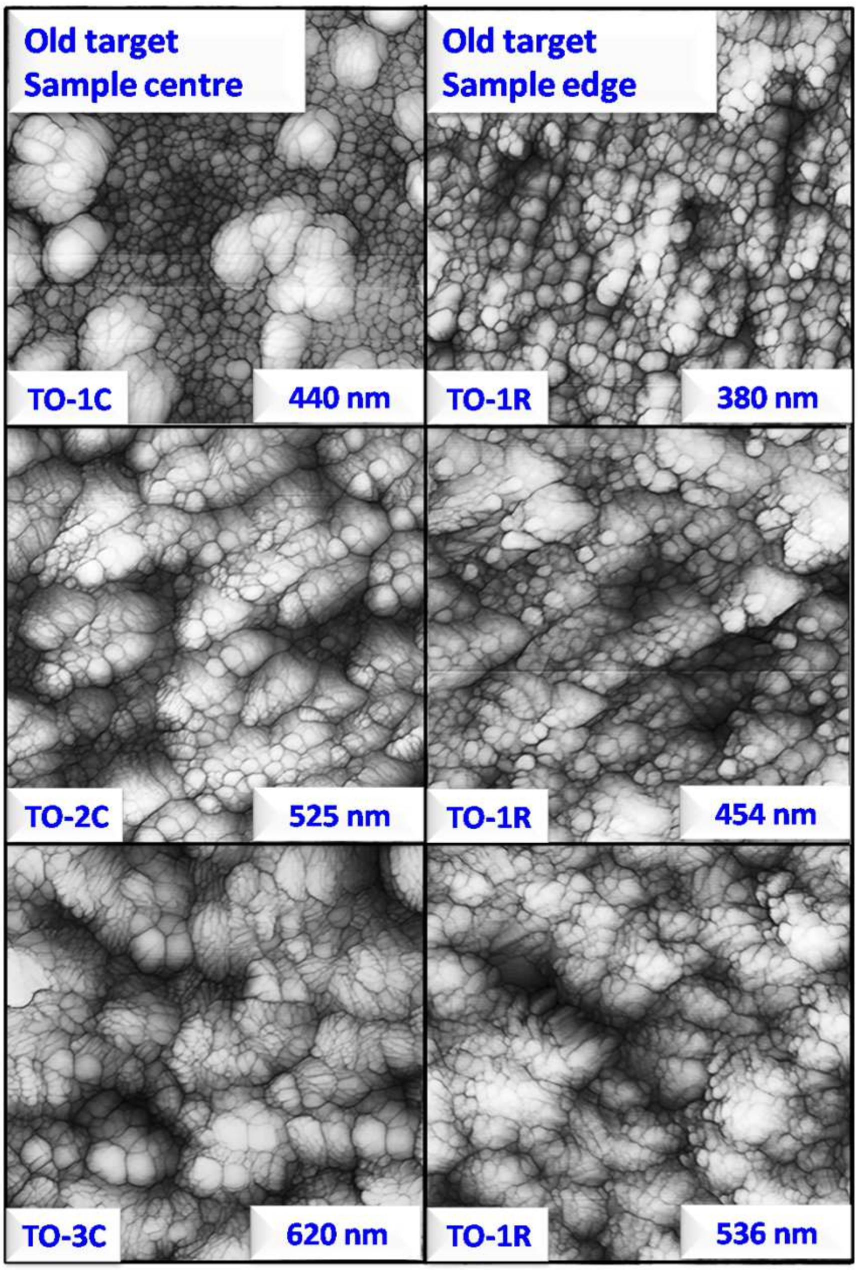

**Figure 5.11:** Surface topography of a $TiO_2$ film deposited from an old target. Above the racetrack, the surface exhibits a closed type 2 structure, while at the sample centre a mixed type 1 and type 2 structure is found. These findings correlate with the XRD spectra of these samples as shown in figure 5.10. The scan size is 1µm × 1µm. Images are post-processed to enhance surface corrugation

Film strain also is more pronounced at the sample centre in contrast to the films from the new target as shown in figure 5.12 where the peak positions of the anatase peak are shown.

We have used the Scherrer equation [104] to estimate the anatase grain size at the different substrate positions for the new and the old target, respectively.

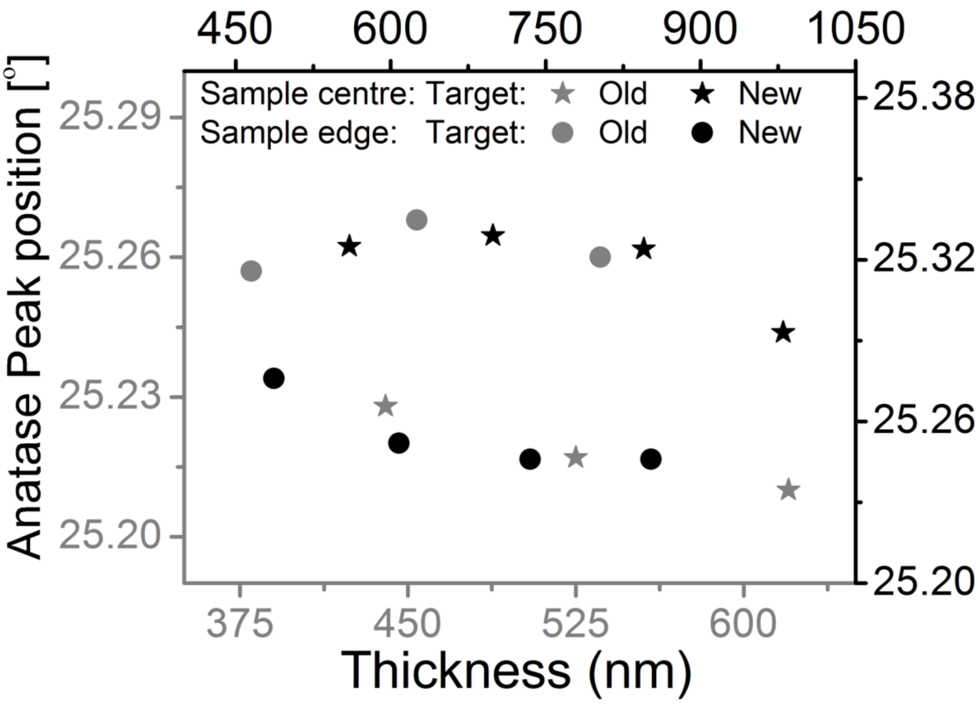

**Figure 5.12:** Position of the anatase (101) peak as extracted from the spectra shown in figures 5.8 and 5.10. There is evidence that at sample positions subject to increased energetic oxygen ion bombardment there is a shift of the anatase peak position towards lower angles. For the new target this is at the position opposite to the racetrack (sample edge) while for the old target this is at the sample centre. The shift of peak position indicates lattice strain and therefore mechanical film stresses induced by the impact of ions.

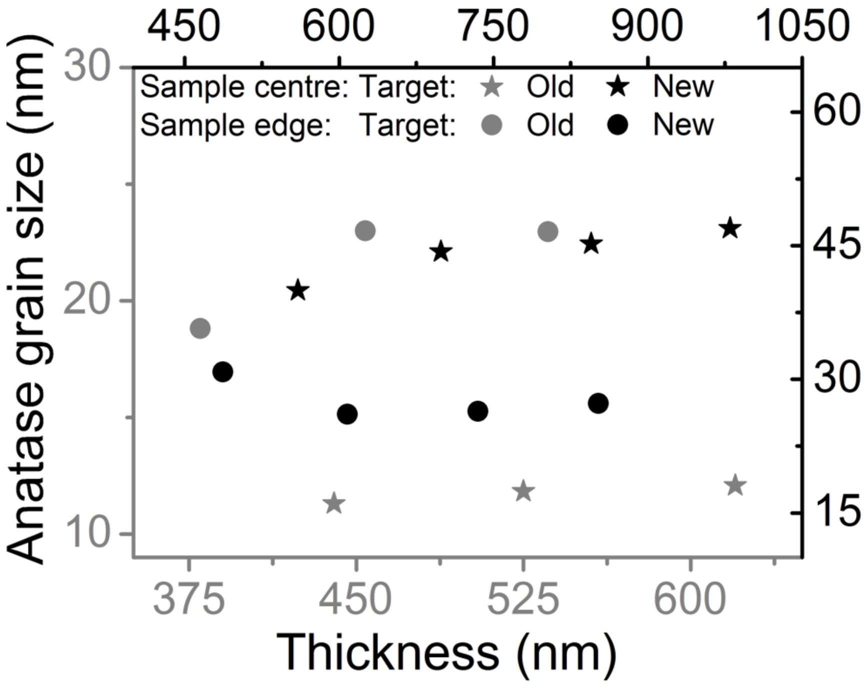

**Figure 5.13:** Estimation of the average grain sizes of the anatase phase for films sputtered from an old and a new target, respectively. The Scherrer formula has been applied to the anatase peaks in the diffraction patterns shown in figures 5.8 and 5.10. For the new target, the grain size is larger at the centre of the substrate while for the old targets the grain size is largest at a position at the sample edge (above the targets racetrack). This difference between the old and the new target is clear evidence for the effect of oxygen ion bombardment on structure evolution.

Figure 5.13 shows that the grain size is significantly affected by the oxygen ion bombardment. At positions with low bombardment the grain size is increased by a factor of approximately 2 with respect to positions that are hit predominantly by the energetic ions. In summary, these results provide unambiguous proof that highly energetic negatively charged oxygen ions created at the target surface and accelerated towards the growing film by the full cathode voltage strongly effect phase composition, strain (and thus film stress) as well as overall crystallization of reactively sputtered $TiO_2$ films.

### 5.3.3 Deposited by dcMS under reduced oxygen ion bombardment

To determine what would be the resulting film structure if oxygen ion bombardment was significantly reduced, an experiment was designed where the substrates were placed in vertical direction as shown in figure 5.14, such that the current density of energetic oxygen ions from the target surface was lower and ion impact proceeded at grazing incidence.

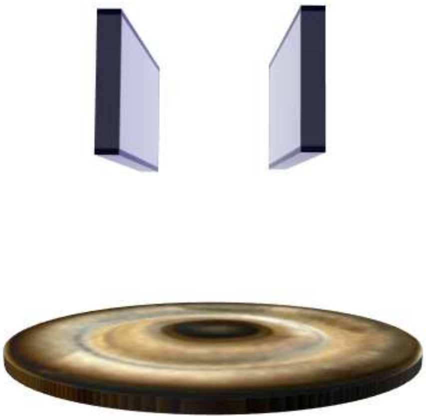

**Figure 5.14:** Sketch for the vertical substrate geometry. The substrates are placed in vertical position in order to reduce the bombardment by energetic oxygen ions from the target surface.

Corresponding XRD patterns are presented in figure 5.15, where the deposition geometry is also sketched as an inset. Sample S1 should be regarded as a reference sample here, since it was placed at the top of the “cavity” constructed by three substrates on a single carrier position. Because an aged target was utilized, sample S1 was therefore subject to oxygen ion bombardment from the target. There is no anatase peak in the diffraction pattern, but potentially a very weak rutile signal at $2\theta \approx 27.5°$. Sample S2 is one of the samples that were placed at the sides of the carrier. Because the film thickness of this sample is quite inhomogeneous, the sample was analyzed at its thickest position, which corresponds to a film thickness very comparable to that of sample S1. Sample S2 shows a pronounced anatase (101) peak. Sample S3 was deposited in an open cavity, i.e. without a top sample. Apparently the anatase signal from this sample is even stronger. We attribute the difference between samples S2 and S3 to recoil ions that are reflected at substrate S1 and probably increased ion bombardment of sample S2 in comparison to sample S3. The average grain size of sample S3 has been estimated to 22 nm (Scherrer).

To discuss the results from this experiment it should first be noted that all samples (S1-S3) produced are very thin (compare e.g. with the thicknesses of samples shown in figures 5.8

and 5.10). With regard to the pronounced influence of film thickness on crystal quality [21], which is also evident from figures 5.8 & 5.10, the very weak crystalline quality of sample S1 is typical for this film thickness. Therefore it is even more striking that both samples S2 and S3 exhibit a distinctly improved anatase structure without any rutile phase. Thus reducing the intensity of the energetic oxygen ion bombardment from the sputter target enables the fabrication of films with pure anatase structure.

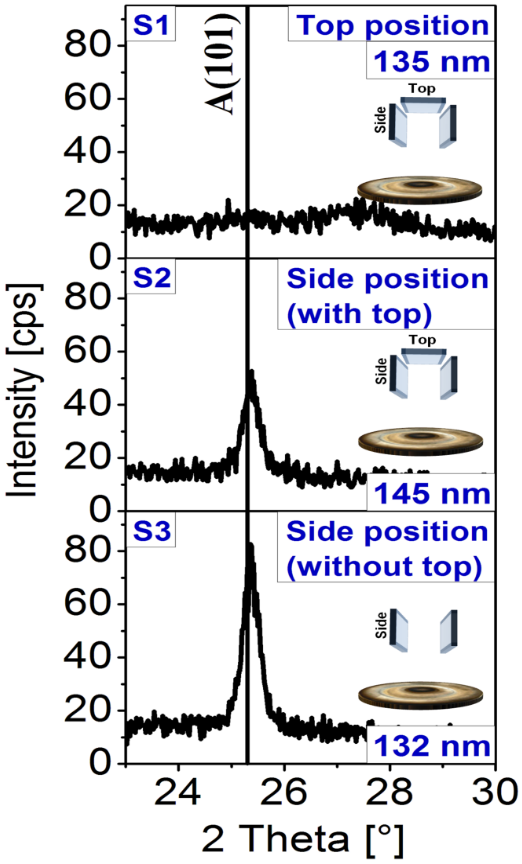

**Figure 5.15:** Grazing incidence XRD patterns of samples deposited with a special substrate geometry. To reduce the impact of energetic oxygen ions, samples have been arranged vertically at the edge of the substrate carrier. At one of the carrier positions an additional substrate (S1) had been placed at the top position. The structure of this sample is massively influenced by the oxygen ion impact and shows a very weak rutile structure probably, while sample S2 shows a distinct anatase structure as ion bombardment was of reduced intensity and occurred under grazing incidence. Probably sample S2 was hit by recoil ions from the top position (S1) because the structure of sample S3 which was sputtered with an open top position is of even better quality.

### 5.3.4 Structure evolution in a HiPIMS process

To characterize the structure formation of $TiO_2$ films in a HiPIMS process, films have been deposited at a constant average discharge current and by applying unipolar pulses with a length of 50 µs at a working pressure of 0.8 Pa. In this mode, the peak discharge current during a single pulse can be varied by changing the repetition frequency of the discharge, i.e. the length of the off-time between adjacent sputter pulses. With increasing off-time, the repetition frequency decreases and therefore the energy delivered to the sputter target during a single pulse has to increase to maintain a constant average discharge current. Hence, target voltage and, as a consequence, also the peak current increases. This behavior is depicted in figure 5.16, where the discharge voltage and peak current are plotted versus off-time. The data at zero off-time correspond to the properties of a DC discharge operated at the same average target current with the pulser operated in DC mode. Features of the HiPIMS discharge are an extremely high peak power density and a significantly increased target voltage compared to a dcMS discharge at the same average discharge current or power [115]. Consequently, the negatively charged oxygen ions that are created at the target surface and subsequently accelerated towards the growing film have much higher kinetic energies upon impact. Based on our previous investigations we therefore expect a significant increase in the influence of this ion bombardment. Additionally, there is a second effect that is expected to further increase the relative strength of the oxygen ion bombardment, which will be explained in the following. With increasing peak current density of the HiPIMS discharge, self-sputtering of the target becomes increasingly dominant since some of the sputtered species are ionized in the dense plasma and subsequently retracted towards the target surface. This significantly lowers the process efficiency, i.e. the ratio between the deposition rate and the sputtering power [79, 128]. This reduction of the deposition rate is evident from figure 5.16. Since the rate of generation of the negatively charged oxygen ions is not expected to be influenced to the same extent by the increasing action of self-sputtering due to the collision of the oxygen ions with the energetic sputtered Ti particles and an increase of the ionized sputtered species in the target's vicinity. This would imply an increased ratio of bombarding oxygen ions to deposited $TiO_2$ molecules at the substrate. Consequently, in a HiPIMS discharge the concurrent increase of the energy of the bombarding ions and the increase of the relative ion flux is expected to have a significant impact on structure formation.

A series of films was sputtered at an average target current of 0.9 A. The peak power was adjusted by increasing the off-time from 800 to 2000 µs for the different samples.

Accordingly, the frequency of the discharge decreased from approximately 1180 to 490 Hz while the peak power increased from about 32 to 114 kW.

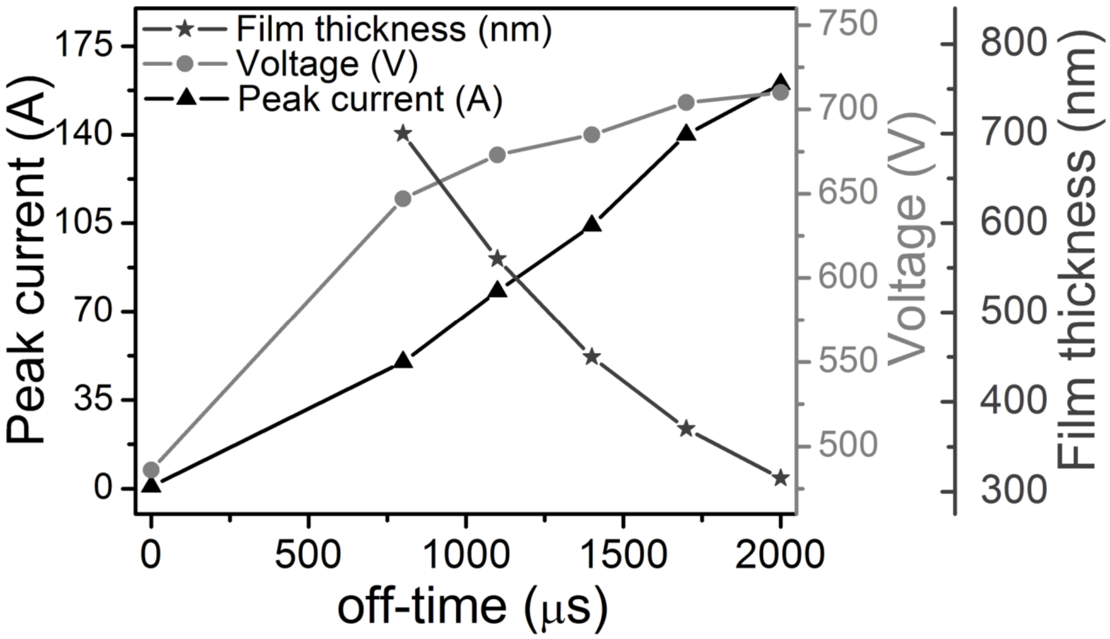

**Figure 5.16:** Process properties of $TiO_2$ films deposited by HiPIMS. With increasing off-time (i.e. decreasing pulse frequency) at constant average target current of 900 mA the peak current strongly increases up to 160 amperes for the largest off-time. At the same time the target voltage increases by about 50 V from approximately 650 to 700 V. The voltage in a dcMS process is only 500 V. The deposition rate strongly decreases with increasing peak power, due to the self-sputtering phenomenon, which is evident from the resulting film thicknesses. This is a typical feature of HiPIMS processes.

Figure 5.17 shows XRD patterns of the films fabricated. One of the spectra shows a sample (D1) sputtered in a dcMS process under otherwise identical conditions, which serves as a reference. XRD spectra were recorded at the sample centre and at the edge to also show the lateral in-homogeneities according to the directional oxygen ion bombardment from the target. From the reference it is evident that the utilized target exhibited only a shallow racetrack. This is evident e.g. from the intense rutile (110) peak at the substrate position opposite to the targets racetrack. From our previous investigations we know that this is an unambiguous fingerprint of intense oxygen ion bombardment from the cathode. Hence, for the HiPIMS films there are several clear trends:

i) At low peak currents of 50 Amperes (sample H1) the peak and integral intensities both of the anatase (101) and the rutile (110) peak are larger by a factor of 2 at the sample centre compared to the reference sample D1. There might be several reasons for that. First, a similar observation has been made when investigating the profiles of films sputtered from old or new targets, respectively (figures 5.8 & 5.10). There, an increase of the overall crystallinity of the films has been observed at substrate positions that were subject to an increased oxygen ion bombardment. Therefore, also for the HiPIMS samples energetic oxygen ion bombardment should yield an increase of crystalline phase. Second, since the average discharge power is increased by 33 - 46% for samples H1 - H5 compared to sample D1 due to the increase in discharge voltage, an increased transfer of thermal energy from the target and the plasma to the growing film occurs which could have a significant influence.

ii) Compared to the relative intensity of the anatase and rutile peaks of the reference D1, even at the lowest peak power (sample H1) there is already a more pronounced decrease in the anatase peak intensity at the edge of the sample as compared to the centre. Also, the improvement in the rutile (110) peak intensity at the edge of the sample (above the racetrack) is not as pronounced as for sample D1. We therefore conclude that the ion bombardment in the HiPIMS discharge is significantly stronger than in the DC discharge already at medium peak currents. This can be observed from the homogeneity of the film structure along the substrate profile due to an increase of the ion bombardment in the HiPIMS process as the peak power increases (samples H2-H3).

iii) With increasing peak power the selective deterioration of the anatase phase becomes more pronounced especially at the sample centre. Since the discharge voltage does not significantly increase upon increasing the peak current from 50 Amperes (sample H1) to 160 Amperes (sample H5) and based on our results from ion-assisted dcMS we can understand this trend as an increase of the relative arrival ratio of oxygen ions to $TiO_2$ molecules.

iv) With high peak powers the film structure tends to become almost homogeneous across the substrate and is very likely governed by massive energetic bombardment across the full width of the sample (H5). This fact can probably be attributed to the extension of the erosion area presumably due to a loss of magnetic confinement above the sputtered target at extreme power densities [129]. The lateral homogeneity of the ion bombardment at high peak powers (sample H5 and partially H4) is further supported by the fact that for peak currents larger than 104 Amperes the relative intensity of the rutile peaks at the centre and the edge of the samples has changed to an order that can be explained solely by the difference in film thickness between the different sample positions.

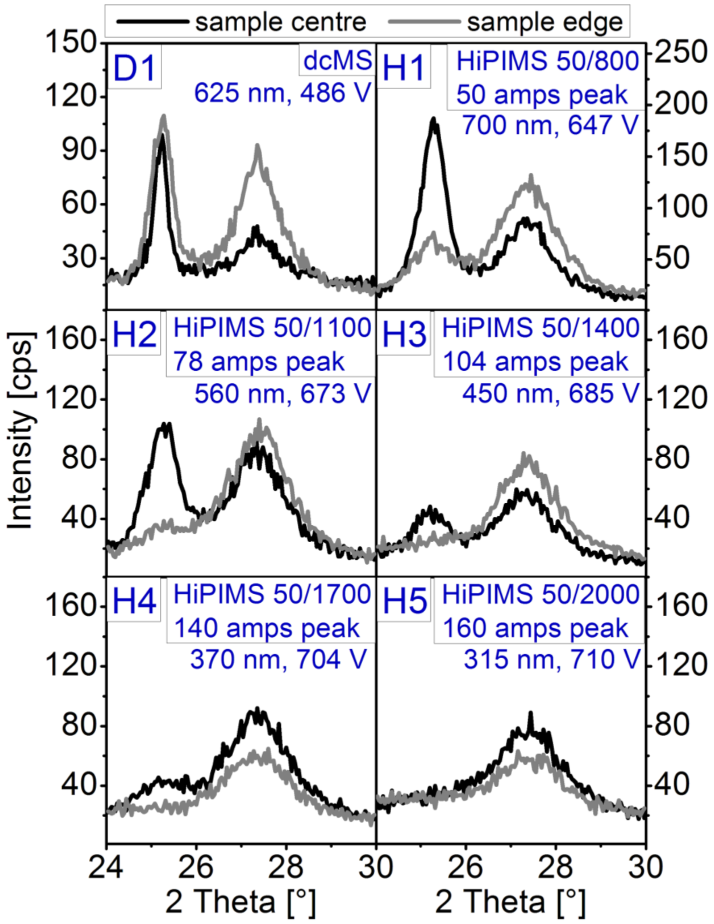

**Figure 5. 17:** Grazing incidence XRD patterns of films sputtered in a HiPIMS process. The length of the voltage pulses was fixed at 50 µs for each film while the pulsing frequency was varied by changing the delay between adjacent pulses from 800 to 2000 µs. The discharge current was fixed at 900 mA for all films. Low frequencies result in larger peak sputter currents and higher discharge voltages, as indicated. The deposition time for each film was 1 hour. The film thickness especially at large pulsing frequencies is slightly increased compared to the dcMS film (D1) which serves as a reference here. The increase of the deposition rate for high frequencies (H1) is a general feature of the HiPIMS discharge and is observed for other materials as well. With increasing peak current the anatase peak selectively deteriorates while the growth of the rutile structure is promoted. At highest peak currents (H5) the structure exhibits a homogeneous profile along the substrate since no difference between the sample centre and the edge is observed.

A statement should be given here about a possible influence of the film thickness on the results discussed above. Since film thickness decreases by about a factor of 2 upon increasing the peak discharge current from 50 to 160 Amperes, the thickness dependence has an influence on film structure as well. However, it has been confirmed that this effect does not alter the qualitative result by subsequent deposition of a sample with a thickness of approximately 300 nm at 50 Amperes peak. This sample showed a clear indication of the presence of the anatase phase (although the peak intensity is weaker than for sample H1) in contrast to sample H5 which is of similar thickness.

The change to homogeneous films with increasing power density is also reflected in the surface topography. The samples sputtered at 50, 78 and 160 Amperes peak were mapped by AFM. The corresponding images are presented in figure 5.18. The sample sputtered at 50 Amperes peak (H1) shows a mixed type 1 and 2 surface with extremely large connected regions of type 2 at the centre while towards the position above the racetrack a type 1 surface topography dominates. A similar observation was made for the sample sputtered at 78 Amperes peak (H2). However, there is a shift towards a predominant type 1 surface structure in direct comparison with sample H1. At highest power densities, type 2 surface features are completely absent (H5). The film sputtered at 160 Amperes peak is solely governed by type 1 surface features at all substrate positions. These observations are fully consistent with the correlations between ion bombardment, crystal structure and surface topography discussed for the IAS and dcMS processes in the foregoing sections.

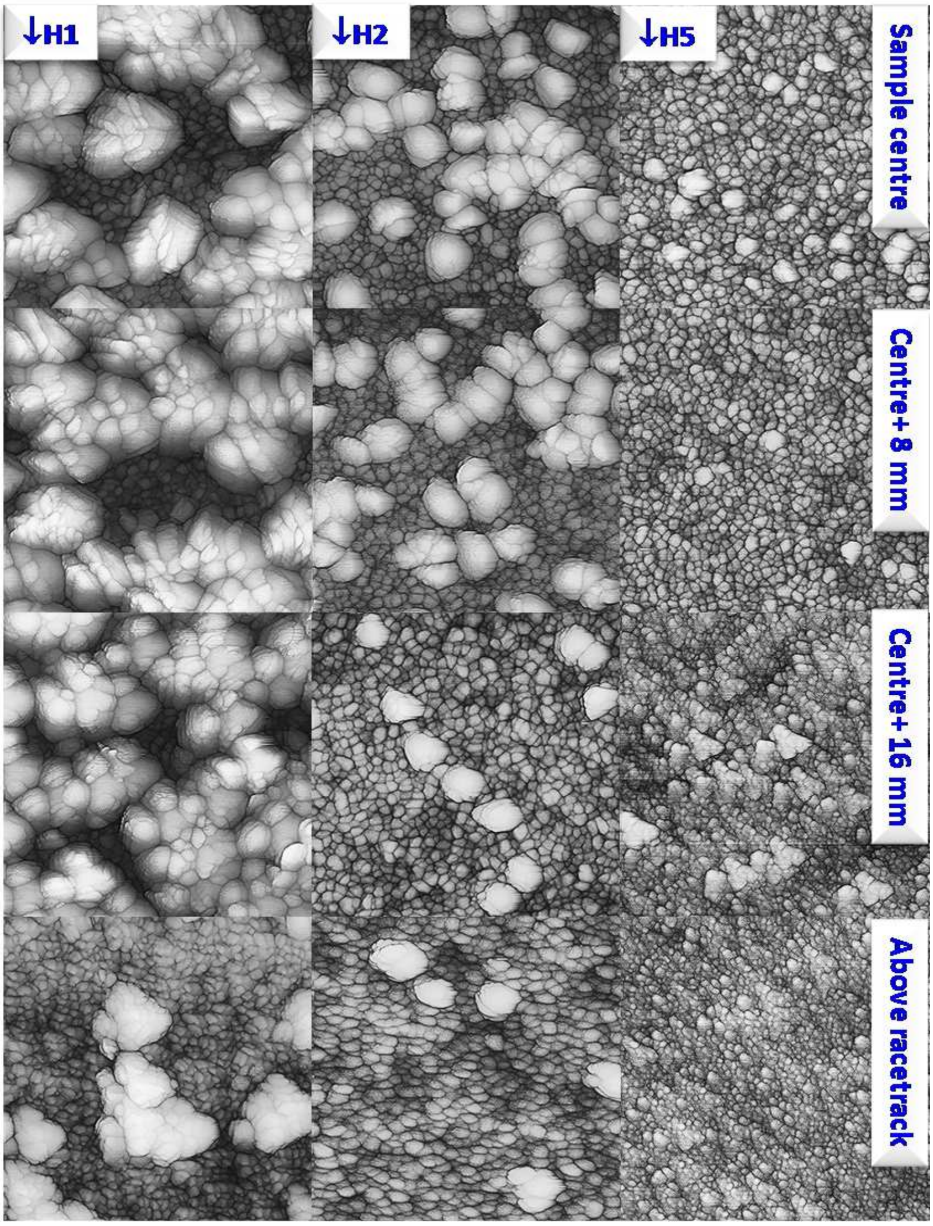

**Figure 5.18:** Surface topography profile of HiPIMS films (H1, H2, H5) sputtered at different pulse configurations. The samples are scanned in four steps from the sample centre to a position approximately above the racetrack. The geometrical distance between the scanned areas was 8 mm. The sample sputtered at 50 amps peak (H1) shows a distinct in-homogeneity along the substrate. In the sample centre a mixed type 1 and type 2 structure is found which is dominated by type 2. Above the racetrack a type 1 structure dominates. With increasing peak current (H1 → H2 → H5) a pure type 1 structure forms along the full extent of the substrate suggesting intense energetic bombardment at all substrate positions. Images are post-processed to enhance surface corrugation.

### 5.3.5 Thermal stability of films grown under intense ion bombardment

To further investigate structure formation upon energetic ion bombardment, $TiO_2$ films have also been treated in a post-deposition thermal annealing process. Five different samples have been selected: 1) A sample (T1) grown at low oxygen partial pressure which exhibited a very weak mixed anatase/rutile structure after deposition. 2) A sample with a pronounced mixed crystal structure deposited at an intermediate oxygen partial pressure (T2). 3) A sample exhibiting a pronounced anatase phase and a weak rutile contribution upon sputtering at a high partial pressure (T3). 4) A HiPIMS sample deposited at a large peak current (T4). 5) A rutile sample produced by ion-assisted reactive sputtering (T5).

It has been widely accepted in the literature that recrystallization upon post-deposition thermal annealing strongly depends on the microstructure of the sample [27, 37]. Typically films that are amorphous or mixed anatase/rutile exhibit pronounced anatase growth upon thermal annealing if the annealing temperature is well below the transition temperature of approximately 800 °C above which anatase $TiO_2$ is converted into a rutile structure. Only films with a pronounced anatase structure (as-deposited) are stable under post-deposition annealing below this temperature. Therefore, it is difficult to fabricate thermally stable rutile films by sputtering at moderate temperatures since at low temperatures rutile films can be deposited which are not thermally stable while at slightly higher substrate temperatures films typically grow with a preferred anatase structure.

The samples investigated have been annealed for 2 hours in air at a temperature of 270 °C. Some of the specimens have been further treated by an additional annealing process at 500 °C in vacuum for 2 hours. The results of these experiments are shown in figure 5.19.

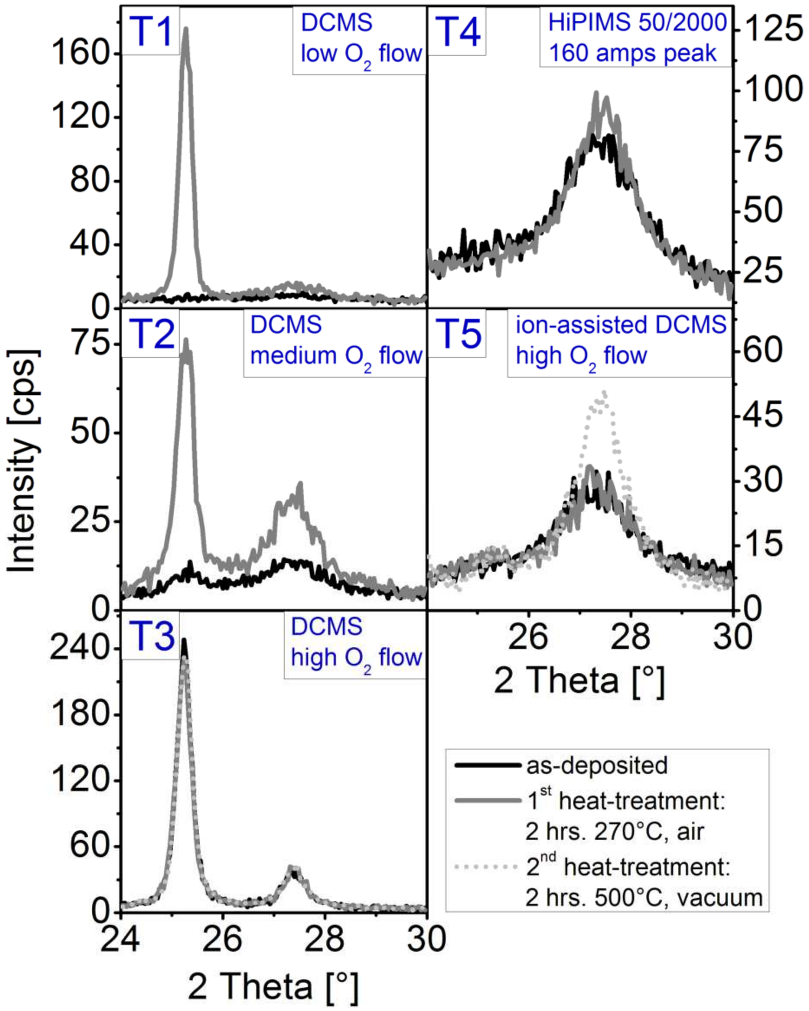

**Figure 5.19:** GI-XRD patterns of $TiO_2$ films treated by post-deposition thermal annealing steps. Sample T1 - T3 have been deposited in a standard dcMS process at different oxygen partial pressures. Low partial pressures yield an almost amorphous structure (T1), while with increasing partial pressure mixed rutile/anatase (T2) and finally strongly anatase films (T3) are fabricated. Samples T4 and T5 have been produced by HiPIMS and ion-assisted dcMS, respectively. Films have been annealed in air at 270 °C for 2 hours. Some films have been heated again at 500 °C for 2 hours in vacuum. For standard dcMS only the anatase sample (T3) is stable under the thermal treatment while both samples produced via ionized PVD (T4 and T5) exhibit a stable rutile phase.

It is evident that samples T1 - T3 exhibit exactly the behavior described above, i.e. it is not possible to fabricate a thermally stable rutile film. However, it is evident from the structure of samples T4 and T5 that have experienced sufficient high energy ion bombardment during deposition either by ion-assisted dcMS or HiPIMS yield rutile films that are comparatively stable. We propose that this behavior is a consequence of the microstructure of the as-deposited films. We assume that films grown under low ion bombardment and without a pronounced anatase phase contain a significant contribution of an amorphous phase which crystallizes into the anatase phase at temperature well below 800 °C for energetic reasons explained in [37]. Films grown under intense high energy ion bombardment on the contrary are assumed to have fully crystallized into the rutile phase during deposition and hence formation of an anatase phase is energetically not possible.

## 5.4 Mechanical growth stress

The mechanical stress in the deposited thin films can lead to severe problems including adhesion failures, formation of cracks and undesirable formation of holes. As the $TiO_2$ films are applied in applications where it is crucial to guarantee a certain lifetime, it is important to understand the origin of mechanical stress and control its level in the films. As mentioned in section 3.4, the generation of stress in the film is caused by the energetic bombardment of the growing film. Also, the $TiO_2$ films undergo a variation of the structure with the deposition parameters and the energetic bombardment. Hence, to investigate and understand the origin of deposition stresses in the films as a function of the structure and the various process parameters is the objective of this section.

The mechanical stress has been investigated by means of an in-situ wafer curvature method. The film stress and the instantaneous stress have been calculated from the film force and the deposition rate. The instantaneous stress represents the differential change in stress induced by each new deposited layer. Therefore it is sensitive to abrupt changes in the stress generating mechanisms. The instantaneous stress is defined by:

$$\sigma_i = d\,(\text{film force per unit length})\,[\text{Pam}] \;/\; d\,(\text{film thickness})\,[\text{m}] \qquad 5.1$$

As reported in the literature [20, 32, 130- 132], the $TiO_2$ films exhibit a compressive stress with a magnitude of the order of GPa which is dependent on the variation of the process parameters. Figure 5.20 shows the film stress of two crystalline $TiO_2$ films deposited at relatively low oxygen partial pressure of 8.5 sccm with different thicknesses and structures of rutile and mixed with small anatase contribution respectively. Both samples show the development of compressive stress on the order of -29 GPa, which is suddenly formed at the early stage of film formation and reaches a maximum at a few nanometers thickness. Then there is a slight decrease followed by a linear increase of the film stress during the continuous film growth. It seems that the structure variation has no significant influence on the film stress, whereas there is a slight decrease in the magnitude of the compressive stress for mixed structure. The generation of the compressive stress in the $TiO_2$ films has been attributed to the atomic peening mechanism [133, 134], i.e. the impact of high energy sputtered atoms to the growing film, as explained in section 3.4.1. The high magnitude of the compressive stress is attributed to increase of the kinetic energy of the sputtered particles. The particles impinging on the surface of the growing film can move to more energetically favored sites such as voids, interstitial positions and grain boundaries. The higher density of the film grown under these conditions will promote increase in the compressive stress.

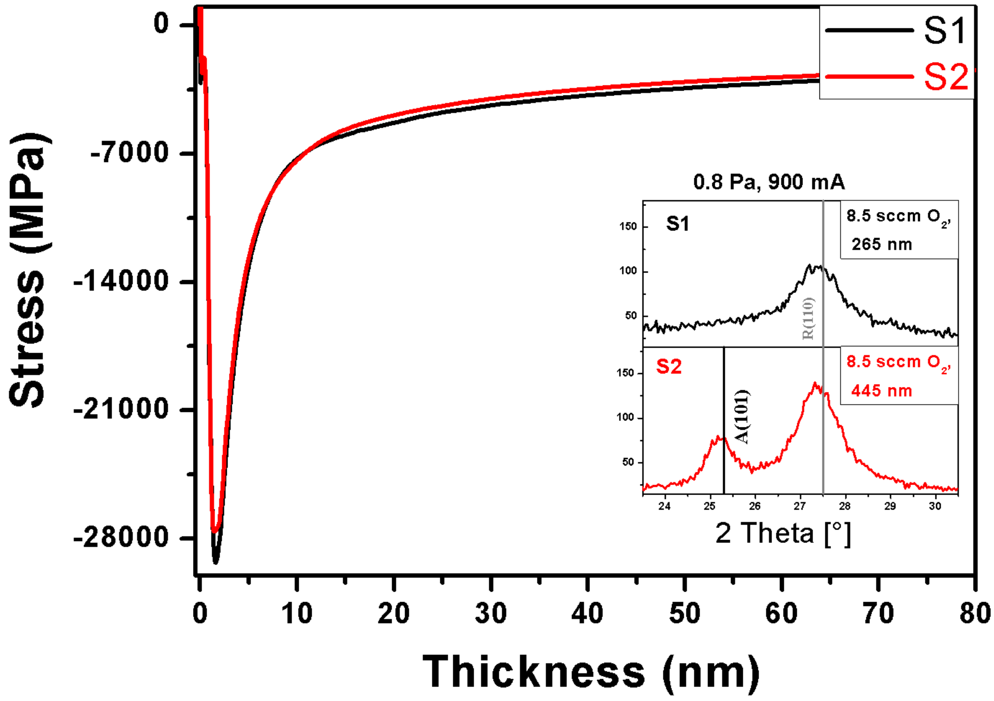

**Figure 5.20:** In-situ stress measurement of $TiO_2$ films sputtered at relatively low oxygen flow (8.5 sccm) with different thickness and structures. It is obvious that both samples exhibit generation of compressive stress during the early stage of the film formation followed by a slight decrease. Then there is a linear increase during the advance layer growth. There is no significant change in the magnitude or the behavior of the compressive stress upon structure variation.

### 5.4.1 Dependence of film stress on the oxygen content in the process

To further unravel the influence of the process parameters and the structure variation on the stress, the film stress has been investigated as a function of oxygen partial pressure. Figure 5.21 shows the film stress and the instantaneous stress of $TiO_2$ films fabricated at different oxygen flows. All films have been deposited at the same discharge current and total sputtering pressure. At high oxygen flows (12-16 sccm $O_2$); the films exhibit a rutile structure with approximately equal thickness of 122 nm. At an oxygen flow of 7.5 sccm, the film shows a mixed structure with 800 nm thickness due to deposition at high deposition time. However all films exhibit a compressive stress of the order of GPa. The level of the compressive stress increases with increasing oxygen partial pressure. The same trend has been observed in ZnO and $ZrO_2$ films by Drese et al. [126, 135]. They attributed this to increasing the bombardment of the growing film by the energetic oxygen ions. As the oxygen flow increases, the oxidation layer on the target surface increases where the energetic oxygen ions are formed. The instantaneous stress (the lower graph, figure 5.21) reveals that the generation of the compressive stress takes place at the early stage of the film growth. As the oxygen flow increases, the development of the compressive stress occurs at the first deposited layers with a high order of magnitude. This has been attributed to increasing the energy of the bombarded oxygen ions and the kinetic energy of the sputtered particles to the growing film by applying high oxygen content to the film.

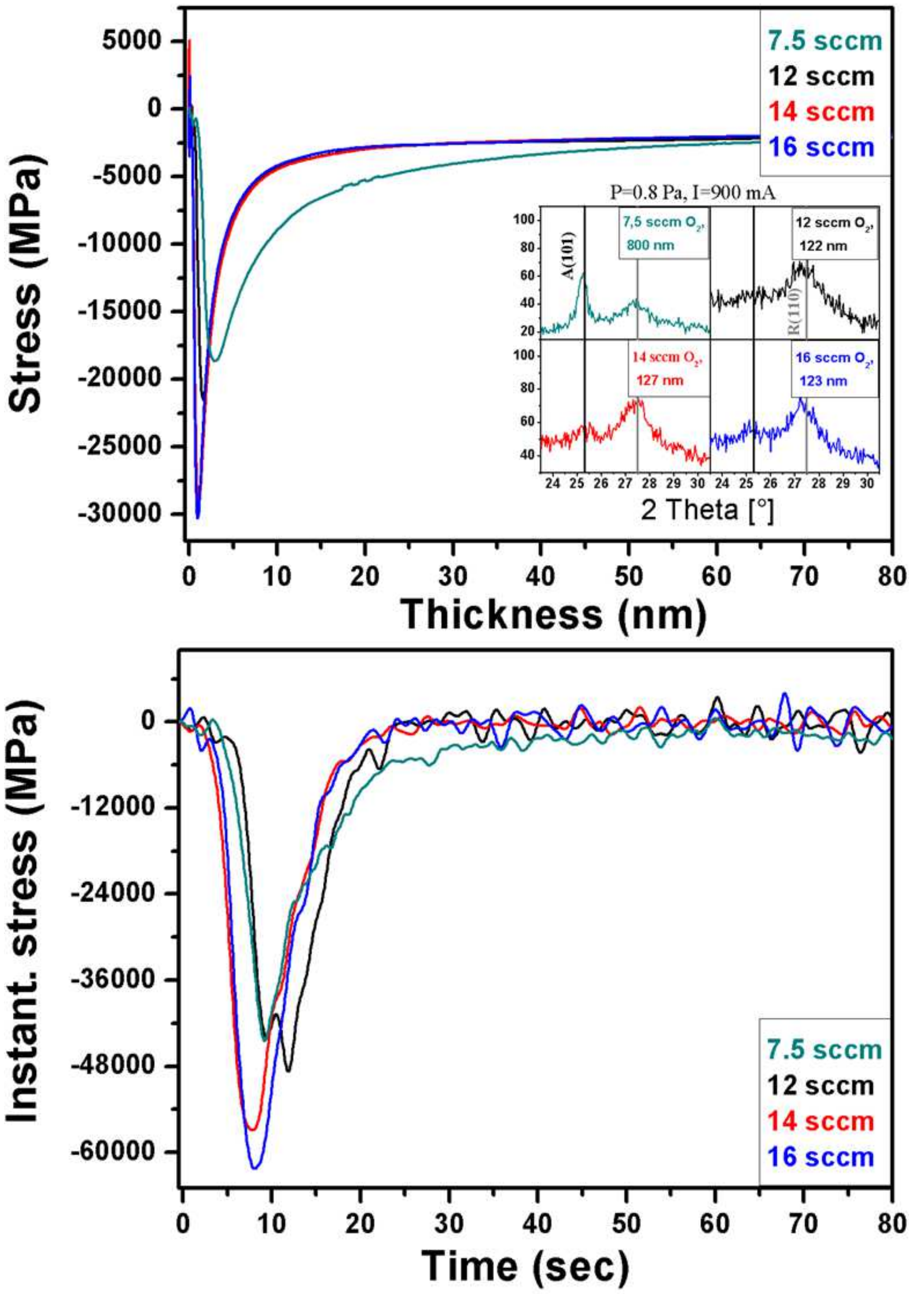

**Figure 5. 21:** Dependence of the film stress and the instantaneous stress on the oxygen content in the growing $TiO_2$ film. All films at high oxygen flows (12-16 sccm $O_2$) show a rutile structure while film sputtered at low oxygen flow with higher thickness show a mixed structure. The in-situ stress measurements of all $TiO_2$ films at different oxygen partial pressure reveal that increasing the oxygen content leads to the generation of a pronounced compressive stress in the film. The generation of the compressive stress starts at the first deposited layers with applying high oxygen flows to the growing film as observed from the instantaneous stress (lower graph).

### 5.4.2 Influence of sputtering pressure on the film stress

The mechanical stress has been further investigated upon a variation of the total sputtering pressure. Figure 5.22 presents the in-situ stress and the instantaneous stress measurements of $TiO_2$ films deposited at an oxygen partial pressure of 12 sccm and different working pressures in the range of 0.4 to 1.4 Pa. The films show either a rutile or amorphous structure. As usual all films exhibit a compressive stress. In contrast to the effect of the oxygen partial pressure, the compressive stress shows an opposite trend. The magnitude of the compressive stress decreases as the total sputtering pressure increases. This has been explained by a reduction of the energy of the bombarding oxygen ions upon increased collisions [135]. As the sputtering pressure increases, more collisions occur for the ions on their way to the substrate. This leads to more scattering of the ions, a reduction of kinetic energy and thereby a decrease in the compressive stress upon increasing the pressure. The instantaneous stress (equation 5.1) shows that higher sputtering pressures reduce the compressive stress in the $TiO_2$ films. As the total sputtering pressure increases, the deposition of new layers with a low kinetic energy has no much effect on the stress formation in the growing film. The dependence of the stress values at a film thickness of 15 nm upon sputtering pressure is presented in figure 5.23. It is obvious that the compressive stress changes dramatically upon increasing of the sputtering pressure.

### 5.4.3 Variation of the film stress with the discharge current

It has been found that by increasing the rf power, the compressive stress increased which is attributed to increase of the kinetic energy of the sputtered particles and the densification of the film [132]. Also a sharp increase of the compressive stress has been observed at high substrate bias correlated with the higher density of the film [130]. Hence, we have investigated the in-situ stress as a function of the discharge current. Figure 5.24 shows the film stress of $TiO_2$ films deposited at low oxygen partial pressure close to the transition point upon variation of the discharge current from 0.5 to 0.9 ampere and at constant sputtering pressure of 0.8 Pa. All films exhibit an amorphous structure. It is clearly visible that a high level of compressive stress on the order of -15 GPa is generated in the film upon applying a high current. On the other hand, a very low amount of compressive stress is formed at a very low target current. It has been found that the particles impinging on the surface of the growing film at high r.f. power leads to movement of the coating atoms to more energetically favoured sites such as voids and interstitial positions [132]. This causes the high densification of the growing film and generation of high compressive stress. Therefore we assume that increasing the target current leads to densification of the growing film and thereby generation of high values of compressive stress.

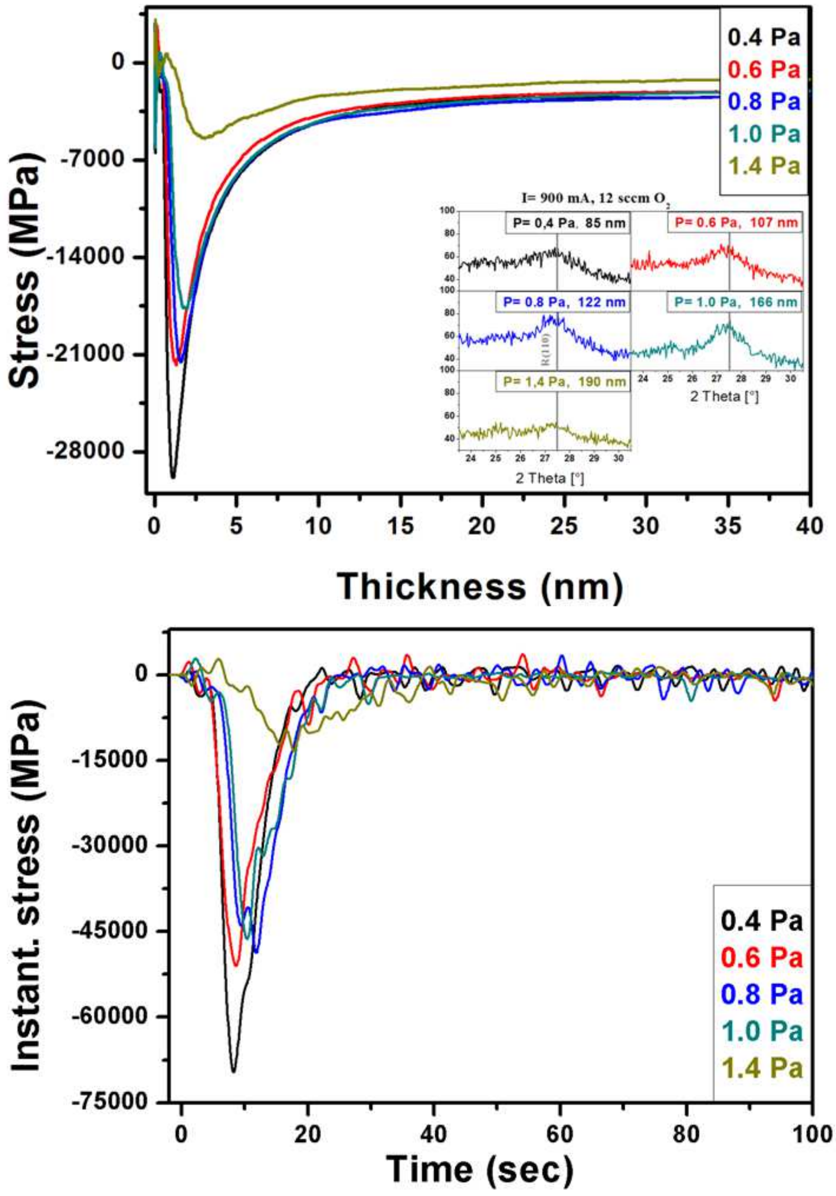

**Figure 5.22:** Variation of the film stress and the instantaneous stress as a function of the sputtering pressure of $TiO_2$ films. All films have been deposited at an oxygen flow of 12 sccm upon variation of the sputtering pressure from 0.4 to 1.4 Pa. Increasing the pressure and thereby decreasing the energy of the bombarded oxygen ions leads to reducing the magnitude of the compressive stress in the film. The instantaneous stress confirms this finding (the lower graph).

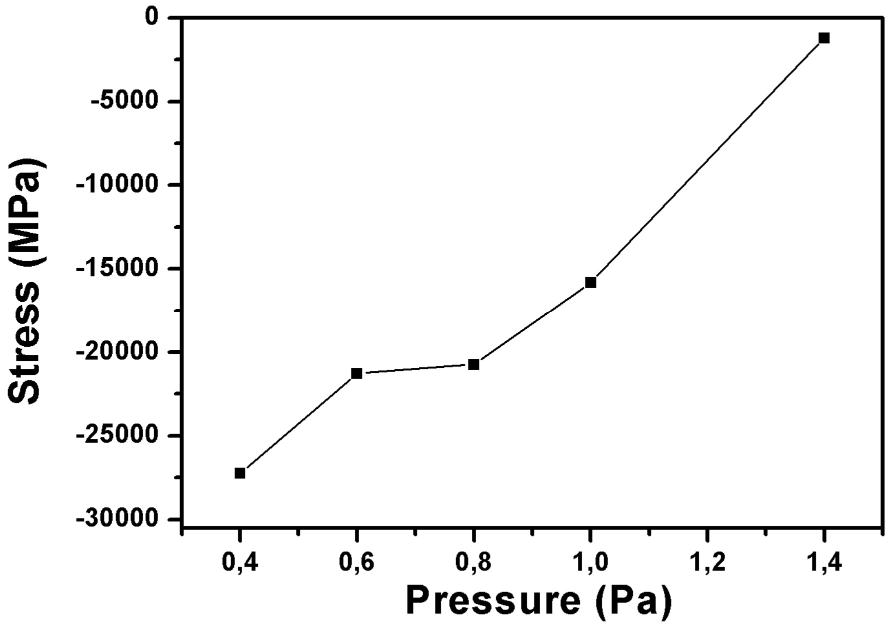

**Figure 5.23:** Variation of the compressive stress values at a film thickness of 15 nm as a function of increasing sputter pressure. The higher the deposition pressure, the lower the compressive stress values in the film.

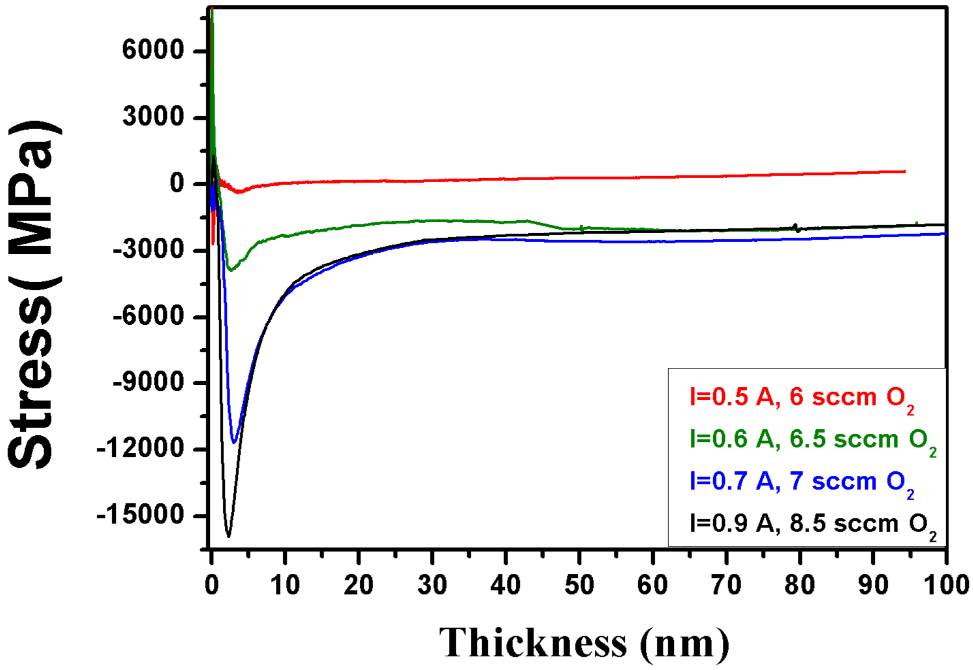

**Figure 5.24:** Influence of the discharge current on the film stress of $TiO_2$ thin films. Samples have been deposited at low oxygen flow close to the transition at different discharge currents in the range of 0.5 to 0.9 A at a constant sputtering pressure of 0.8 Pa. Decreasing the target current leads to a reduction of the compressive stress level in the film.

To summarize this section, the investigation of the mechanical stress of reactively sputtered $TiO_2$ thin films reveals a generation of compressive stress with a magnitude of several GPa. The compressive stress with high magnitude is suddenly formed at the early stage of film deposition. This is followed by a gradual decrease and then linear increase with film thickness which is explained by the atomic peening mechanism [133, 134] i.e. the impact of high energy sputtered atoms and energetic oxygen ions to the growing film. The high magnitude of the compressive stress is attributed to increase of the kinetic energy of the sputtered particles. The particles impinging on the surface of the growing film can move to more energetically favored sites such as voids, interstitial positions and grain boundaries. The higher density of the film grown under these conditions will promote increase in the compressive stress. It is also shown that the stress magnitude is strongly dependent on the process parameters instead of the film structure. Upon increasing the oxygen content and hence the bombardment by high energetic oxygen ions striking the film an increase of the compressive stress level is observed [126, 135]. The same behavior is observed as the discharge current increases. Also, compressive stress is observed in very dense films due to the increasing of momentum reaching the film and the increase of the adatom mobility [130, 134]. This is more evident from the variation of the stress with the sputtering pressure. At high sputtering pressure, more collisions occur for the ions on the way to the substrate thereby lowering the energetic ion bombardment the film [135]. This leads to a reduction of the compressive stress level in the film. The compressive stress is significant for thicker films due to the accumulation of defects and impurity incorporation during the growth [132]. It has been also observed that the compressive stress is relaxed during the continuous film growth; this might be explained by the thermal spike mechanism [100].

## 5.5. Discussion

The results from ion-assisted reactive sputtering and from the investigation of the lateral sample profiles for a standard dcMS process utilizing new and aged targets, respectively, provide unambiguous proof that highly energetic ion bombardment (especially negative oxygen ions generated at the target surface) need to be regarded probably as one of the most important quantities governing structure formation during reactive sputter deposition of $TiO_2$ films.

It has been found that the rutile phase of $TiO_2$ selectively grows with increasing energy/intensity of the bombardment. For the films sputtered by standard dcMS (figures 5.8 & 5.10) it has been found that the crystallization into the rutile phase is promoted by high energy oxygen ion bombardment inherent to the deposition technique. For films grown by ion-assisted sputtering an increase in the intensity of the rutile (110) peak has been found only at low ion current densities (sample IX-2C in figure 5.5) while higher current densities and energies already lead to a slight deterioration also of the rutile phase. For films deposited onto vertically aligned substrates (with respect to the target surface) films have been deposited without detectable traces of the rutile phase (samples S2 & S3 in figure 5.15). In conclusion, energetic bombardment is mandatory for the nucleation of the rutile phase. This can be explained by the fact that rutile is the high-energy phase (thermally stable phase at high temperature) of $TiO_2$, in contrast to the anatase phase and therefore requires a sufficient amount of energy to nucleate [cf e.g. 24, 35, 37, 41].

According to our investigations the anatase phase typically deteriorates upon an increase of high energy ion bombardment. This is likely a direct consequence of the fact that rutile nucleation is strongly promoted under such conditions. However, for several samples a selective deterioration of the anatase (101) peak has also been observed without a simultaneous increase of the rutile (110) peak intensity (compare e.g. samples IO-1C and IO-3C in figure 5.3). Therefore energetic ion bombardment might have an additional destructive influence on the crystallization or the growth of the anatase phase aside the promotion of rutile nucleation and growth. As yet, there is no clear proof for this assumption. Under conditions that result in relatively weak bombardment of the growing film (vertical substrates, figure 5.15) the growth of the anatase phase is strongly promoted. This behavior has frequently been observed in the literature and has been attributed to the fact that the amorphous phase has a density very similar to the density of anatase $TiO_2$ but significantly lower than the density of the rutile structure. Therefore, crystallization into the anatase phase is energetically favored at medium temperatures which do not yet promote nucleation of the rutile phase [37]. Anatase growth also profits from the fact that anatase grains seem to grow much faster than rutile grains under such conditions [37]. The difference in grain size of the anatase and the rutile crystals indicates a remarkable difference in the growth rate between both phases. The Anatase phase with large grains is growing fast whereas the rutile is growing very slowly at temperature below 600° C. This might be explained by the high surface free energy of the rutie phase than the anatase phase, as explained in chapter 8.

In many cases (see figures 5.8 & 5.10 for example) the bombardment by high energy oxygen ions does not only promote the growth of the rutile phase but also seems to improve the overall crystallinity of the films which is evident from the increase of the integral intensity of both the anatase (101) and the rutile (110) peak. An increase of the quality of anatase films for medium ion bombardment has also been found in the literature [32]. We attribute this to an increased nucleation density of the anatase phase, in particular. The density of the anatase phase (3.89 g $cm^{-3}$) is much lower than the density of the rutile phase (4.23 g $cm^{-3}$), so the anatase grains might be grown in a vertical direction over the rutile grains which leads to increase the crystallinity and overgrown the rutile by the anatase phase. Also the formation of rutile means a stronger densification and costs more energy than the formation of anatase [37].

Structure formation in a HiPIMS discharge is very similar to the ion-assisted sputtering process on the one hand and to the observations made upon investigating the influence of the target racetrack on the other hand. There is a very clear correlation of the structure with the trajectories of energetic negative oxygen ions. The structural changes are much more pronounced than in a DC process, which lead to the assumption of an increased bombardment intensity. Hence we think that this is a strong proof for the fact that also in a HiPIMS discharge negative oxygen ions with high energies are the dominant ion species that governs structure formation. We therefore propose that positively charged ions, in the absence of a large substrate bias potential, obtain comparatively low energies that have a much weaker influence on the crystallization of $TiO_2$.

In consequence the existence and where applicable the trajectories of the negatively charged oxygen ions emanating from the target surface need to be regarded as an important parameter in the discussion of the structural evolution of $TiO_2$ films.

In summary our experimental findings clearly show possibilities and limitations to tailor $TiO_2$ films for applications where the phase composition is an important parameter. We have demonstrated that a HiPIMS discharge apparently does not meet the prerequisites for fabricating films with anatase phase featuring large grain sizes. On the other hand, the growth of thermally stable films with pure rutile structure is strongly promoted in a HiPIMS process.

We also have shown that ion bombardment has a strong influence on surface topography. The observed surface features can be clearly distinguished. For a variety of films sputtered under different environmental conditions (oxygen partial pressure, and with different film thicknesses; as will be presented in chapter 6) we generally observe that rutile films exhibit a type 1 surface structure while the onset of anatase phase formation is typically accompanied by partial coverage of that surface by type 2 features. Films with preferentially anatase phase finally do not exhibit type 1 features at all. Hence, the explicit reduction of type 2 surface features in favor of the remaining type 1 surface upon ion bombardment is also a clear indication of the promotion of the rutile structure and the accompanying deterioration of the anatase phase. Due to this inter-correlation between crystal structure and surface topography of as-deposited films ion bombardment typically affects both crystallinity and topography.

It has also been found that the energetic bombardment causes the generation of compressive stress on the order of several GPa during the first stage of film growth. This has been explained by the atomic peening mechanism [133, 134]. We have observed that the film stress shows a significant variation upon changing deposition parameters such as oxygen partial pressure, total sputtering pressure and discharge current. This is explained by the change of the energetic oxygen ions striking the film as the parameters change.

## 5.6. Conclusion

There is clear evidence that, besides the directly accessible deposition conditions, ion bombardment plays a dominant role in structure formation. There is also unambiguous proof for the fact that it is the bombardment of the growing films by highly energetic oxygen ions inherent to the sputtering process that dominates structure formation rather than the bombardment by low energy positive ions from the plasma. Energetic bombardment strongly promotes the growth of the rutile films while anatase films typically profit from growth conditions that are characterized by the absence of (or very weak) ion bombardment. Purely rutile films can be grown under intense ion bombardment. In contrast to weakly anatase mixed films grown under low energetic ion bombardment, such films are thermally very stable since complete crystallization into the rutile phase is promoted by the intense bombardment during deposition and hence conversion into an anatase phase is energetically unfavorable. This knowledge further contributes to a comprehensive understanding of the correlation between film structure and process parameters and therefore constitutes another important step towards tailoring the structure and morphology of $TiO_2$ films.

# 6

# Structure zone model for the growth of reactively sputtered $TiO_2$ thin films

## 6.1 Introduction

As shown in chapter 5 the energetic oxygen ions have a significant effect on the structure formation of thin $TiO_2$ films. It has been proven that the growth of rutile films is favored at strong energetic bombardment while anatase films typically profit from the absence of (or very weak) ion bombardment. As presented in section 2.2, a large number of studies have been performed on $TiO_2$ thin films at different deposition parameters such as oxygen partial pressure and film thickness. It is reported in [21, 24, 41] that the structure formation of $TiO_2$ thin films depends strongly on the oxygen content in the process. The crystallinity of anatase phase is favored at high oxygen partial pressure ($P_{O2}$), while rutile is the dominatant phase at lower values of ($P_{O2}$). It was also reported in [21, 23, 25, 26] that the structure shows a transformation from rutile at low deposition time to anatase upon increasing the thickness of the deposited film. However, no significant attention has been given to investigate the surface topography and the film microstructure as a function of the oxygen content or film thickness. Moreover, the formation mechanism of the film structure is still discussed controversially. Therefore, it is our goal to figure out the mechanism of the structure evolution of sputtered $TiO_2$ thin films and establish a model to describe the structure variation as a function of the various process parameters.

To achieve this goal, we have been concerned with the investigation of the crystal structure as well as the surface structure of reactively sputtered $TiO_2$ thin films upon the variation of these deposition parameters (oxygen content and film thickness). More analysis of the film structure has also been done by the small angle rocking curve scan of the thickness films series, due to the observed change of the crystalline structure from rutile to anatase with increasing film thickness. Additionally, an investigation of the microstructure have been performed by TEM measurements on selected films with different thickness to further unravel the change in the film growth upon variation of the film thickness. The influence of the heating parameter during growth has also been investigated. At the end, a structure zone model has been developed to describe the correlation between the structure variation of $TiO_2$ thin films and the process parameters. The investigations and the results obtained are presented in this chapter.

## 6.2 Influence of oxygen partial pressure on the structure

In order to reveal the role of the oxygen partial pressure on the structure of $TiO_2$ thin films, a series of samples were fabricated at different oxygen flow rates ranging from 7.5 to 20 sccm with approximately equal thickness of 220 nm. The deposition was carried out in dcMS mode at a discharge current of 0.9 A. The oxygen/argon ratio was varied to keep the total sputtering pressure constant at 0.8 Pa. The sputtering was started again after 3 hr pre-sputtering in the oxide mode to ensure temperature stability during deposition and avoid any influence of temperature variations on the sample structure. The films display a significant variation from a pure rutile to a mixed structure upon increasing the oxygen flow as shown in figure 6.1. Further increment of the oxygen flow has no much effect on the structure i.e. no transition to the pure anatase phase has been observed. The grazing incidence XRD patterns show that the rutile phase (110) dominates for low oxygen partial pressure samples (O1, 7.5 sccm -O2, 8.5 sccm). The anatase phase (110) benefits from increasing the oxygen flow and starts to contribute to the film structure. Therefore, the resulting samples (O3, 11 sccm - O5, 12 sccm) show a mixed structure of rutile and anatase. Further increasing the oxygen flow leads to an increase of the anatase peak intensity. At higher oxygen flow, the anatase phase approximately dominates the film structure as shown in samples (O7, 17 sccm- O8, 20 sccm). These results indicate that the formation of the anatase phase is favored at high oxygen flow on unheated substrate $T_{sur} \leq 170°C$, which is consistent with [21, 24, 41].

The evaluation of the film structure upon increasing the oxygen partial pressure is also evident from the surface topography. AFM images display the influence of the oxygen flow on the surface structure as shown in figure 6.2. The surface structure exhibits two different features with different sizes, for example sample O4. To simplify the discussion of AFM images we will refer to the regular small-grained surface structure (sample O1) as a type 1 while a type 2 surface denotes the large irregular features which are observed for sample O8, as discussed in chapter 5. As reported in the literature [21, 31, 45] the type 1 surface is linked with a rutile phase while the anatase phase is accompanied by type 2 features. At low oxygen flow (samples O1-O2), the surface is characterized by the small-grained features (type 1). Upon increase the oxygen flow (sample O3-O4), irregular features (type 2) with larger mean width than type 1 started to form at separate sites, while the major fraction of the surface is still governed by type1. Further increasing of the flow leads to enlarging type 2 features as apparent in samples (O5-O6). Then it continues to overgrow until the films show completely ordered and smooth surface structure with type 2 features at high oxygen flows (O7- O8).

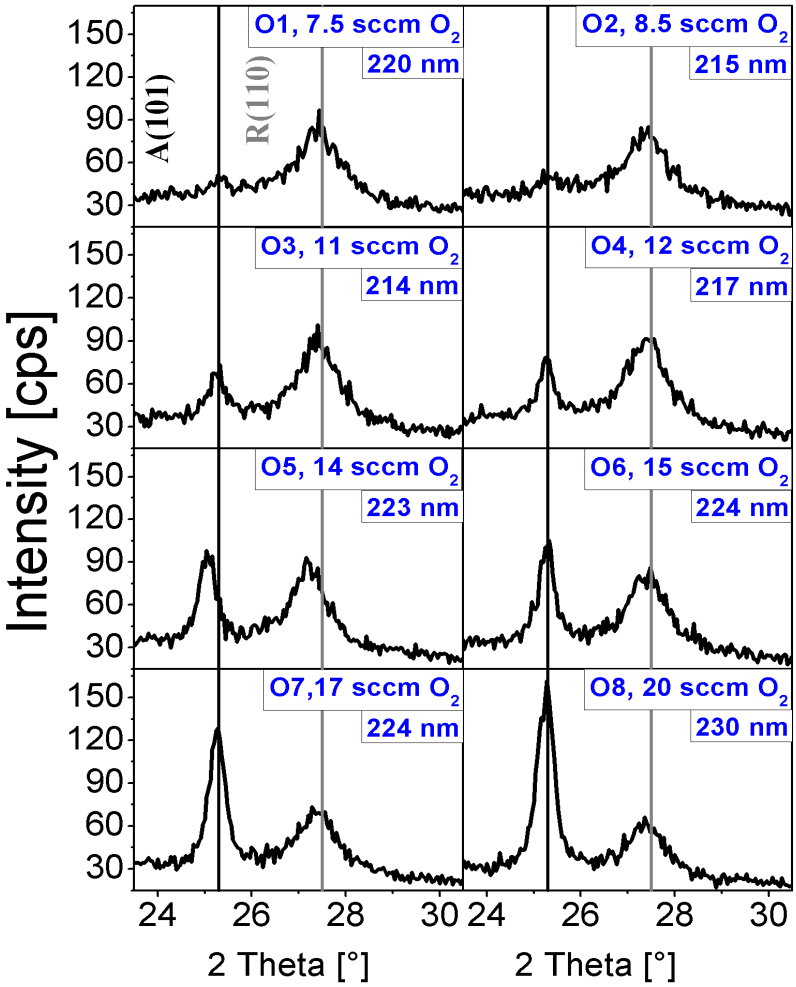

**Figure 6.1:** Grazing incidence XRD patterns of $TiO_2$ thin films deposited at different oxygen partial pressures. The scans were performed at an incidence angle of 0.7°. At low oxygen flow, the films exhibit a rutile structure (samples O1-O2). Upon increasing the flow, a mixed structure of anatase and rutile formed (samples O3-O5). At higher oxygen flow, the contribution of anatase phase increased and dominated the structure (samples O7-O8).

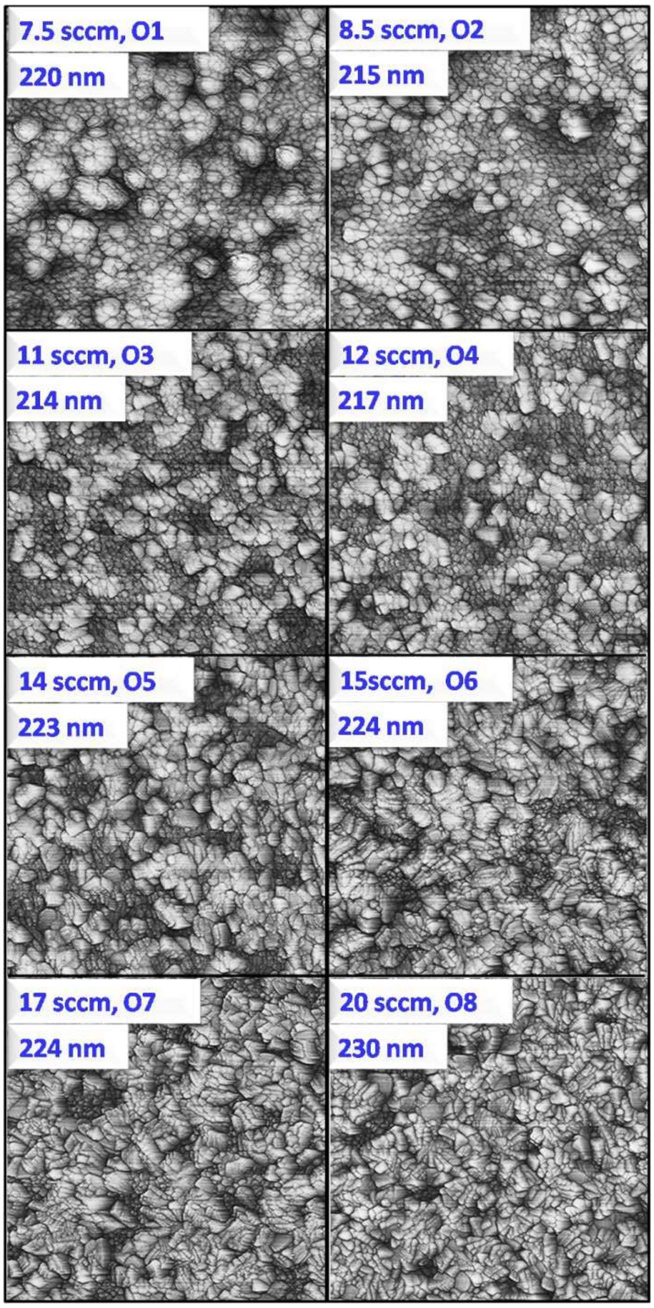

**Figure 6.2:** Surface topography of $TiO_2$ films deposited at different oxygen partial pressures. XRD spectra of these films are shown in figure 6.1. At low oxygen, the film exhibits a fine-grained surface (type 1, samples O1-O2). With increasing the flow, irregular features (type 2) with large size form at separated sites, while the major fraction of the surface is still governed by type1 (samples O3-O4). At larger oxygen flows, type 2 features have apparently overgrown the smaller features (O7-O8). The scansize is 1 × 1 $\mu m^2$. Images are post-processed to enhance surface corrugation.

In summary, these results show that presence of large amounts of oxygen in the process promotes the formation of the anatase phase, while the rutile phase dominates the structure at low oxygen partial pressure. Several explanations have been derived to understand this behavior. Löbl et al. [37] have reported that the formation of the rutile phase is favored when Ti atoms are the dominant vapour species, while the nucleation of anatase is favored by the presence of TiO and $TiO_2$. Additionally, Okimura et al. [136] have attributed the growth of the rutile phase to the higher irradiation of $Ar^+$ through the formation of O vacancies by sputtering at low pressure. They [137] also reported that the rutile phase is formed by the reaction of $Ti^+$ with $O_2^+$ and the concentration of $O_2^+$ is much higher at low pressures when high-energy electrons produce $O_2^+$ ions via inelastic collisions. Moreover, Suhail et al. [5] attributed the phase conversion to the energy of the incident particles since they observed an increase in the cathode potential for higher oxygen partial pressures and thereby decrease in the deposition rate. The reduction in the deposition rate has been attributed to the oxidation of the target and negative ion formation effects. Hence, we can conclude that the growth of rutile at low partial pressure is controlled by the energy delivered to the film. However, these explanations do not provide a clear understanding to the role of high oxygen flow on the formation of anatase phase.

## 6.3 The role of film thickness on the structure formation

As reported in [21, 23, 25, 26, 41], the structure of $TiO_2$ films strongly depends on their thickness. It has been found that the crystal structure of the fabricated films undergoes a gradual conversion from an amorphous to rutile to mixed anatase/rutile phase to a pure anatase phase with increasing the film thickness. Hence, to understand the growth mechanism upon increasing the film thicknesses, two series of $TiO_2$ films have been sputtered with variation of the thicknesses at low and high oxygen flow of 6.2 and 15 sccm, respectively. The standard deposition parameters have been applied i.e. dcMS mode at discharge current of 0.9 A and total sputtering pressure of 0.8 Pa; in addition to pre-sputtering for 3 h in the oxide mode to exclude the effect of temperature variation on the sample structure. The series have been also performed in a random array to demonstrate only the influence of the thickness on the structure. Figure 6.3 shows the grazing incidence XRD patterns of films grown at low oxygen flow (6.2 sccm) close to the transition regime. The amorphous phase is obtained at low thicknesses from 33 nm to 243 nm (samples T1- T4). Upon increasing the thickness to

303 nm (sample T5), a film with rutile phase (110) is formed. At 400 nm thickness (sample T6), the anatase phase (101) starts to take part in the structure and its contribution increased by further increasing of the thickness to 608 nm (samples T7-T8).

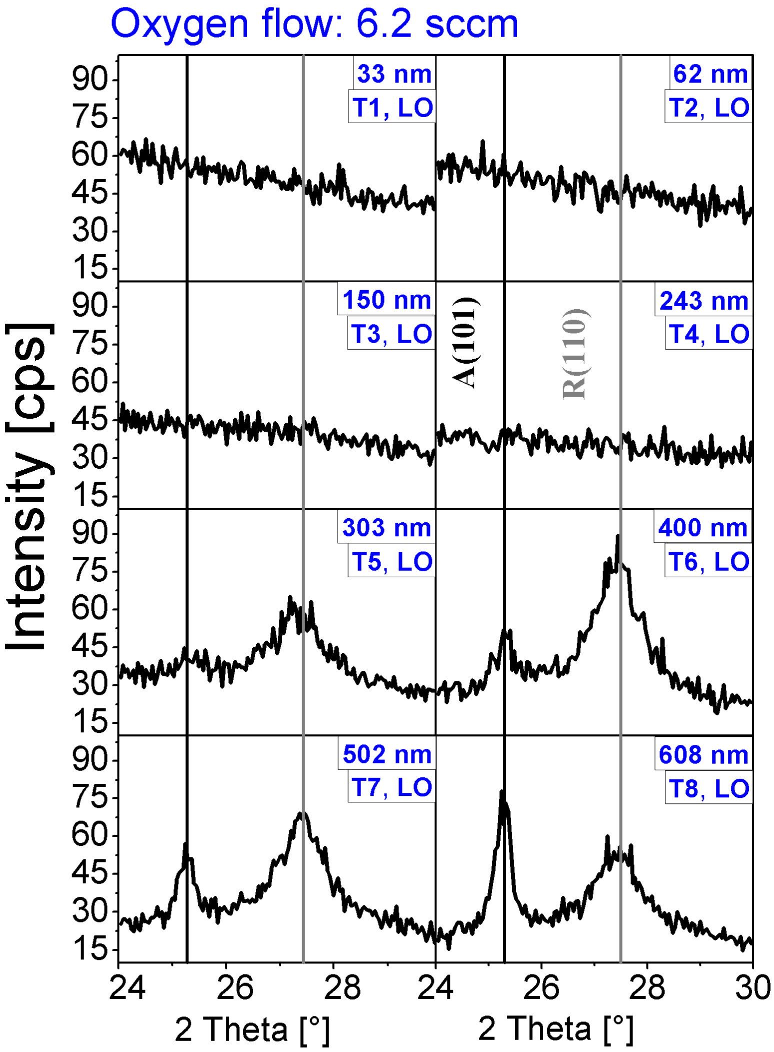

**Figure 6.3:** Grazing incidence XRD patterns of $TiO_2$ films with different film thicknesses. All films were deposited at low oxygen flow of 6.2 sccm. Thin films appear amorphous up to 243 nm samples (T1-T4). With increasing thickness to 303nm (sample T5), the rutile phase appears first, while the anatase phase starts to form at higher thicknesses of 400 nm (samples T6). Mixed films with high intensity of anatase phase are formed upon increasing the thickness (samples T7-T8).

The surface topography reveals a good correlation with the crystal structure as exhibited from AFM images, figure 6.4. It is evident that type 1 and type 2 features exist at the film surface. For the thinner films of 33 and 62 nm (samples T1-T2), an amorphous surface is observed. For films with a thickness of 150 and 243 nm (T3-T4), there is probably an amorphous background on which crystallites seem to form at separate sites. When the film grows thicker (303 nm (T5)), the background is formed by homogeneously distributed small crystallites (type 1 features) with the additional formation of large features (type 2) at separate sites. That pattern apparently continues as the film thickness increases up to 502 nm (T6- T7). For thick films 608 nm (T8), there is still a background of type 1 features but the large grains (type 2) seem to spread in the size, and form a closed surface.

The structure evaluation as a function of the film thickness has also been investigated at high oxygen flow (15 sccm). Figure 6.5 and figure 6.6 show the development of the crystal and surface structure of these films as displayed by grazing incidence XRD spectra and AFM images, respectively. At high oxygen partial pressure, the structural development of these films shows identical behavior as at low partial pressure (figure 6.3) except for the dominance of the anatase phase at low film thickness. The amorphous phase is obtained for thinner films of 33 and 64 nm (T1-T2). In comparison to low oxygen pressure, the rutile phase is formed at a lower thickness of 105 nm (T3), already. Moreover, a mixed anatase and rutile structure is formed at low thickness 151 nm (T4). For thicker samples, a pure anatase structure is apparently formed.

A similar scenario of the surface structure development at high oxygen partial pressure as at low partial pressure is also revealed by AFM images. The exception is that type 2 features dominate the surface and overgrown type 1 feature at low thickness of 201 nm (T5). For thicker films, a completely closed, dense-packed and rough surface with type 2 features is formed (samples T6-T9) and no more change in the structure is observed upon increasing the thickness. As presented in chapter 5 and reported in the literature [21, 24, 45], features 1 and 2 represent rutile and anatase grains respectively.

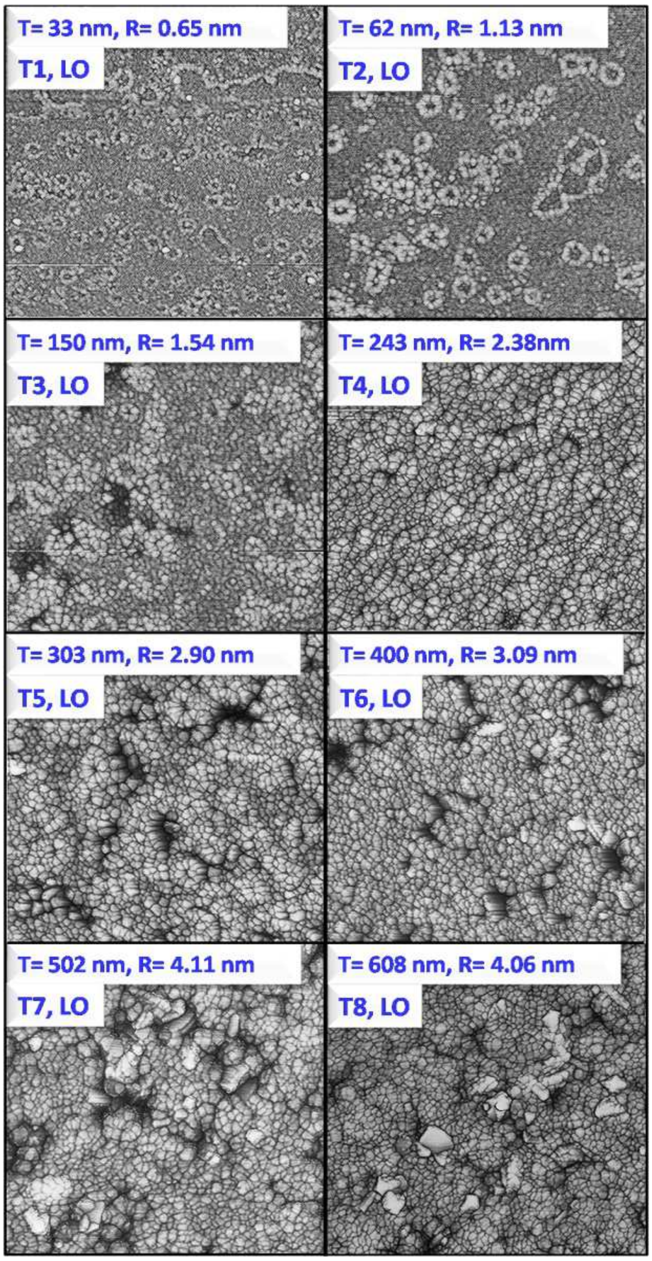

**Figure 6.4:** Surface topography of $TiO_2$ films with different thickness at low oxygen flow of 6.2 sccm. The corresponding XRD spectra for these films are shown in figure 6.3. Very thin films show no surface features (T1-T2). With increasing the thickness to 303 nm (T5), films are first governed by small, homogeneously distributed surface features (type 1). For thicker samples (T6- T7), large features (type 2) appear on the surface. These large features (type 2) overgrow and apparently dominate the surface. The scansize is 1×1 $\mu m^2$. Images are post-processed to enhance surface corrugation. R denotes the RMS roughness calculated from the AFM scans.

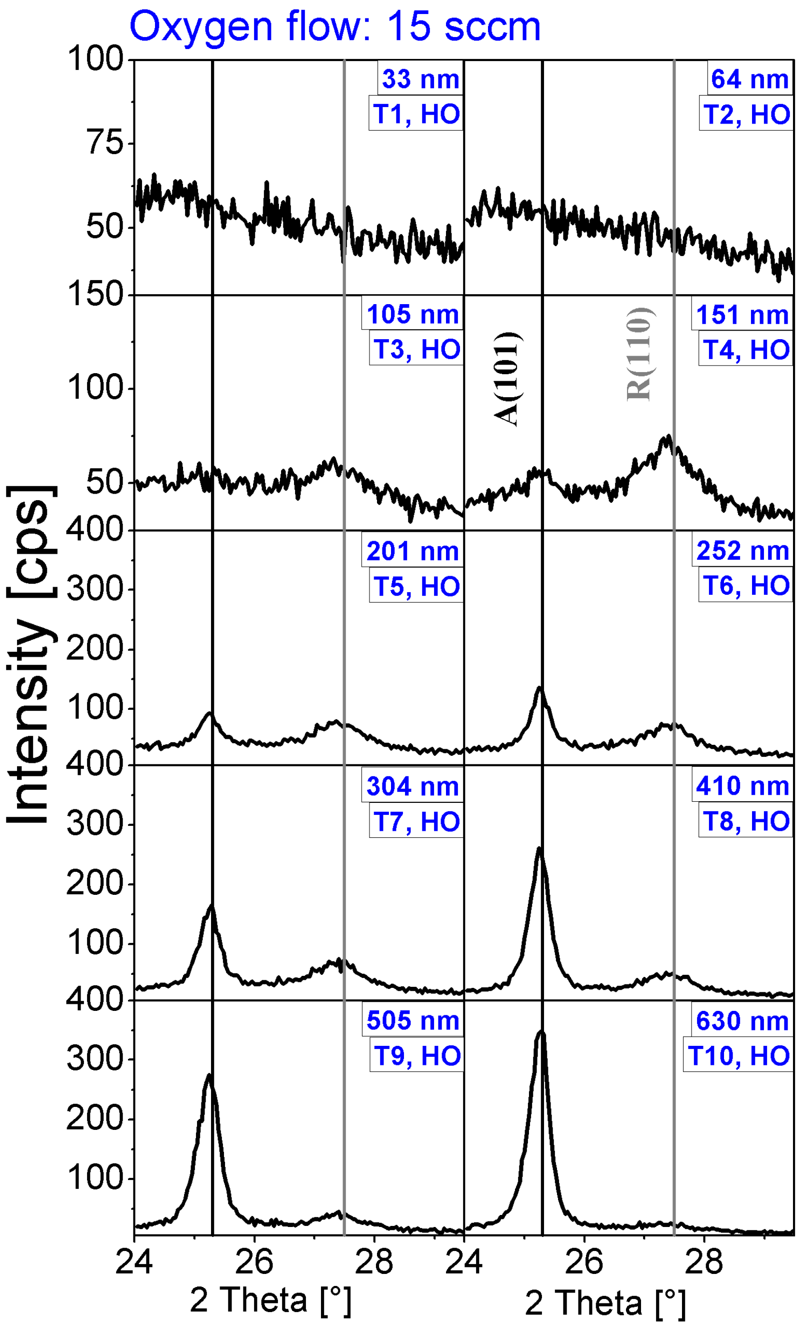

**Figure 6.5:** Grazing incidence XRD patterns of $TiO_2$ films with different thicknesses at a high oxygen flow of 15 sccm. Thin films appear amorphous (T1-T2). Increasing the thickness leads to formation of the rutile phase (T3-T4). The anatase phase forms upon further increasing of the thickness (T5-T7), until it dominates the structure at thicker films (T8-T10).

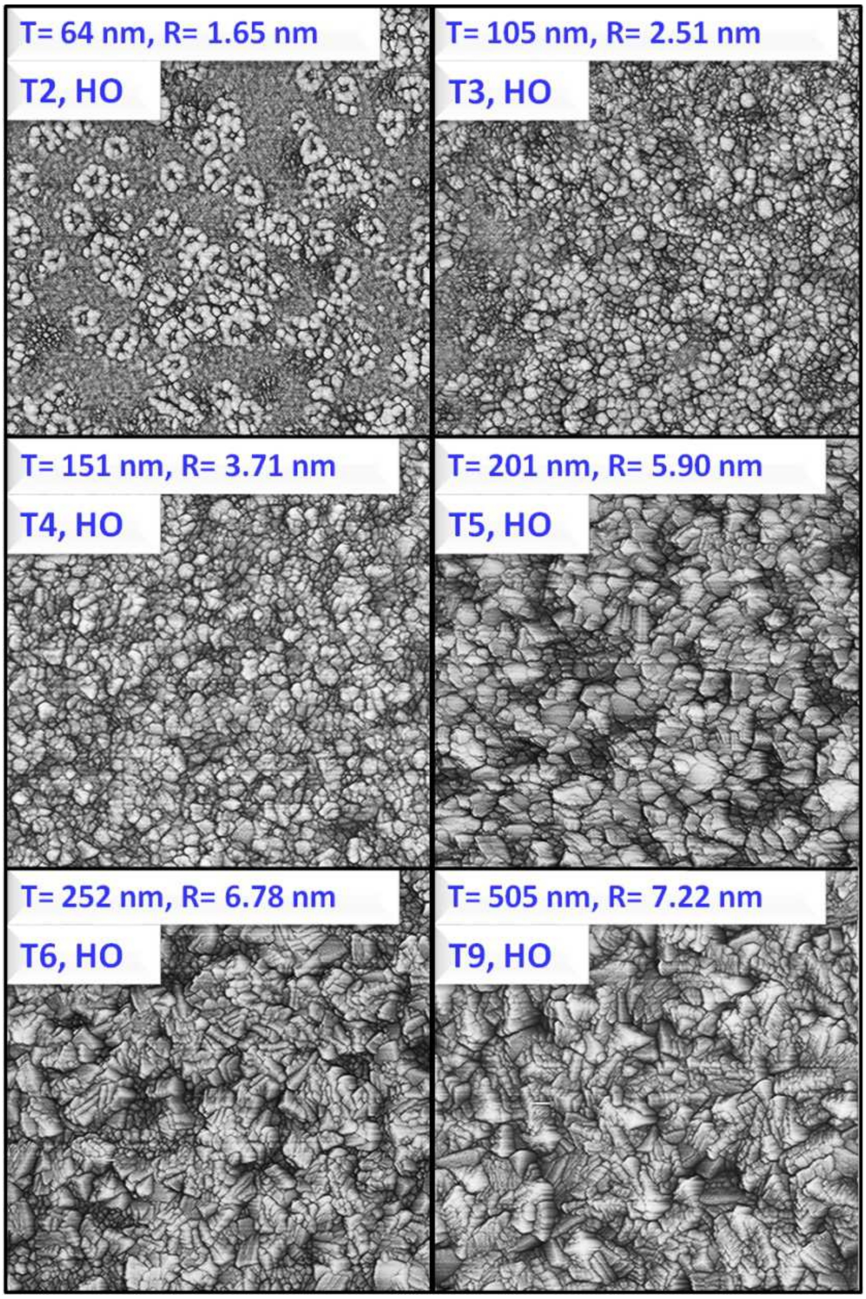

**Figure 6.6:** Surface topography of $TiO_2$ films deposited with different thicknesses at high oxygen flow of 15 sccm. XRD spectra of these films are shown in figure 6.5. Thinner films (T2) exhibit an amorphous background. The small features (type1) start to occupy the surface at higher thickness (T3-T4). A mixed surface of type 1 and type 2 features is formed with increasing the thickness to 201 nm (T5). The large features (type 2) continue to grow and overgrow type 1 features at higher thickness and dominate the surface completely (T6-T9). The scansize is 1×1 µm². Images are post-processed to enhance surface corrugation. R denotes the RMS roughness calculated from the AFM scans.

Investigations of $TiO_2$ films sputtered with different thickness either at low or high oxygen partial pressure indicate that the growth of the anatase phase is strongly favored at higher film thickness as well as at high oxygen partial pressure as shown in section 6.2. The change of the crystalline structure from rutile to anatase with increasing film thickness is in-line with the finding in the literature [21, 23, 25, 26]. It is apparent from XRD spectra that the anatase reflex decreases in width, which corresponds to an increasing of the vertical grain size. The rutile reflex in contrast does not change in width noticeably. Therefore, we have used the Scherrer equation [104] to estimate the anatase and rutile grain sizes for these series. Figure 6.7 shows the variation of the grain sizes and film roughness as a function of film thickness at low and high oxygen partial pressure. The rutile grains have small dimensions in comparison to the anatase grains and show only a slight change with the thickness. On the contrary, the anatase grains and the film roughness show a significant change with increasing the thickness especially at high oxygen partial pressure. There is a threshold thickness at which the anatase phase dominates the structure. Above this thickness, the anatase grain size and the film roughness show a slight change upon increasing the thickness while a decrease in the rutile grains is obtained.

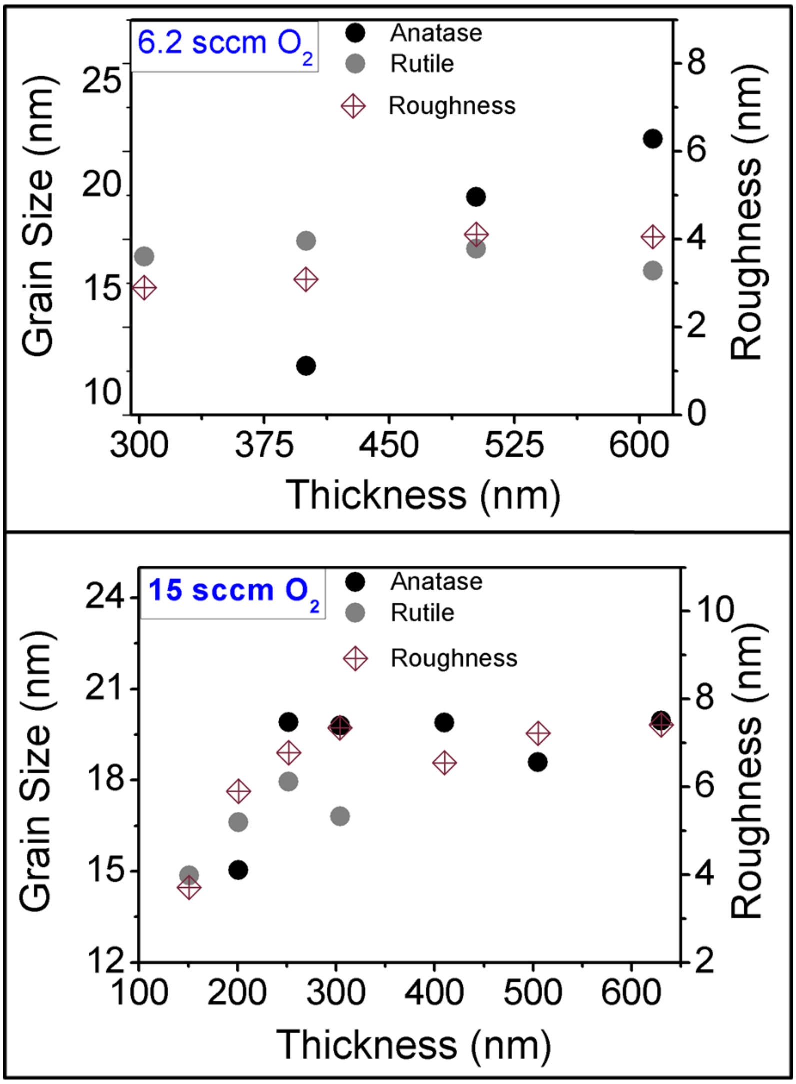

**Figure 6.7:** The lateral grain size of the anatase and rutile phases as estimated from the GI-XRD scans using Scherrer's equation, as a function of film thickness at low and high oxygen flows (6.2 and 15 sccm) respectively. The film roughness determined from AFM images is also shown. It is apparent that the rutile grains have small dimensions and a slight change is observed over the thickness range. For the anatase phase, there is a threshold thickness for each oxygen flow above which this phase grows. At this threshold thickness, the film roughness shows a significant increase.

To summarize these results, the structure undergoes a gradual change from amorphous to pure anatase via a mixed structure upon increasing film thickness both at low and high oxygen partial pressure. The higher the film thickness, the faster is the formation of the anatase phase. The anatase phase is preferred at high oxygen partial pressure even at low film thickness and the rutile structure seems to be buried with the anatase phase by increasing the thickness. This leads to an in-homogenous structure during growth with increasing thickness. To prove this, a small angle rocking curve scan has been performed on the films with different thicknesses.

## 6.4 Homogeneity of the film structure (Small Angle Rocking Curve)

As presented in the preceding section, there is a gradual change of the structure upon increasing of the film thickness. It seems that the rutile phase grows at the substrate interface in amorphous background and is gradually replaced by anatase with increasing thickness, as found in [26]. Therefore, this leads to the assumption that the structure is inhomogeneous. In order to prove this assumption, small angle rocking curve scans have been performed for films with variable thicknesses at a high oxygen partial pressure, by doing omega scans at several small angles of incidence for each phase (anatase and rutile) as shown in figure 6.8. As observed from the scan:

1) The first two samples at low thickness (T4, T5) have both structures present (rutile and anatase phases) at the film surface. This can be concluded from the fact that there is a sharp increase of the signals directly at the critical angle.

2) If films grow thicker (T6-T7), the rutile reflex is shifted to higher angles and is buried by the anatase. This is evident from the fact that the rise of the rutile intensity becomes delayed and does not exhibit a steep rise at the critical edge anymore.

3) Further increasing of the thickness causes an increase of the anatase reflex at the expense of the rutile reflex (T8-T9). For thicker films (T10), there is no rutile peak anymore in the scan.

4) The crystal quality of the rutile structure does not seem to increase with film thickness. This can be seen nicely from the first two samples (T4 & T5). There is no increase in the maximum intensity of the rutile reflex. This will be observed in the case of homogenous mixtures of anatase and rutile structure as present in section 6.5.

5) In case of the anatase reflex, the peak intensity clearly rises with increasing film thickness.

6) The surface roughness increases with increasing layer thickness which can also be concluded from the broadening of the transition at the critical edge.

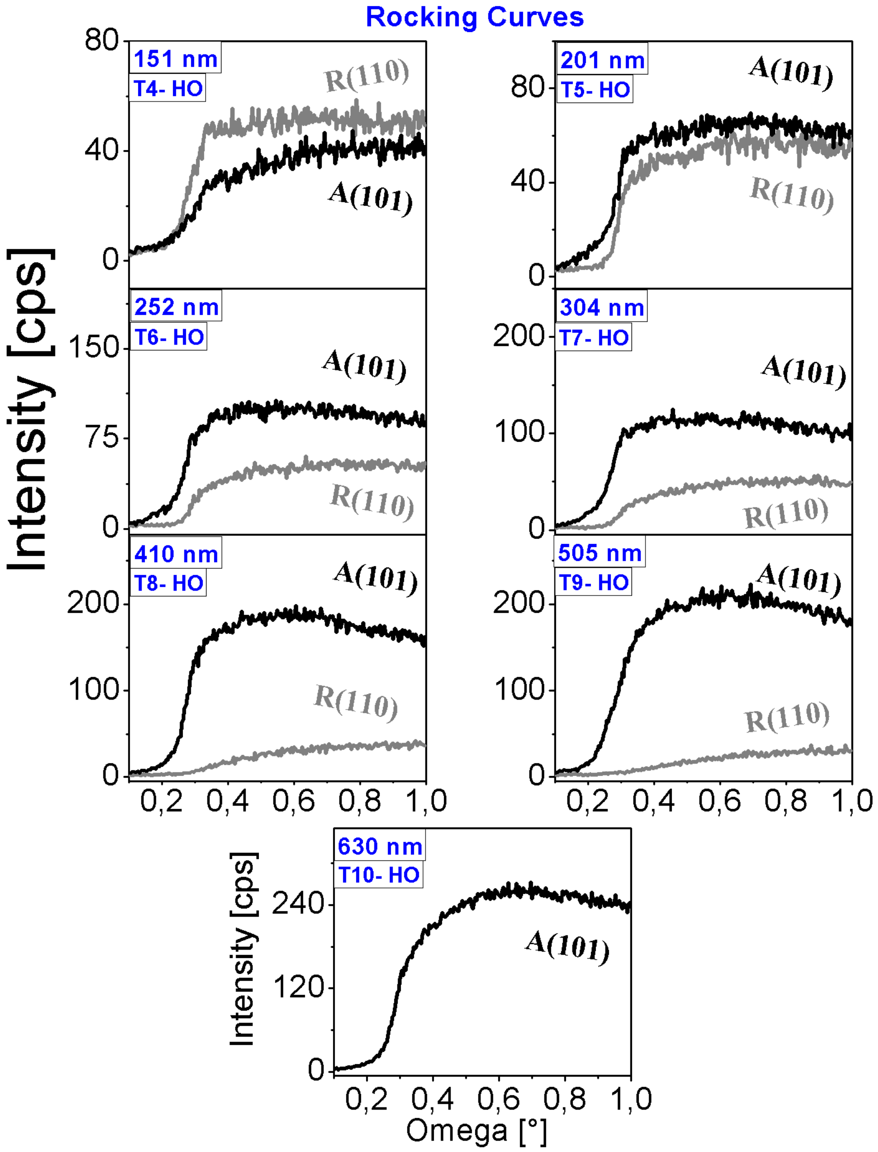

**Figure 6.8:** Small angle rocking curve scans of $TiO_2$ films with different thicknesses at high oxygen flow of 15 sccm. Corresponding XRD spectra are shown in figure 6.5. Samples (T4-T6) show a coexistence of rutile and anatase grains at the film surface. At higher thicknesses (T7-T9) the scans show the typical behavior of an overgrown rutile layer. The rutile phase is buried completely by the anatase phase at very high film thickness (T10).

This could be interpreted as a two layer system with some local structure gradient at the interface between rutile and anatase, i.e. an inhomogeneous structure has been obtained. A simplified postulated geometry has been developed to describe this variation of the structure as shown in figure 6.9.

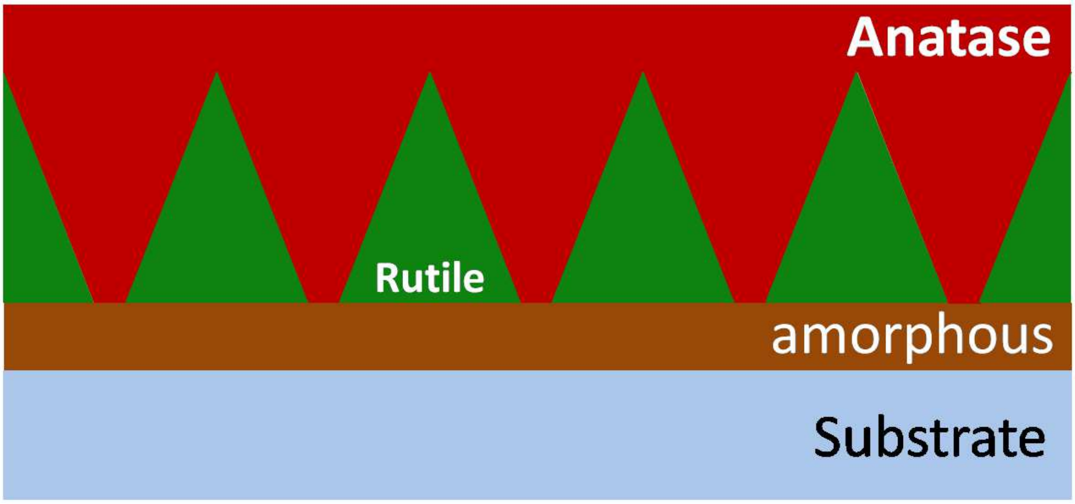

**Figure 6.9:** Model of a possible geometrical distribution of anatase and rutile grains based on the combination of AFM measurements and GI-XRD scans.

To confirm this geometrical model, one possibility is to use the depth information about the film structure that is included in the intensity of small angle rocking curves (figure 6.8). To interpretate the x-ray signal intensity, at first a model needs to be developed. The intensity is then calculated using the model and the result can be compared with the measurement. If the model adequately fits the measurement, the model parameters are likely to correctly describe the geometrical film structure. This model will also show the expected structure distribution for homogenous and inhomogeneous layers.

## 6.5 Modeling of the small angle rocking curve scans

In this section, a mathematical model has been developed by Dominik Köhl [138] to describe the reflected beam intensity for the small angle rocking curve. This model is based on a geometrical consideration for the $TiO_2$ film structure. Figure 6.10 shows a sketch of the geometry for a small angle rocking curve and the principle of the model.

The x-ray beam hits the sample surface at typically very small angles of incidence with respect to the sample surface (e.g. $0° < \omega_1 < 2°$). If $\omega_1$ is larger than the angle of total reflection, the beam propagates through the medium and is diffracted at crystallites according to Bragg's law. The fraction of crystallites with suitable orientation leads to an increased signal intensity at the detector placed at a fixed position $2\theta$ with respect to the incident beam. On propagating through the film, the beam is attenuated, which can be described by an exponential law with a decay length $\alpha$:

$$I(l) = I_0 \cdot e^{-\alpha l} \quad \text{with} \quad l = l_1 + l_2$$

Where, *l* is the path length of the beam through the medium. Note that this length corresponds to the sum of the incident beam and the diffracted beam, figure 6.10.

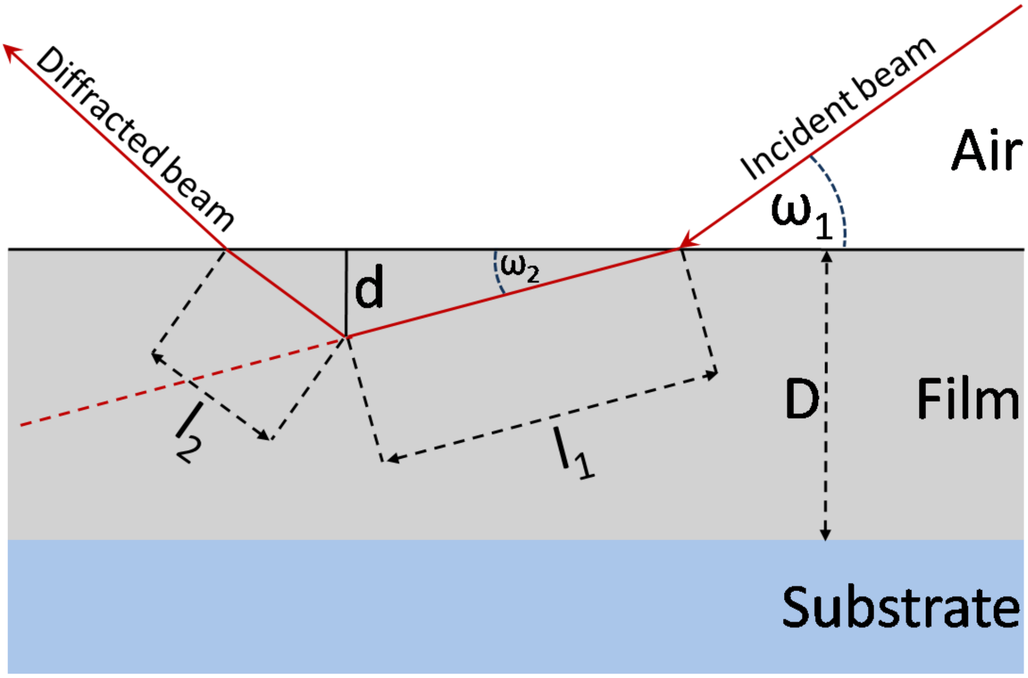

**Figure 6.10:** Sketch of the geometry of a small angle grazing incidence measurement.

Before we can calculate the diffracted intensity, a few geometrical considerations have to be done. First of all we should note that 1/α >> D, where D is the total thickness of the film. This means that for small angles of incidence we can simplify the expression for the total path length of the beam and link this with the vertical penetration depth into the sample:

$$l = l_1 + l_2 \approx l_1, \quad d \approx l \cdot \sin \omega_2$$

Furthermore: $\cos \omega_1 = n \cdot \cos \omega_2$ and $\cos \theta_c = n$

Where $n$ is the refractive index of the medium and $\theta_c$ is the angle of total reflection. Substituting the second equation into Snell's law, performing a series expansion and only considering terms up to first order in ω directly leads to: $\omega_2 \approx \omega_1 - \theta_c$ for small angles.

To calculate the diffracted intensity, we now need to sum over all possible contributions:

$$I(\omega_1) \propto \int_0^{D/\sin(\omega_1 - \theta_c)} S(d(l)) \cdot e^{-\alpha l} \cdot \left( \frac{\sin \omega_1}{\sin \omega_0} \cdot \theta(\omega_0 - \omega_1) + \theta(\omega_1 - \omega_0) \right) dl$$

Where $I$ is the intensity measured at the detector, $S$ is a geometrical structure factor which is unity only for a completely homogeneous distributions of scattering centre through the film. The term in parentheses corrects the signal intensity for the limited width of the detector. For extremely small angles of incidence only a fraction of the beam actually is detected due to the limited observable spot size visible to the detector. $\Theta$ is the Heaviside function which is a non-continuous function whose value is zero for negative argument and one for positive argument and $\omega_0$ is the angle above which the full irradiated area is visible to the detector.

In our experiments usually a collimator is used in the diffracted beam optics such that the visible spot length is in the range of 1 cm. In the incident beam optics a very narrow divergence slit is employed resulting in a very sharp beam with small angular spread. It can be easily shown that in this case $\omega_0 < \omega_1$ and hence the last term in the integral may be ignored.

To describe the intensity of titania films, the remaining task is now reduced to finding suitable expressions for $S$ for the rutile and the anatase grains separately. As the irradiated area is typically much larger than the lateral width of the film microstructure, it is sufficient to model the thickness dependency of the volume fraction of anatase to rutile. The parameters used are shown in figure 6.11. $D$ is the total film thickness without the amorphous interlayer at the substrate interface and $a$ the included thickness of a purely anatase top layer. The values $C_{a,t}$ and $C_{a,b}$ are the anatase volume fractions at the top and at the bottom of the rutile regions.

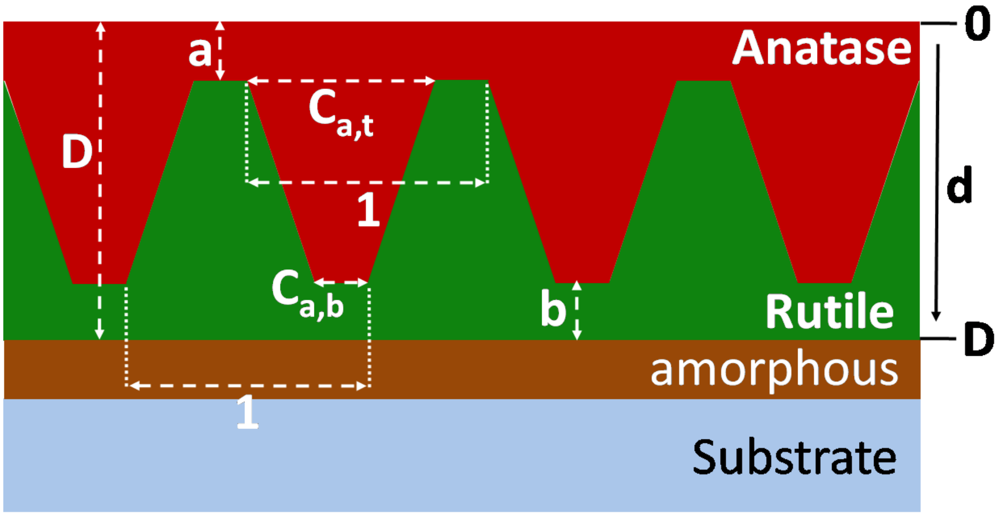

**Figure 6.11:** Description of the model parameters used. The film is treated as a three layer system with a linearly graded interface. The geometry shown in figure 6.9 is a special case of this more general model.

It can be easily shown that the intensity of the anatase signal can be described by:

$$I_A(\omega_1) \propto \int_0^{a/\sin(\omega_1-\theta_c)} 1\cdot e^{-\alpha l}\,dl + \int\limits_{a/\sin(\omega_1-\theta_c)}^{(D-b)/\sin(\omega_1-\theta_c)} \left( (C_{a,t}-C_{a,b})\frac{D-b-d(l)}{D-b-a} + C_{a,b} \right)\cdot e^{-\alpha l}\,dl$$

and the rutile intensity is described by:

$$I_R(\omega_1) \propto \int_{(D-b)/\sin(\omega_1-\theta_c)}^{D/\sin(\omega_1-\theta_c)} 1\cdot e^{-\alpha l}\,dl + \int\limits_{a/\sin(\omega_1-\theta_c)}^{(D-b)/\sin(\omega_1-\theta_c)} \left( 1-\left( (C_{a,t}-C_{a,b})\frac{D-b-d(l)}{D-b-a} + C_{a,b} \right)\right)\cdot e^{-\alpha l}\,dl$$

with

$$d(l) = l \cdot \sin\omega_1 - \theta_c$$

To correct for different scattering amplitudes of the rutile and the anatase grains, suitable correction pre-factors may be used to scale the two signals. It should be noted that all possible film geometries based on linear gradients can be modeled with the developed model. E.g. the parameter sets:

$$\left[a=\frac{D}{2}, b=\frac{D}{2}\right] \text{ (1) and } \left[a=b=0, C_{a,t}=C_{a,b}=0.5\right] \text{ (2)}$$

Correspond to the extreme cases of (1) a simple two layer system with equal thicknesses of the rutile and anatase layers with a sharp interface and (2) a homogeneous mixture of rutile and anatase through the medium.

A small maple script has been written to perform the integrations and to plot the calculated intensities. To demonstrate the impact of different layer stack geometries on the signal intensity, four different layer stacks are simulated as shown in figure 6.12.

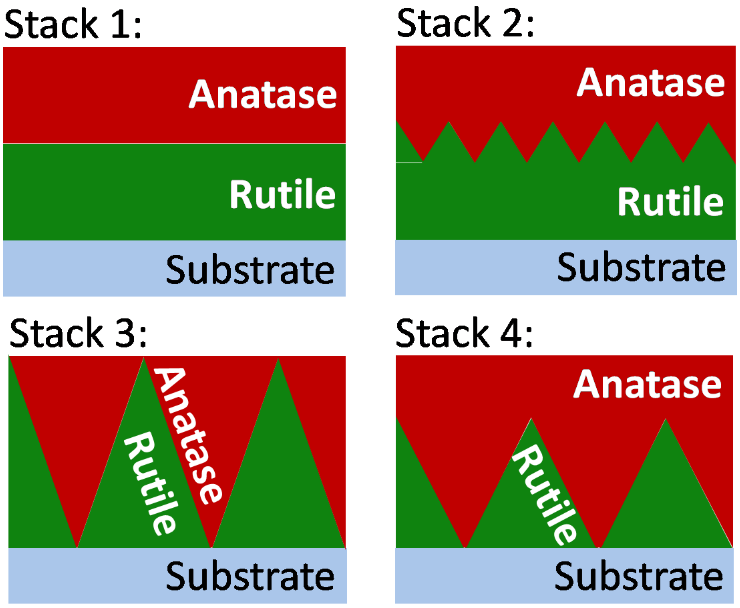

**Figure 6.12:** Geometries of the four different layer stacks that are simulated as an example.

The anatase and rutile signals have been calculated for these four stack geometries for films with different thicknesses. One simulation reproduces our XRD and AFM results well (Stack 4). The simulation result of the appropriate layer stack is presented in figure 6.13.

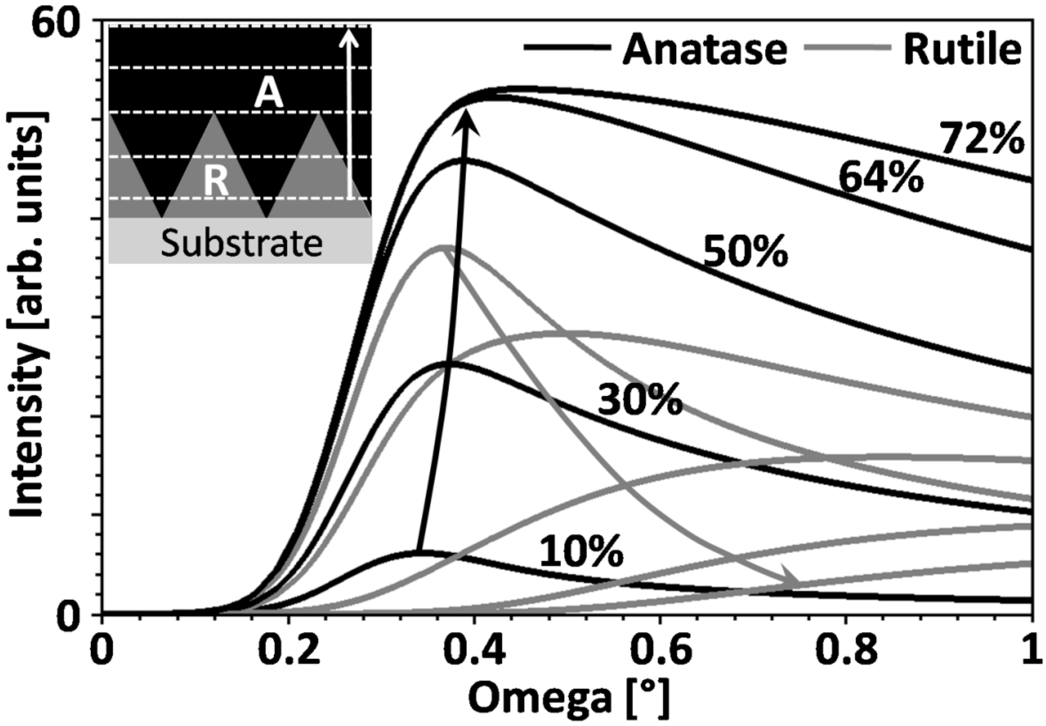

**Figure 6.13:** Simulation of small angle rocking curves for a film with an inhomogeneous distribution of the rutile and anatase grains. In the model (inset), the film is assumed to be purely rutile at the substrate interface. With increasing thickness, the anatase content increases linearly until it completely governs the structure at larger thicknesses. The corresponding rocking curve spectra have been simulated for different growth stages (thicknesses) as marked by the dotted white lines (inset). In the simulated spectrum, dotted arrows indicate increasing film thickness. The thinnest film (10% anatase) is characterized by a large rutile content with a small anatase contribution. The spectrum shows a small anatase intensity and a large rutile contribution. Upon increasing the thickness (30% and 50%), the anatase intensity increases while the rutile intensity decreases at the same time. Both intensities decrease at larger angles as the x-ray beam passes through a smaller volume fraction of the crystalline structure. At larger thicknesses (64% and 72%), the film is characterized by a complete anatase top layer. In this case, the increase in rutile intensity is shifted towards larger angles and still increases at 1°. This behavior is characteristic for a layer which has been overgrown by another structure.

We can draw some conclusions from these results:

- The intensities change drastically if there is a pure anatase top layer.
- The decrease in the rutile signal with increasing thickness can be explained by a rutile layer which is buried by an anatase layer.
- The rutile reflex does not only depend on the number of rutile grains but also on their geometrical distribution.
- The ratio of the anatase and rutile intensity is strongly dependent on both the angle of incidence and the geometrical structure of the film.
- The weight percentage of anatase and rutile phases in a mixture can be determined from XRD measurements using the empirical formula $W_A = \frac{1}{1+1.265 I_R / I_A}$ [139], where $I_A$ denotes the intensity of the strongest anatase reflection and $I_R$ is the intensity of the strongest rutile reflection.
- This calculation is not applicable in the case of in-homogenous structure, since this formula only considers fixed intensity ratios of anatase and rutile phases at all angles of incidence. From simulations as shown in figure 6.14, we find that this prerequisite is only fulfilled for homogeneous mixtures of anatase and rutile. Hence this formula is suitable only for powder samples rather than for sputtered films.

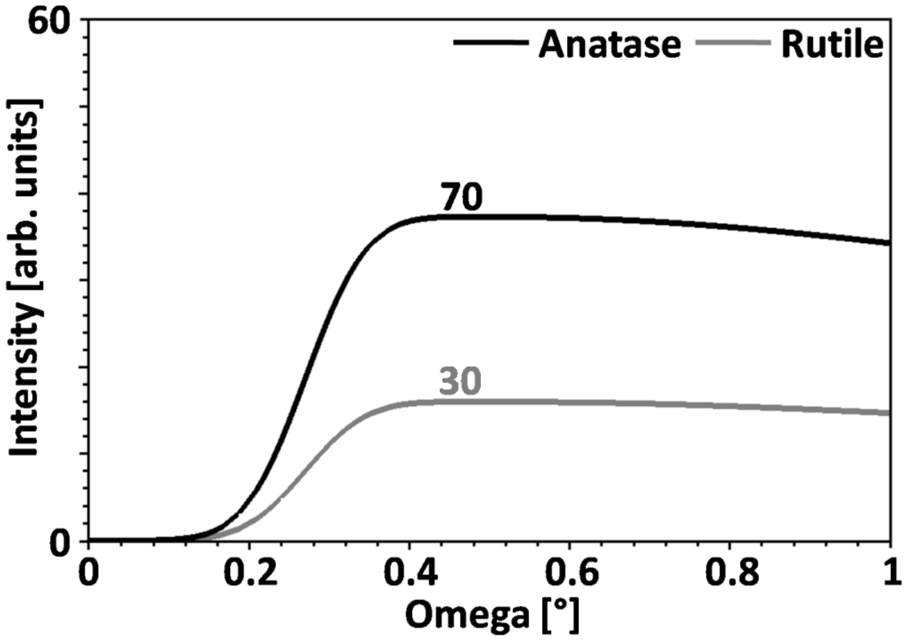

**Figure 6.14:** Simulation of a small angle rocking curve for a film consisting of a homogeneous mixture of rutile (30%) and anatase (70%) grains. For simplicity, the diffraction intensities were assumed to match in case of equal volume fractions of rutile and anatase. Apparently, the ratio of intensities is independent of the incidence angle. This is expected for a film that does not show any inhomogeneous depth distributions.

Additionally, from the simulations of other stacks, it is obvious that if a constant quality (no gradient with film thickness) of the anatase or rutile grains is assumed, there is no change in the position of the maximum reflex intensity of the topmost layer with increasing film thickness. In consequence, as soon as the surface of the film is fully closed by e.g. a purely anatase layer, there should be no further intensity rise with increasing film thickness. This is of course different from what is typically observed. This discrepancy can only be explained by a gradual change of the reflected intensity with growing film thickness, i.e. a change of crystal quality. The intensity usually starts to increase already at lower angles and does not instantaneously reach the maximum value exactly at the angle of total reflection. This behavior can be explained by surface roughness. Usually sputtered samples exhibit a rough surface topography which leads to some variation in the angle of incidence.

In summary, this model and the simulations confirm our postulated geometrical distribution which is shown in figure 6.9. Also it reveals that there is an inhomogeneous distribution of the rutile and anatase phases of the sputtered $TiO_2$ films upon increasing of the film thickness

## 6.6 Microstructure

To clarify the change in the film growth with increasing film thickness, TEM measurements have been performed on two selected samples (T1 and T2) fabricated at low oxygen flow of 5.5 sccm with different thicknesses of 404 and 620 nm. These films show a mixed rutile/ anatase structure and a pure anatase phase, respectively as shown in figure 6.15.

The cross-section TEM image of the mixed structure (404 nnm) exhibits a microstructure with mountain-like crystals at the interface and a thin layer at the top surface as shown in figure 6.16. The corresponding diffraction pattern indicates that the large crystals at the bottom layer possess a rutile structure with some reflections from the silicon substrate. The anatase phase is detected at the top layer of the film.

The images in figure 6.17 show crystalline columns with a conical shape. The growth starts with a seed layer at the substrate-interface with approximately few nanometers. The first columnar crystallites with conical shape start to grow from the seed layer. These crystallites extend throughout the whole layer with further film growth until the layer completely consists of columnar microstructure with cone-shaped crystallites. The individual grains at the top position in the diffraction pattern reveals that the columns are typically assigned for anatase structure as integrated and shown in the intensity spectra (c). On the other hand, the seed layer which observed at the bottom layer of the film referred to rutile phase with some reflection from the silicon substrate.

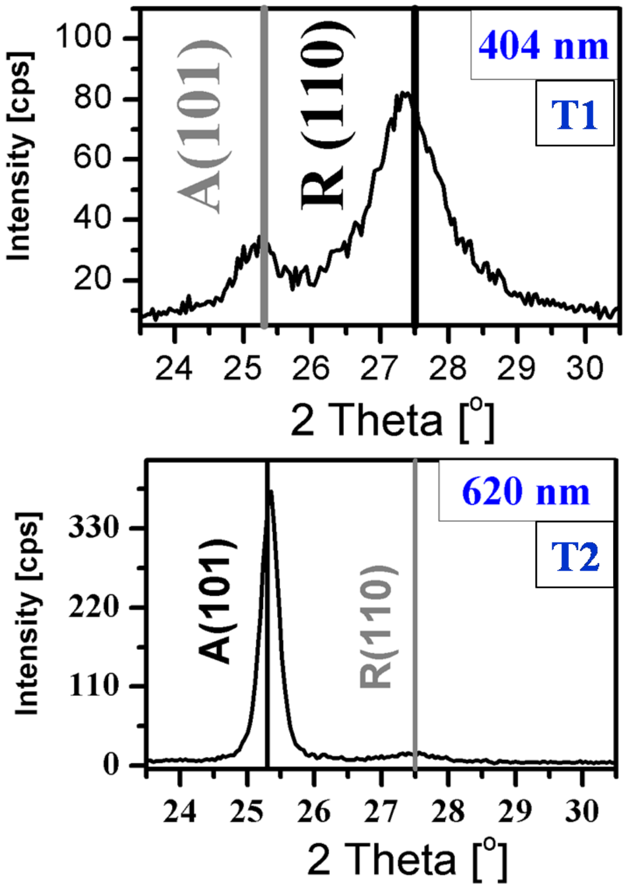

**Figure 6.15:** Grazing incidence XRD scans of $TiO_2$ films deposited at low oxygen flow of 5.5 sccm with different film thicknesses (T1 and T2). The thin film (T1) shows a mixed structure with a large rutile contribution while T2 possesses a purely anatase structure.

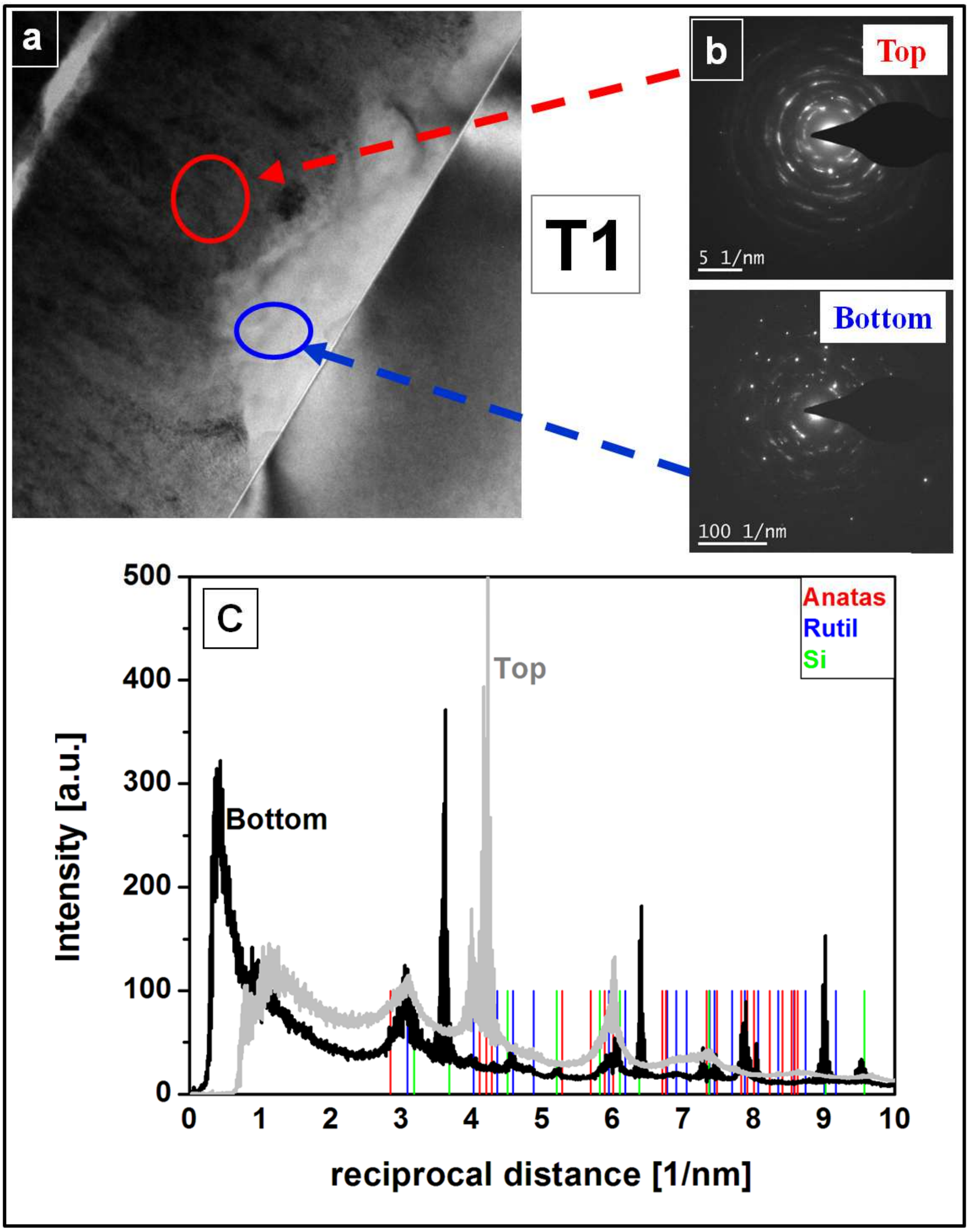

**Figure 6.16:** Cross-sectional TEM image of $TiO_2$ thin film (T1) with a thickness of 404 nm (rutile rich). (a) Shows bright field image of the film, (b) the corresponding diffraction pattern at different positions (top and bottom layer) of the sample and (c) represents the intensity of the different diffraction patterns. The film shows a columnar microstructure, the bottom layer is assigned to the rutile phase which a thin layer grows on the top with anatase phase as seen from the diffraction patterns.

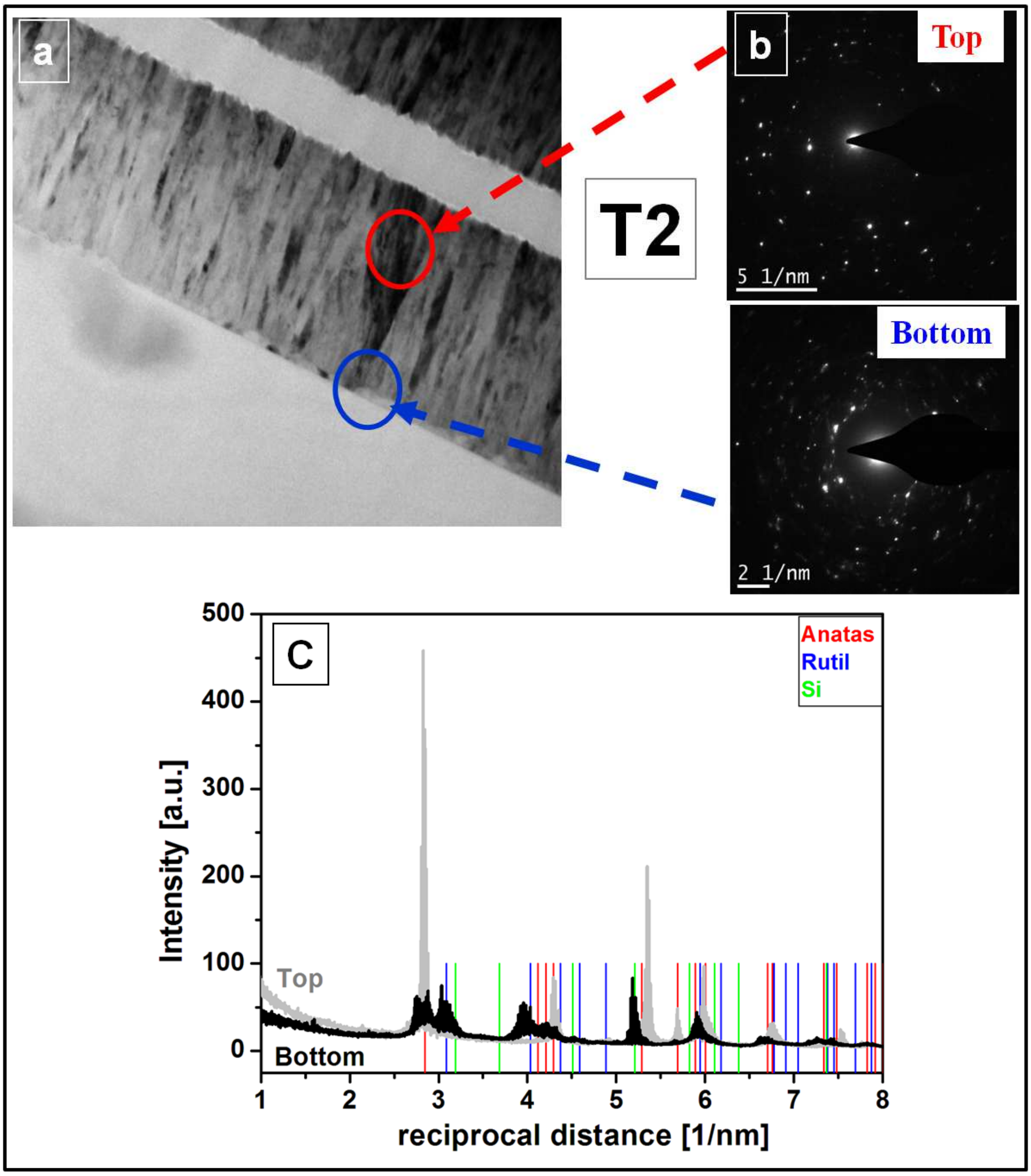

**Figure 6.17:** Cross-sectional TEM image of $TiO_2$ thin film (T2) with thickness of 620 nm (purely anatase structure). (a) Shows bright field image of the film, (b) the corresponding diffraction pattern at different positions (top and bottom layer) of the sample and (c) represents the intensity of the different diffraction patterns. The film shows a columnar microstructure, since a column with conical shape is growing at the top layer with anatase phase. The thinner layer which grows at the interface (the bottom layer) possesses a rutile phase as can be seen from the diffraction patterns.

These results demonstrate that the reactively sputtered $TiO_2$ thin films have a columnar microstructure and show an in-homogenous distribution of the anatase and the rutile phases. The columnar growth of $TiO_2$ thin films has been observed and reported in the literature [24, 32, 35, 121, 140, 141]. The TEM observations explain the structure variation with increasing thickness and the complete replacement of the rutile phase by anatase. The rutile phase grows at the interface and is completely overgrown by anatase upon increasing the thickness. These results are consistent with XRD and AFM scans and confirm the postulated geometrical distribution model (figure 6.9).

## 6.7 Influence of buffer layer and heating on the structure formation

The substrate temperature and the post-annealing treatment parameters have a strong influence and play an important role in the crystallization of $TiO_2$ thin films, as reported in the literature (e.g. [23, 25, 32, 45, 141] ). It has been shown that the crystallinity of the anatase phase is improving upon increasing the temperature, while the transition to the rutile structure is observed at a higher temperature of 700°C.

In order to demonstrate the influence of substrate heating and the $TiO_2$ buffer layer on the structure formation, series of samples have been deposited upon changing oxygen flow during deposition. Another series has been recorded with substrate heating at a temperature of 400°C. The depositions were carried out at standard sputtering conditions, a total pressure of 0.8 Pa and a discharge current of 0.9A. Figure 6.18 shows the grazing incidence XRD scans from the sample centre and the sample edge for a series of samples deposited at different conditions. The left column represents $TiO_2$ thin films which have been used as buffer layers for the continuous films in the right column.

1. Low flow series (5.5 sccm $O_2$): thin buffer layer with rutile structure has been deposited at low oxygen partial pressure as shown on the left side. Switching from low to high flow (15 sccm $O_2$) leads to the formation of an anatase phase (on the right side). Strong anatase peak above the racetrack is observed due to the target aging (old target).
2. High flow series (15 sccm $O_2$): thin buffer layer at high oxygen partial pressure is also characterized by the nucleation of the anatase phase. Consequently, a high oxygen flow in combination with a low bombardment at the substrate edge leads to a superior quality of the anatase structure. No significant change observed in the structure at the sample centre upon switching from high flow to low flow (15 → 5.5 sccm $O_2$).

3. Heating series (low oxygen partial pressure at 400°C): the films in this series have been deposited at a substrate temperature of 400°C at low oxygen flow of 5.5 sccm $O_2$. Heating in the early stage of film growth only produces a buffer layer that promotes anatase growth while heating for the full growth time yields a superior anatase structure. Moreover, the heating leads to complete transition of the structure from rutile to pure anatase, the buffer layer in low flow series (1) and the continuous film of the heating series (3). This illustrates that the substrate heating during deposition has the same influence on the structure as a high oxygen partial pressure or a low oxygen ions bombardment.

In summary, these results reveal that the nucleation of the anatase phase is favored at high oxygen partial pressure as well as in the presence of low oxygen content in the process combining with substrate heating. The growth of anatase phase under these conditions might be ascribed to the annihilation of defects which are preferentially created during film growth. These defects are considered to be oxygen vacancies which are created by preferential oxygen sputtering [142, 143]. The defects are formed by weak sputtering of the surface or bombardment the substrate by negative oxygen ions [144] or by $Ar^+$ ions [143]; which leads to a preferential loss of oxygen atoms from the deposited layer. These defects can be removed by substrate heating or by applying high oxygen partial pressure. It has been found that the oxygen deficiency decreases with annealing [144], annealing in oxygen atmosphere [145] and with increasing oxygen concentration in the sputtering gas [59]. On the other hand, since the $Ar^+$ sputtering of stoichiometric $TiO_2$ leads to preferential loss of O from the near surface region [143] and as mentioned earlier that higher irradiation of $Ar^+$ strongly assists the the growth of rutile phase through the formation of O vacancies [136]. It is also known that the rutile phase can accept a larger defect density than pure anatase [35]. Therefore; growth of rutile structure is preferential at conditions that promote a large number of defects (at low partial pressure or energetic ion bombardment).

The origin of the oxygen vacancies can be explained as follows: $TiO_2$ surface can contain a substantial amount of oxygen defects and interstitial Ti defects [146]. The Ti interstitial defects are mostly found in bulk because it prefers to have a high coordination. On the other hand, the oxygen vacancies with undercoordinated surface sites are energetically favored where a smaller number of Ti-O bonds need to be broken. These defects are frequent on the anatase and rutile surfaces. The oxygen vacancies can be found on the surface and the subsurface sites in both phases. The oxygen vacancies on the surface are corresponding to the removal of a surface twofold bridging oxygen ($O_{2c}$). It has been found that for rutile (110) phase, the formation energy of surface ($O_{2c}$) vacancies is lower than that of subsurface vacancies. In the case of anatase (001) and (101) surfaces, the oxygen vacancies have lower formation energy in the subsurface than at the surface. Based on the density- functional theory (DFT) calculations, the formation energy of oxygen vacancies at the surface sites of (4.15 eV) is lower than in the subsurface region for the anatase (101) phase and the anatase (001). While for rutile (110) phase, the formation of surface bridging oxygen vacancies with formation energy of (3.68 eV) and sub-bridging vacancies are most likely. Also, the concentration of surface oxygen vacancies is quite large (5%-10%) on rutile phase under standard preparation conditions. The formation energy ($E_f$) is defined as the difference between the sum of the total energy of the defect surface ($E_{ds}$) and the removed oxygen species ($E_o$) and the perfect surface state ($E_{ps}$). $E_f = (E_{ds}+E_o)-E_{ps}$. The smaller the $E_f$, the higher is the formation probability [146]. Therefore, it is expected to find a high concentration of oxygen vacancies at the surface in rutile (110) phase than in anatase (101) phase.

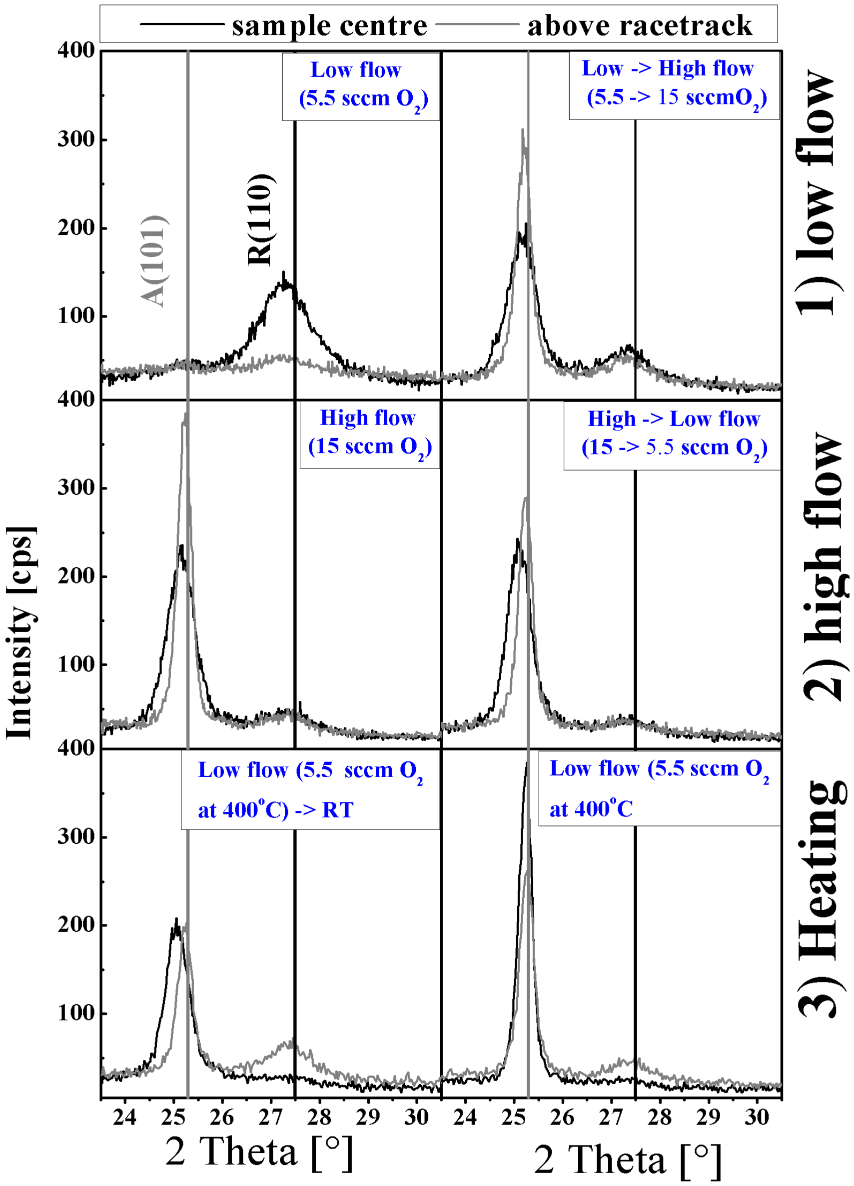

**Figure 6.18:** Grazing incidence XRD patterns of $TiO_2$ films sputtered at different conditions. The left and right columns show the $TiO_2$ buffer layer and the continuous film respectively. A buffer layer with rutile structure formed at low oxygen flow (5.5 sccm $O_2$) while the anatase phase dominates the structure at high oxygen flow (15 scsm $O_2$) [1) low flow series]. The high oxygen flow promotes the formation of the anatase phase and no significant structure change is observed upon changing to low flow (15→ 5.5 sccm) [2) high flow series]. Heating at 400°C at low oxygen flow for the full growth time leads to a superior anatase structure, as shown in [3) heating series].

## 6.8 Structure zone model

Based on the preceding results, a structure zone model for reactively sputtered $TiO_2$ thin films has been established to describe the structure variation as a function of the different process parameters. It has been shown that the crystal structure as well as the surface structure of sputtered $TiO_2$ thin films is strongly influenced by several parameters, such as the oxygen partial pressure, the oxygen ion bombardment and the film thickness.

Figure 6.19 shows a schematic diagram which exhibits the variation of the structure from the amorphous structure to the anatase phase via a mixed (rutile/anatase) state as a function of increasing oxygen partial pressure and oxygen ion bombardment on the X-axis and the Y-axis, respectively. This model is valid for films with identical thickness and deposited on unheated substrate. The darker region corresponds to a higher crystallinity of anatase structure while the gray colour represents a mixed or rutile structure.

- Increasing the oxygen flow: the structure undergoes a transformation from the amorphous-mixed (rutile/anatase) - to anatase phase.
- Increasing the oxygen ion bombardment: variation of the structure moves in the opposite direction of increasing the oxygen content. Crystallinity of anatase films show deterioration upon applying energetic ion bombardment, even higher ion bombardment leads to formation of amorphous structure.
- Reducing the oxygen ion bombardment by utilizing vertical substrate geometry leads to superior anatase structure.

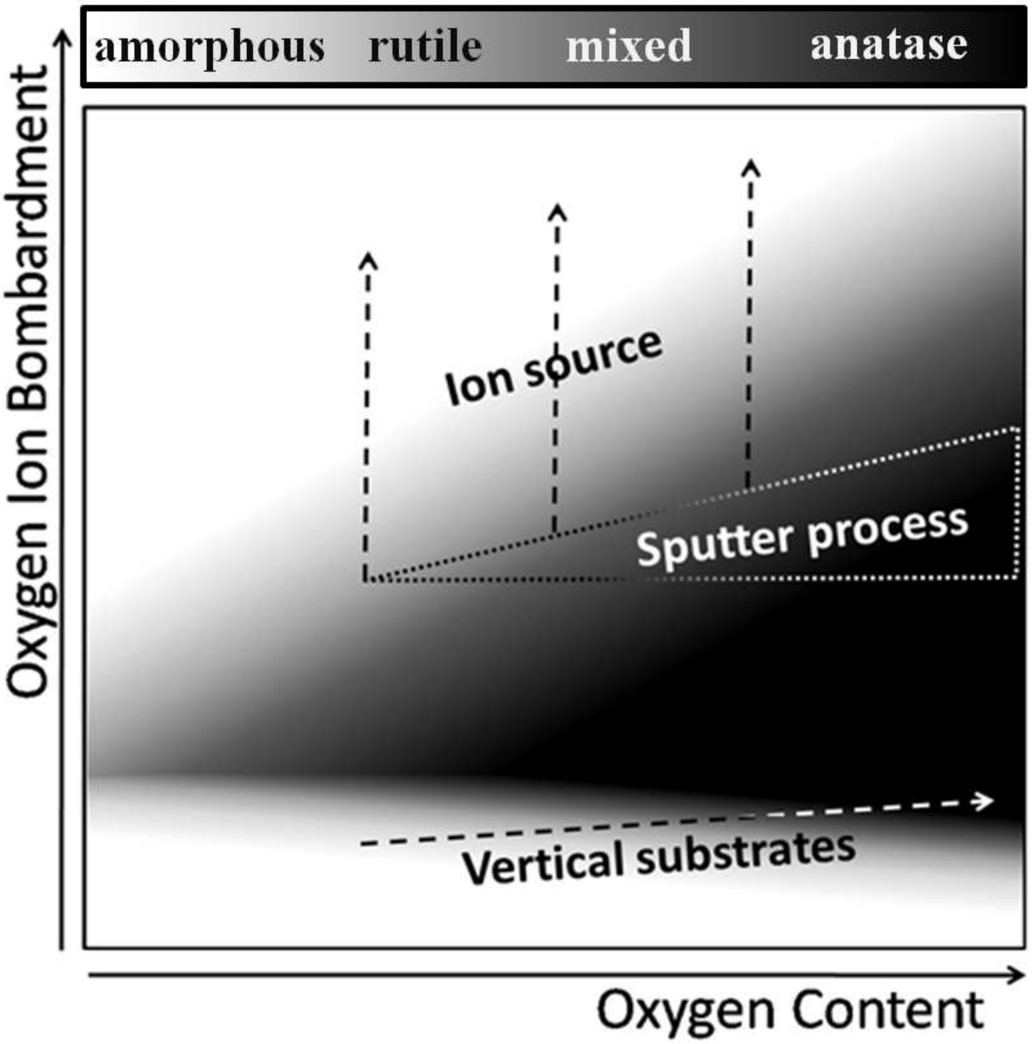

**Figure 6.19 :** Structure zone model for sputtered $TiO_2$ thin films which describes the influence of increasing the oxygen content (X-axis) and oxygen ion bombardment (Y-axis) on the structure formation. Increasing the oxygen content leads to improvement of the anatase structure while the oxygen ion bombardment has the opposite effect on the structure. This model is valid for films with identical thicknesses and on unheated substrate.

The variation of the film structure as a function of film thickness for thin and thick films is shown in figure 6.20. The X-axis and Y-axis also represent increasing the oxygen content and the oxygen ion bombardment, respectively. For thin films (the left diagram), the amorphous and mixed phases seem to govern the structure over the oxygen flow range while a small contribution of the anatase phase is observed at high oxygen partial pressure. On the other hand, the film structure is governed by anatase phase for thick films even at low oxygen partial pressure. The dark colour represents the improved crystallinity of the anatase phase while the bright one represents amorphous and mixed structures. Increasing the oxygen bombardment leads to formation of an amorphous structure and a mixed structure in thicker films. The absence of the anatase structure for higher ion bombardment is observed in both cases (thin and thick films). This model is also valid for films deposited on unheated substrates.

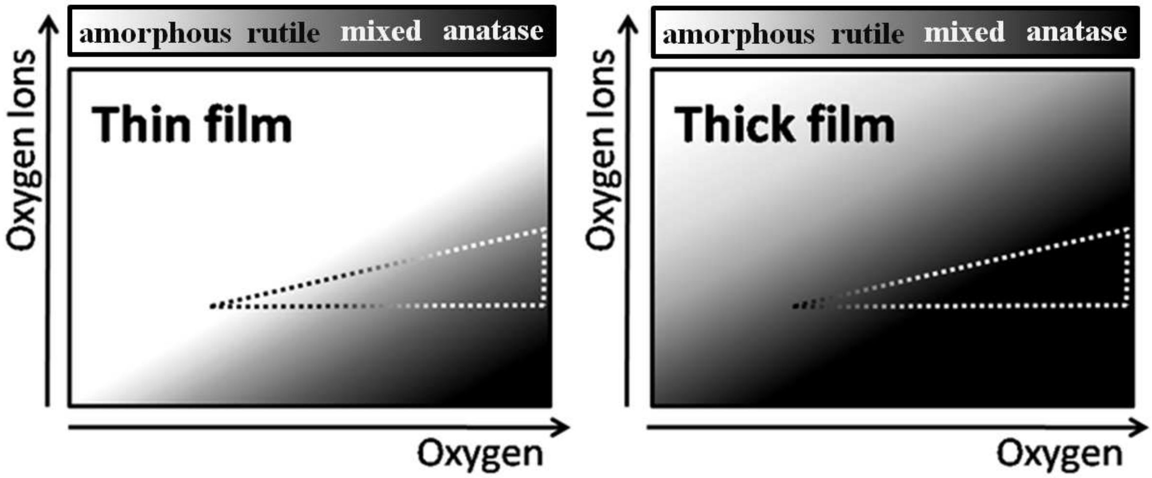

**Figure 6.20:** Change of the quality of $TiO_2$ films as a function of film thickness with increasing oxygen partial pressure and oxygen bombardment. Thin films show amorphous or mixed phases upon increasing oxygen partial pressure as well as oxygen bombardment. The anatase phase governs the structure for thicker films even at low oxygen partial pressure. This model is valid for films deposited on unheated substrate.

Moreover, the surface topography shows a clear correlation with the crystal structure (XRD scans) as presented in figure 6.21. A transition from an amorphous surface to the formation of regular arranged small rutile features with irregular larger anatase grains is observed with increasing oxygen content in the film. At higher oxygen flow, a closed surface with anatase grains is obtained. The surface structure moves in the opposite direction upon increasing the energetic bombardment.

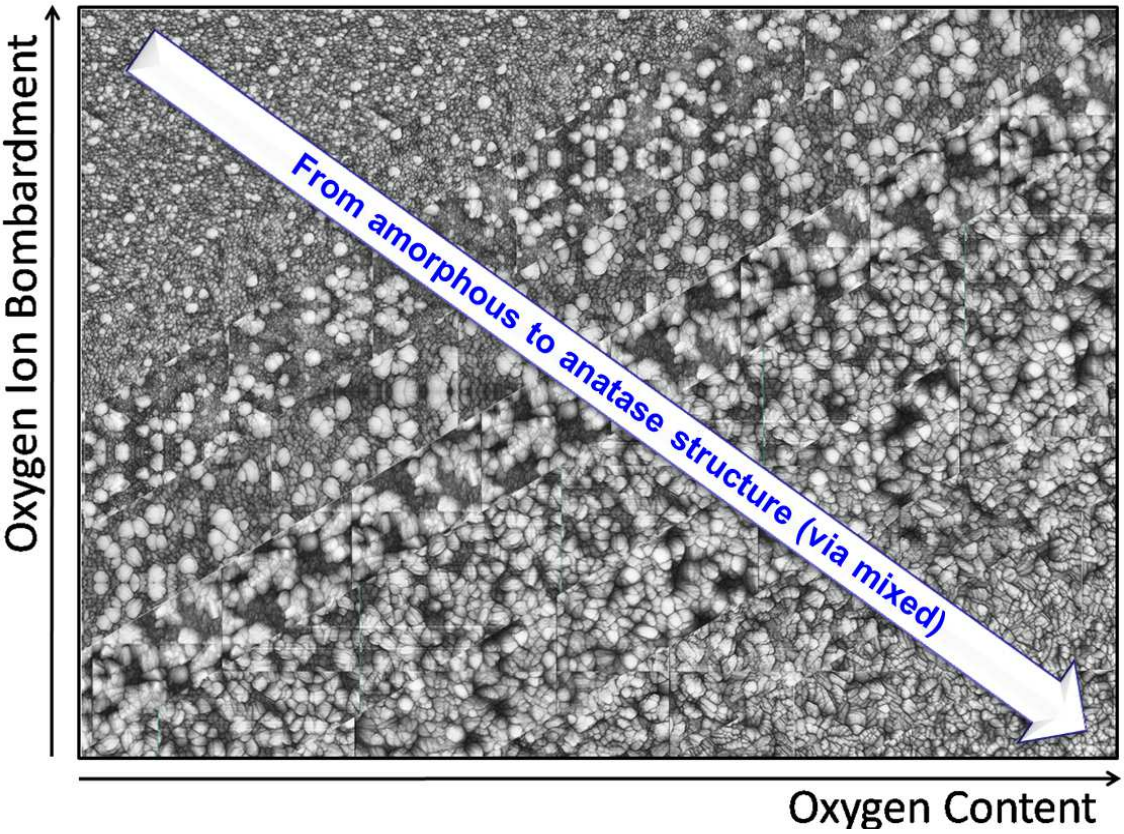

**Figure 6.21:** Schematic diagram for the variation of the structure topography of reactively sputtered $TiO_2$ films upon increasing the oxygen partial pressure (X-axis) and oxygen ion bombardment (Y-axis). The structure exhibits a transformation from an amorphous phase with small rutile features to a surface completely populated with large anatase grains upon increasing oxygen flow. The opposite behavior is formed upon high oxygen ion bombardment. The surface structure shows a clear correlation with the crystal structure (XRD patterns).

## 6.9 Discussion

The structure of reactively sputtered $TiO_2$ thin films deposited with dcMS is strongly influenced by variation of the process parameters such as oxygen partial pressure, film thickness and substrate heating:

- Oxygen partial pressure: the oxygen content in the process plays the major role in the structure formation. It leads to an improvement of the anatase structure and a transformation of the structure from amorphous to anatase via a mixed phase upon increasing the oxygen flow rate. The growth of the rutile phase is attributed to a formation of defects (O vacancies) at low pressure [136] upon employing energetic particles. These defects might be removed by applying high oxygen pressure [59] or heating [144] which leads to the formation of an anatase structure.
- Film thickness: increasing the thickness of the film improves the crystallinity of the anatase structure both at low and high oxygen partial pressure. This might be explained by a difference of grain density of the involved phases [37]. A few anatase grains are always formed even with low ion bombardment as shown from surface structure results. Due to the lower density of anatase grains (3.9 g/cm$^3$) than rutile (4.25 g/cm$^3$); the anatase grains might grow faster by shadowing and overgrowing the rutile phase. This finding is in-line with our interpretation of the surface topography. Variation of the film structure upon increasing the film thickness has been explained by increasing the substrate temperature [21]. This interpretation contradicts with the finding in [41], since they found that interrupting the deposition by cooling down the substrate for thicker films results in the same structure as without interruption.
- Small angle rocking curve scans demonstrate that the film is in-homogenous in line with the simulation of the scans. The postulated geometrical distribution of the phases assumes that the rutile phase grows at the substrate-interface with a contribution of anatase grains. At higher thickness, a complete surface of anatase is formed.
- TEM measurements show a columnar microstructure of the film. The growth of a rutile phase is always observed at the substrate-interface while a conical- shaped layer of anatase grows at the surface. With increasing thickness, the rutile phase is buried by anatase. This is consistent with XRD and AFM scans and confirms our geometrical distribution model.

- Substrate heating leads to superior anatase formation. This can be ascribed to the removal of oxygen vacancies which are created during film growth [144]. The formation of anatase is also favored at high oxygen partial pressure as shown from the buffer layer experiment.

## 6.10 Conclusions

Tailoring the composition of sputtered $TiO_2$ thin films is the motivation to establish a comprehensive understanding of the correlation between the film structure and the various process parameters. It has been found that the process parameters have a pronounced influence on the structure formation. It is evident that anatase structure is preferentially favored at higher oxygen partial pressure as well as higher film thickness. Moreover, the anatase structure profits from an absence or very weak ion bombardment. On the other hand, the formation of the rutile phase was improved by the bombardment of energetic negative oxygen ions during the film growth. The oxygen ions bombardment might be causes a generation of more oxygen vacancies during film growth which leads to a superior rutile phase formation. The preference for a rutile or an anatase film structure might simply be explained by a competition between the generation and annihilation of oxygen vacancies. Moreover, the sputtered $TiO_2$ films show a columnar microstructure with an in-homogenous distribution of anatase and rutile phases during growth. These findings have been summarized in a structure zone model which elucidates the correlation between the variation of film structure and various process parameters.

# 7

# Photoconductive properties of $TiO_2$ thin films

As presented in section 2.3.1, previous studies [53-56] have focused on the investigation of the photoconductive properties of $TiO_2$ thin films at different ambient conditions. In order to find out the correlation between the photoconductive behaviour and the structure variation, four $TiO_2$ films with different structure have been selected, figure 7.1. The films were deposited with a thickness of ≈ 220 nm at different oxygen flows of 8.5, 11, 14 and 17 sccm $O_2$, the samples are referred to as O2, O3, O5 and O7, respectively. The photoconductivity measurements have been performed by the setup which is described in section 4.7. The voltage was applied to the film and the photocurrent was recorded as the UV-light was switched on and off for periods of time between 150 and 350 seconds. The sample was heated shortly to 120°C between adjacent steps to (probably) de-trap majority of the charge carriers.

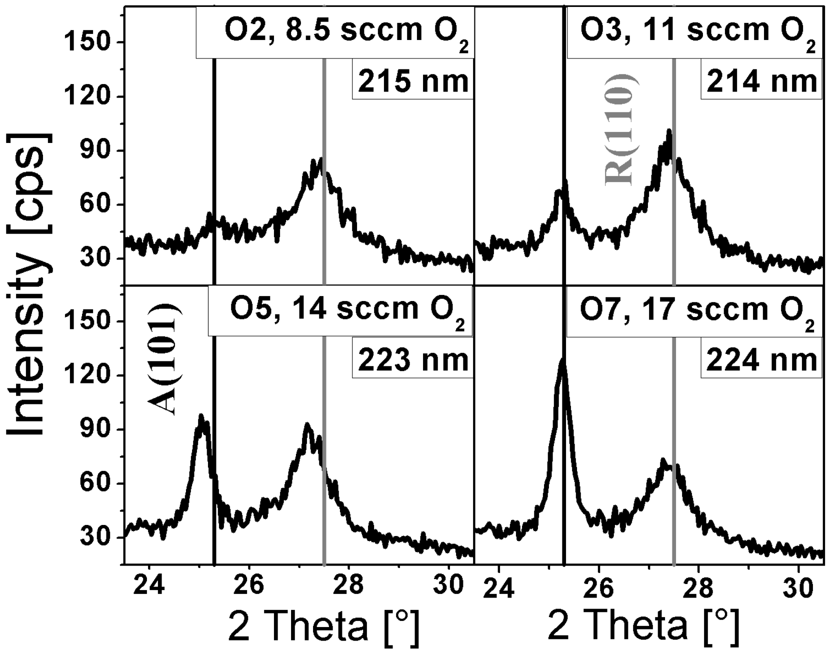

**Figure 7.1:** Grazing incidence XRD patterns of $TiO_2$ films sputtered at different oxygen partial pressure with thickness around 220 nm. The films show structure variation from pure rutile (O2) to a mixed structure with a high portion of the anatase phase (O7). These films have been selected for the photoconductivity measurements.

## 7.1. Influence of ambient atmosphere on the photoconductivity

### 1- Argon

The photocurrent was measured in argon atmosphere for the four selected $TiO_2$ films. Figure 7.2 shows as an example the sample with a high anatase fraction O7 at 45° C upon a variation of the light intensity in the range from 10 to 1. The photocurrent spectrum was recorded for two on-off illumination cycles. The photocurrent response to illumination can be explained as:

- Illumination of the film leads to a generation of $e^-$ - $h^+$ pairs and an increase of the instantaneous current. The current then increases due to the trapping of holes.
- A small amount of current is still observed as the illumination is switched off. This is ascribed to the de-trapping of charge carriers (holes).
- The photocurrent in the second cycle is attributed to the residual occupancy of traps from the first illumination [54].

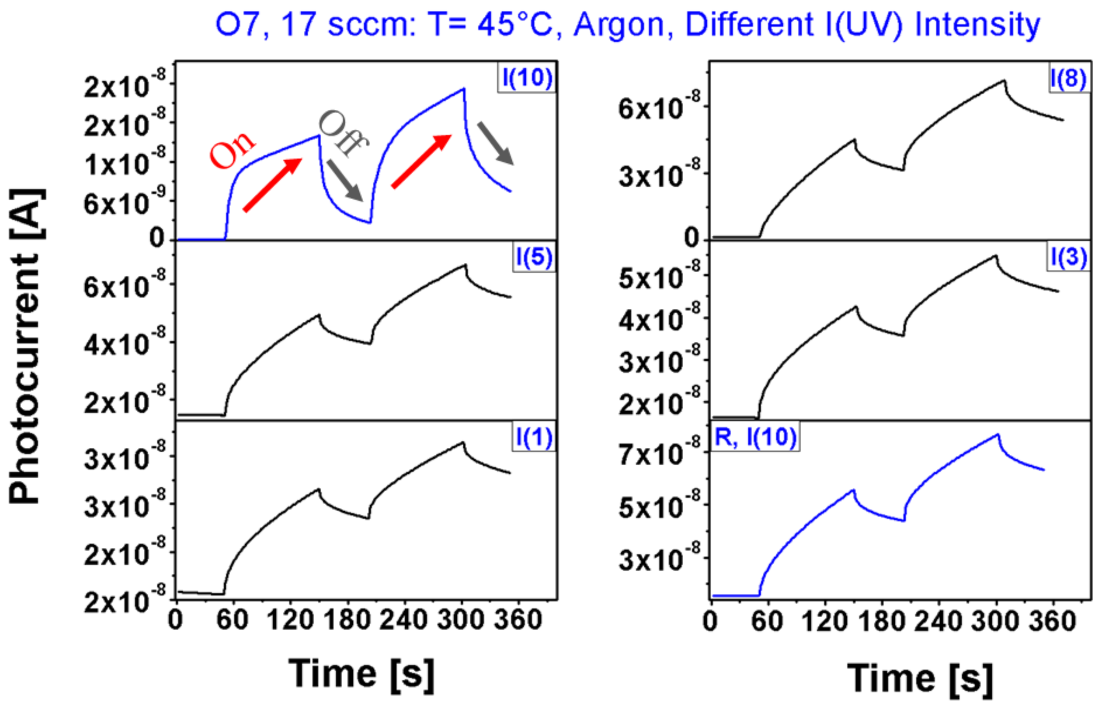

**Figure 7.2:** Variation of the photocurrent of the highly anatase film (O7) as a function of light intensity at 45° C in argon atmosphere. The photocurrent was measured for two on-off illumination cycles. Variation of the light intensity causes a dramatic change of the spectra. The measurements are also irreproducible (blue curves). Re-measuring the photocurrent at the same light intensity (10) at the end of the run shows a significant drift in the current behavior and magnitude. The origin of this drift is unclear.

It is obvious that there is a dramatic change of the photocurrent behaviour upon decreasing the light intensity from 10 to 8. The shape of the photocurrent seems to remain constant for all lower light intensities from 5 to 1. At the end, the photocurrent behaviour was re-measured for the starting light intensity 10 (blue curves) to confirm reproducibility. The second measurement shows a clear change in the current both in terms of curve shape and magnitude. The same behaviour has been observed for other films with different structure (O2, O3, O5). This might be attributed to a change of the film surface after the interaction with the light source. However, the origin of this drift is still unclear.

### 2- Air

The influence of air on the photoconductivity has also been investigated. The variation of the photocurrent at different UV light intensity for anatase sample (O7) as an example is presented in figure 7.3. All other measured films with different structure (O2, O3, O5) exhibit the same behaviour. Contrary to argon atmosphere, decreasing the light intensity leads to gradual change of the photocurrent. The photocurrent rises to maximum and then falls to steady-state value with switching on the light. The same response is produced during the consecutive periods of illumination. The photocurrent magnitude decreases with decreasing light intensity. This is explained by a low rate of photogeneration at low intensity and the slow rate of the trap filling mechanism [54]. Moreover, the drift in the measurements does not exist as observed in the case of argon atmosphere. The decay of the photocurrent with off-illumination is ascribed to electron-hole recombination mechanism [54].

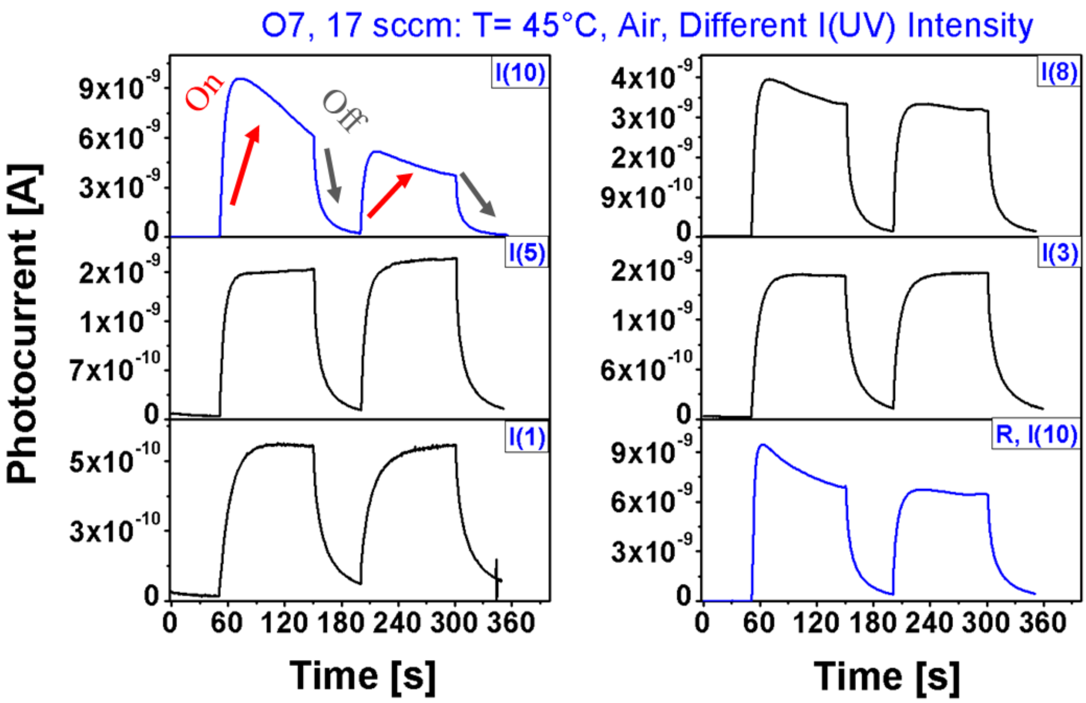

**Figure 7.3:** The photocurrent behaviour of an anatase TiO$_2$ film (O7) at different UV-light intensity at 45° C in air. The photocurrent was measured for two on-off illumination cycles. The photocurrent reaches a maximum and then falls to a steady state value upon switching on the light. This behavior is also observed in the second illumination cycle. The photocurrent magnitude decreases as the light intensity decreases. The measurement is reproducible which is observed from re-measuring the photocurrent at the same light intensity (10) at the end of the run (blue curves).

## 3- Oxygen atmosphere

To further unravel the influence of the ambient environment, the photoconductivity has been investigated in oxygen atmosphere. The photocurrent of the TiO$_2$ thin films (O2, O3, and O7) was measured as a function of the oxygen pressure in the atmosphere at 20°C and constant light intensity, as shown in figure 7.4. It has been observed that:

- The magnitude of the photocurrent decreases with increasing oxygen partial pressure in the atmosphere for all films.
- At low oxygen concentration of 1.42 l/h, switching on the light leads to an abrupt increase of the photocurrent with no saturation i.e. fast trapping rate. This is observed in rutile and mixed films (O2, and O3). On the other hand, gradual increase of the photocurrent is obtained for anatase structure (O7) i.e. slow trapping rate.

- Increasing of the oxygen concentration leads to a slow increase of the photocurrent i.e. lower trapping rate (rutile structure, O2)
- The increase and decay of the photocurrent become slower with increasing the oxygen pressure (mixed structure, O3). The saturation is attained at high concentration of oxygen (11.33 l/h).
- The steady state value and saturation of the photocurrent is reached at small oxygen concentration (highly anatase structure, O7). This indicates that the presence of an anatase phase in the structure reduces the trapping and de-trapping rates. The saturation of the photocurrent is also attained at lower light intensity and low concentration of the oxygen in the ambient atmosphere.

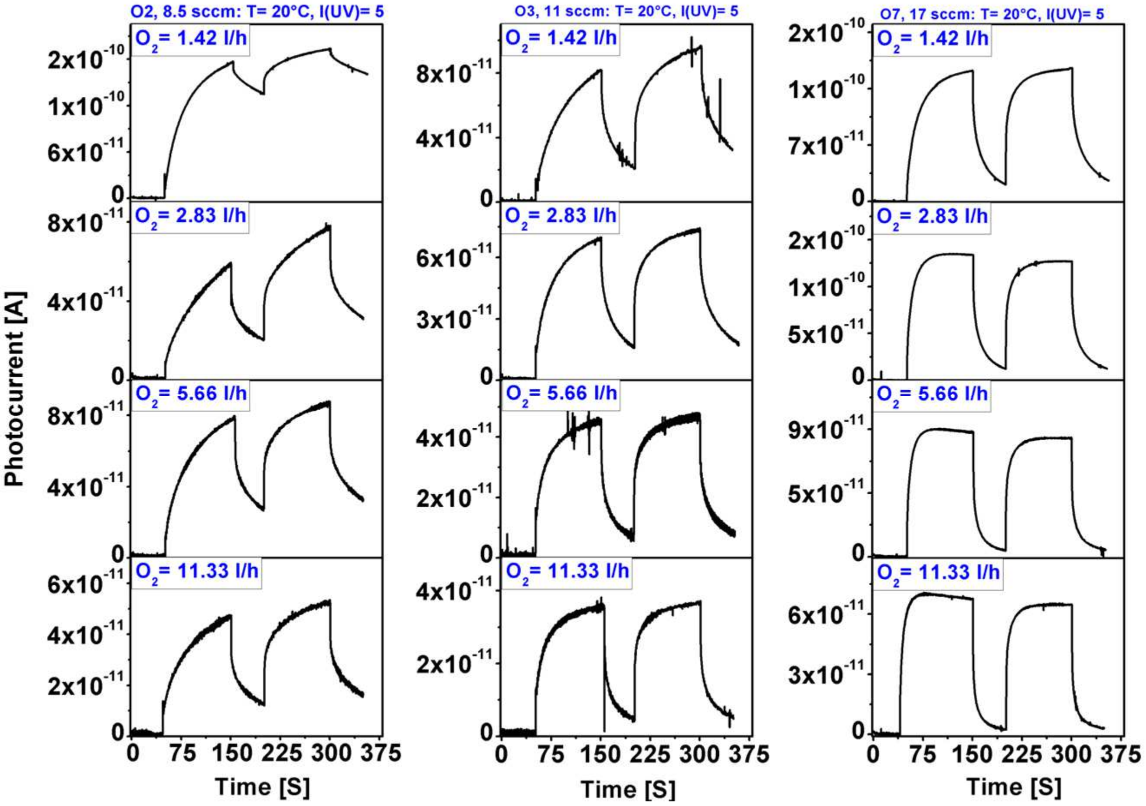

**Figure 7.4:** Change of the photocurrent of $TiO_2$ thin films (rutile O2, mixed O3, and highly anatase O7) as a function of oxygen content in the ambient atmosphere at 20° C and constant light intensity. The corresponding XRD scans for these samples are shown in figure 7.1. At low oxygen concentration, fast trapping with no saturation of the photocurrent is observed. Increasing the oxygen pressure in the ambient atmosphere reduces the trapping rate. For the anatase film (O7), the steady-state value of the photocurrent is reached at low oxygen pressure.

To summarize these results, the variation of the photoconductivity at different ambient atmospheres such as air, argon and oxygen can be attributed to the loss of surface adsorbed oxygen [53-56]. This can be observed from changing the shape and magnitude of the photocurrent in oxygen atmosphere, figure 7.4. The higher the oxygen concentration in the atmosphere, the saturation and steady-state of the photocurrent reach faster. Oxygen is known as scavenger for the photogenerated electrons; this leads to a reduction of the conduction electron density [147]. Due to the high oxygen coverage in air and oxygen as well, the removal of conduction electrons by adsorbed oxygen increases. Consequently, the electron life time is extended and the photocurrent is low. On the contrary, the low oxygen coverage in argon reduces the electron scavenger rate and thereby a large photocurrent is produced. The presence of the anatase phase in the structure improves the photoconductivity; the saturation of the photocurrent is reached at conditions of low light intensity and low concentration of oxygen in the ambient environment, as shown in figure 7.5.

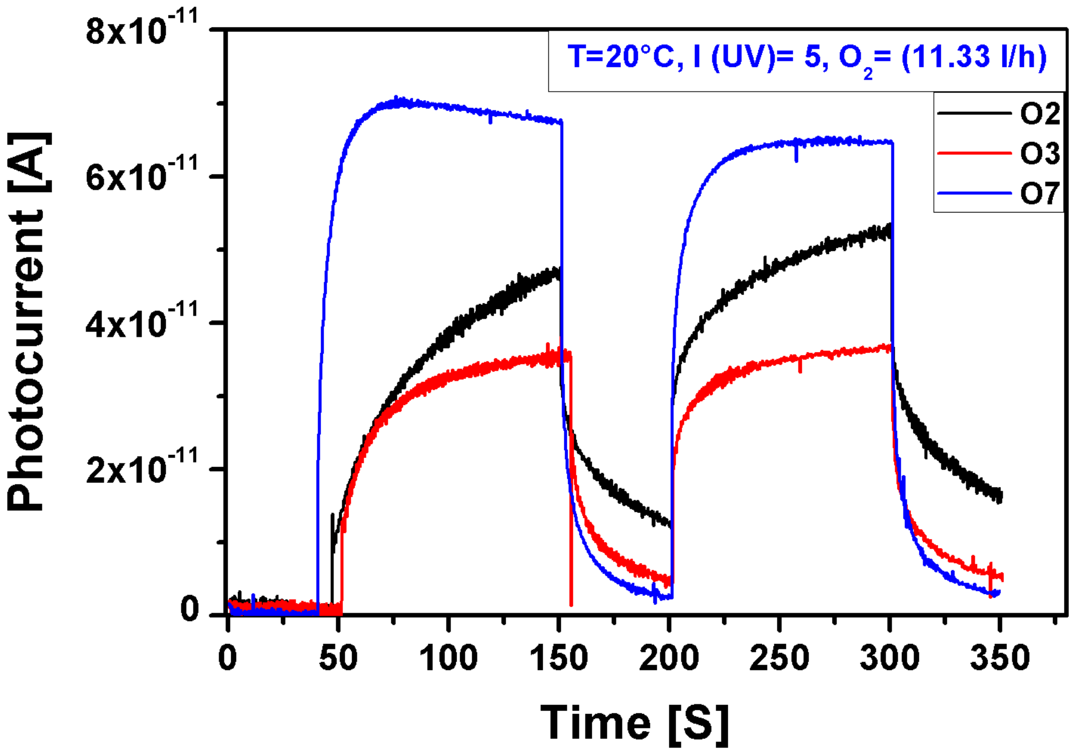

**Figure 7. 5:** The photocurrent behaviour for $TiO_2$ films (O2, O3 and O7) at temperature of 20°C, light intensity of 5 and oxygen concentration of 11.33 l/h. It is obvious that the steady-state value and saturation of the photocurrent is reached faster in the presence of anatase phase in the structure (O7). This indicates that the trapping and de-trapping rates are slower than the rutile or mixed structures.

## 7.2. Effect of temperature on the photoconductivity in oxygen atmosphere.

In order to illustrate the effect of temperature on the photoconductivity, the photocurrent of the $TiO_2$ films was measured at different temperatures of 20°C, 50°C and 80°C in oxygen atmosphere with a variation of the light intensity. Figure 7.6 (a-c) shows the photocurrent spectra of rutile (O2), mixed (O5) and anatase (O7) films.

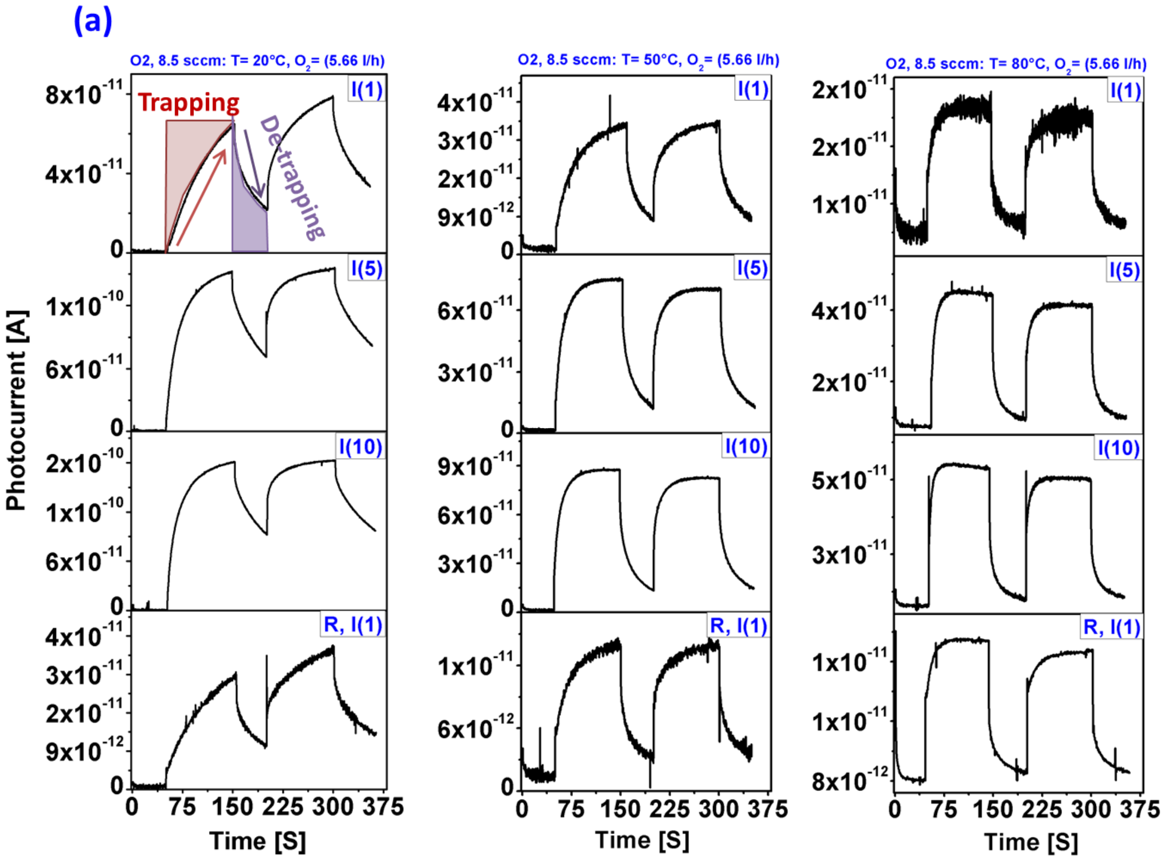

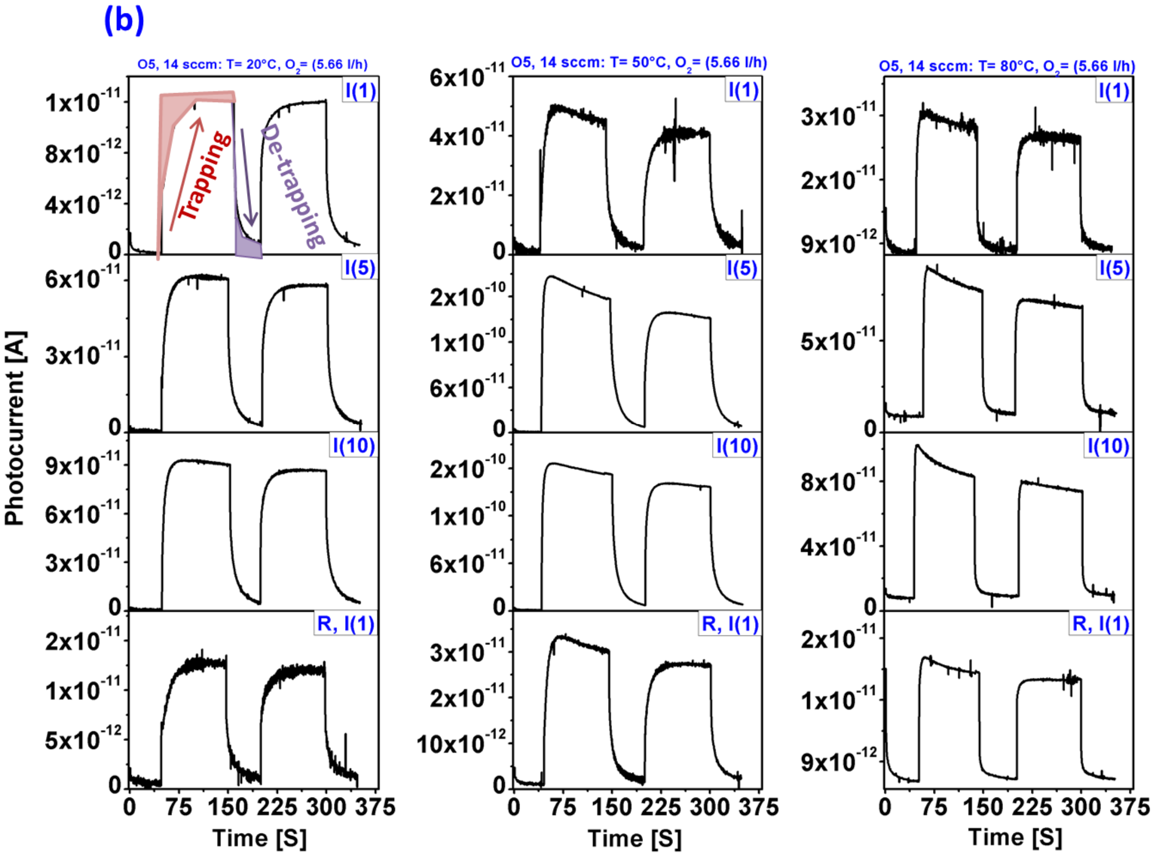
(b)
O5, 14 sccm: T= 20°C, O2= (5.66 l/h)
O5, 14 sccm: T= 50°C, O2= (5.66 l/h)
O5, 14 sccm: T= 80°C, O2= (5.66 l/h)
Trapping
De-trapping
I(1)
I(5)
I(10)
R, I(1)
Photocurrent [A]
Time [S]
0
75
150
225
300
375
1x10-11
8x10-12
4x10-12
6x10-11
3x10-11
9x10-11
2x10-11
5x10-12
4x10-11
2x10-10
1x10-10
10x10-12
9x10-12
5x10-11
8x10-11

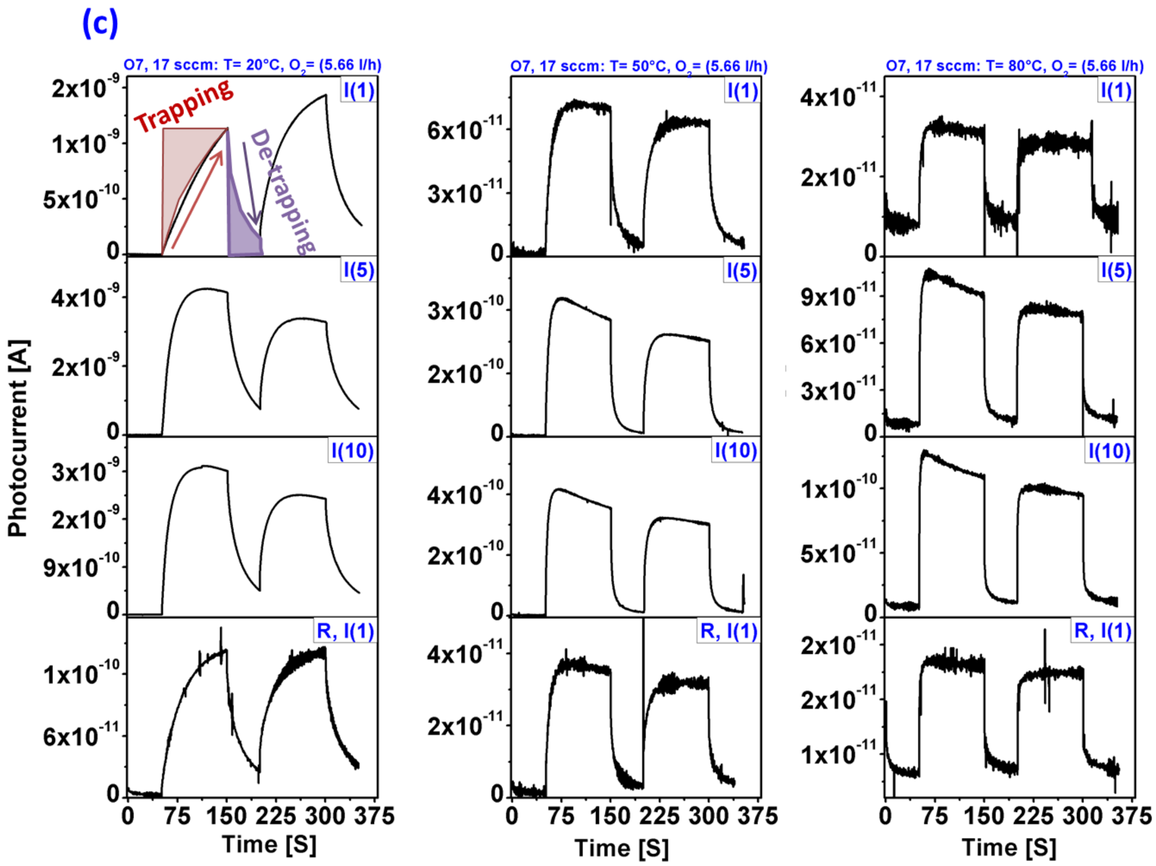

**Figure 7.6:** Variation of the photocurrent behaviour of (a) rutile (O2), (b) mixed (O5) and (c) anatase (O7) $TiO_2$ films as a function of temperatures (20°, 50° and 80°C) at different light intensities of (1, 5, 10) and an oxygen flow rate of 5.66 l/h. The magnitude of photocurrent is directly proportional to the light intensity. Increasing the temperature reduces the trapping rate and thereby a saturation of the photocurrent is obtained at low light intensity. A pronounced trapping and de-trapping is observed in the rutile structure (O2). The presence of the anatase phase in the structure reduces the trapping and de-trapping rates (O5, O7).

These measurements can be summarized as follows:

- The magnitude of the photocurrent is directly proportional to the light intensity for all films with different structures and at all temperatures.
- Increasing the temperatures affects the trapping and de-trapping speed, i.e. the saturation of the photocurrent is attained at high temperatures and the trapping rate is low. This is observed for rutile structure (O2) at 80°C, figure 7.6 a.
- Increasing the anatase contribution in the structure affects the trapping rate, i.e. the steady-state value and the saturation of the photocurrent is reached at lower temperature.

This is observed for the mixed structure (O5) at 20°C and higher light intensity of (5), figure 7.6 b. It is also exhibited by the film with predominant anatase structure (O7), figure 7.6 c.

- Figure 7.7 shows the variation of the photocurrent as a function of temperature at constant light intensity for a rutile and anatase films (O2 and O7). It is evident that the magnitude and response of the photocurrent is strongly affected by the structure variation.

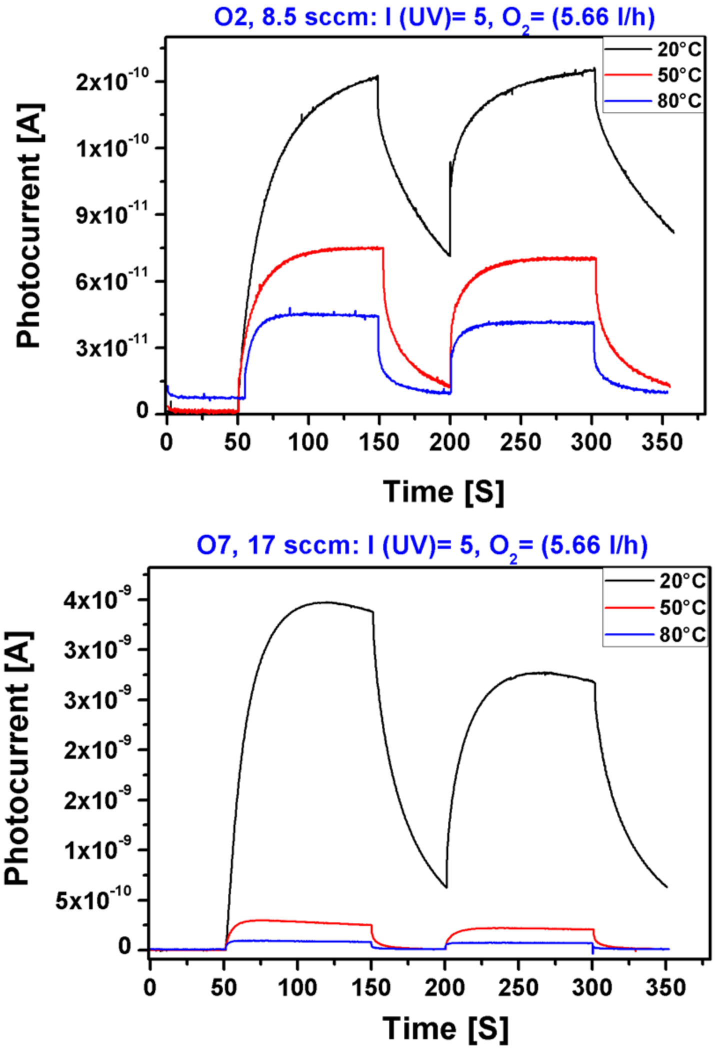

**Figure 7.7:** Variation of the photocurrent behaviour as a function of temperature at constant light intensity of rutile (O2) and anatase (O7) films. Contribution of anatase phase has a significant effect on the behavior and magnitude of the photocurrent over the temperatures range. Saturation of the photocurrent is attained at low temperatures for the anatase structure. This indicates that the trapping and de-trapping rates are slower for the rutile phase.

## 7.3 Conclusions

The photoconductive properties of $TiO_2$ thin films show a strong dependence on the different ambient atmospheres e. g argon, air and oxygen. They also exhibit a significant variation with film structure. The mechanism of the photoconductivity of $TiO_2$ thin films with different structures can be summarized as:

- Electron-hole pairs are generated as a result of an illumination of the $TiO_2$ films.
- The holes are captured by traps and the photocurrent is carried by conduction band electrons [58]. As result, the photocurrent increases in the first illumination cycle.
- The holes escape from the traps and recombine with the excess electrons upon switching off the illumination and thereby the photocurrent decays.
- The photocurrent in the second illumination cycle is attributed to the residual occupancy of traps from the first illumination [54].
- Decreasing the light intensity reduces the photogeneration rate and thereby the filling rate of trap is slow which leads to a decrease of the photoconductivity [54]
- Increasing of the photoconductivity as the temperature decreased at constant light intensity is attributed to move of the conduction electron density to higher energies [55].
- The variation of the photoconductivity with ambient atmosphere has been attributed to the loss of adsorbed oxygen [53-56]. Oxygen is known as scavenger for the photogenerated electrons; this leads to a reduction of the conduction electron density. As mentioned, a high oxygen coverage in air and in oxygen increases the removal of conduction electrons by adsorbed oxygen. As a result, the electron life time is extended and much saturation of the photocurrent is obtained. On the other hand, low oxygen coverage in argon or vacuum reduces the removal rate and thereby a large photocurrent is produced.
- It is observed that the structure variation affects the photoconductive behaviour, e.g. the trapping and de-trapping rate is faster in rutile than in anatase or mixed films. It is known that the rutile structure has a larger defect density than the anatase phase [35]. These defects are considered to be oxygen vacancies [142] which might be act as trapping centres [58]. Hence, we assume that illumination of the rutile phase leads to fast trapping of holes by these defects, while the trapping rate is slow in the anatase phase (O2 and O7), figure 7.7.
- Illumination in the presence of oxygen leads to an incorporation of oxygen into the oxygen vacancies at the surface [56]. Therefore, our assumption is that some of the

oxygen vacancies at the surface might be filled at high oxygen pressure in ambient atmosphere. Consequently, a low trapping rate is obtained. Figure 7.4, O2 and O3.

- However, understanding the photoconductive mechanism with variation of the film structure is not completely understood. Where determination the concentration of the oxygen vacancies for the different phases using the thermally simulated current (TSC) measurements is required. A clear understanding of the photoconductive behaviour as a function of the temperature is also needed.

# 8

# Summary and outlook

In this work, an atomistic understanding of the growth mechanism of $TiO_2$ thin films under the influence of various sputtering process parameters has been developed. It has demonstrated that tailoring the structure of the reactively sputtered $TiO_2$ thin films can be achieved upon controlling the sputtering process parameters. The $TiO_2$ thin films exhibit two crystalline structures i.e. anatase and rutile. The anatase phase appears to be stabilized compared to rutile, this is attributed to the lower surface energy of anatase with respect to rutile [146]. The surface free energy is the reversible work per unit area involved in forming of a new surface of substance.

Rutile has three main crystal faces. The (110) plane has the smallest surface energy in all planes of rutile (surface free energy is $\gamma_R$= 0.82 J $m^{-2}$). The anatase phase has two low energy surfaces, the majority (101) and the minority (001) in the anatase Wulff shape [146]. The anatase (101) is the most stable due to its relatively low surface free energy ($\gamma_R$= 0.52 J $m^{-2}$) in comparison to ($\gamma_R$= 0.81 J $m^{-2}$) for anatase (001) by using the generalized gradient approximations of density functional theory [148]. The (101) plane and the (110) plane are the common and the energetically preferred orientations in the anatase and the rutile phase, respectively. It has been observed from the Bragg- Brentano XRD scans of two $TiO_2$ films T1 and T2 annealed at different temperatures, figure 8.1. The as-deposited T1 exhibits an amorphous structure. An anatase phase with a strong orientation around the (101) plane is formed upon annealing in vacuum (the upper graph in figure 8.1). The as-deposited T2 shows a mixed anatase/ rutile structure. Upon annealing in air, an anatase (200) is appeared in addition to the strong (101) anatase and (110) rutile planes. The other planes such as: A (004), A (105) and A (200) in T1 and T2, respectively are thermally formed. Moreover, it has been found that rutile (110) preferentially grows when the arrival ratio of ion to atom is low upon deposition by ion beam assisted [149]. A change of preferred orientation from (110) to (200) with increase of the arrival ratio was observed with $Ne^+$ and $Xe^+$ ion bombardment during film growth. This has been explained in terms of low surface free energy of (110) orientation at low arrival ratio and ion channeling. As the arrival ratio increases, the damage caused by ion bombardment compresses the growth of crystallites with shallow ion channeling. Then

(200) preferred orientation is observed because of its deep ion channeling. Also, the rutile phase in the (110) plane grows with an increase of the $O_2^+/O^+$ ion energy from ECR ion source while the peak intensity of the other planes does not show any change[36]. This indicates that the anatase (101) plane and the rutile (110) plane are energetically preferred orientations.

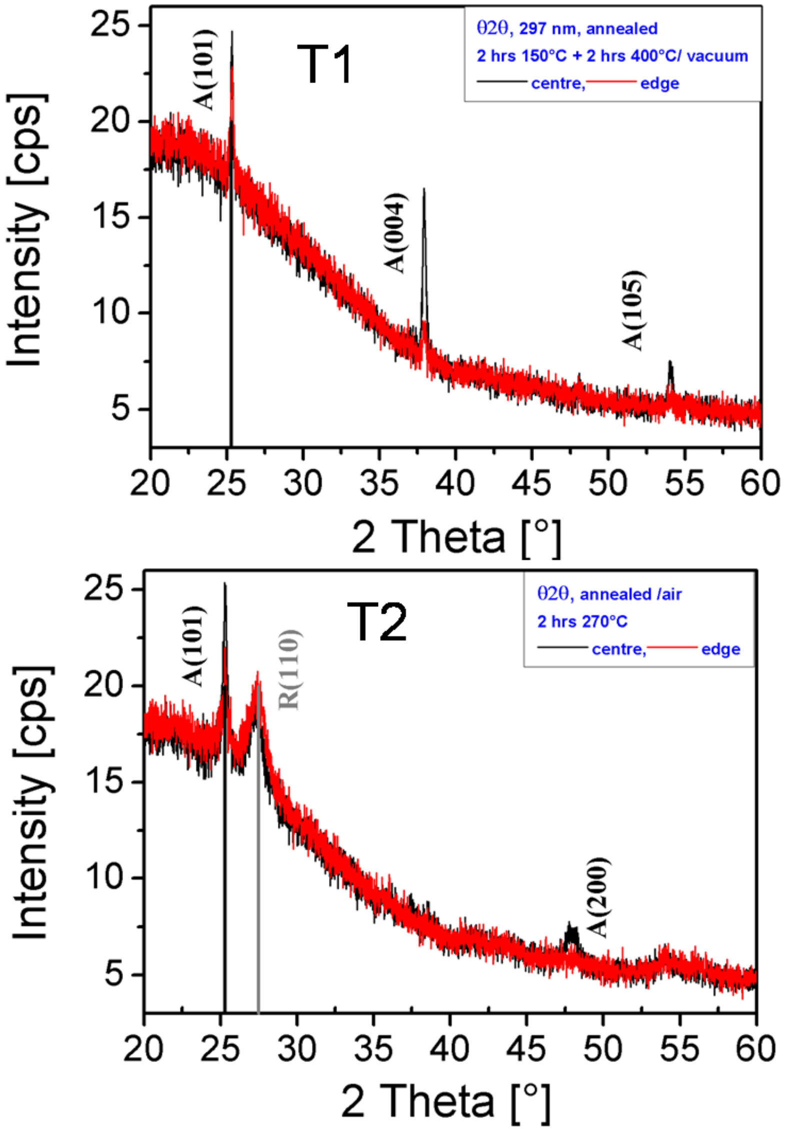

**Figure 8. 1:** Bragg-Brentano XRD scans of annealed $TiO_2$ films (T1, T2) at different temperatures. T1 shows anatase phase with a strong orientation around (101). Anatase (200) is formed in addition to the strong anatase (101) and rutile (110) reflections upon Annealing of as-deposited mixed anatase/rutile structure (T2). These scans indicate that the anatase (101) and the rutile (110) are energetically preferred orientations of both phases.

Different sputtering techniques e.g. dcMS, IBAS and HiPIMS have been utilized to fabricate titanium dioxide thin films. The investigations have been performed as a function of different parameters such as energetic bombardment, oxygen partial pressure and film thickness. It has been found that the formation of each phase is governed by specific parameters. For instance, energetic bombardment promotes the growth of the rutile structure. On the other hand, the growth of the anatase phase profits from absence or very weak bombardment. Additionally, the anatase phase was preferentially favoured at higher oxygen partial pressure as well as higher film thickness. The substrate heating has led to superior anatase formation.

In chapter 5, it has been demonstrated that the energetic bombardment plays a dominant role in the structure formation. It has been proven that the bombardment of the growing film by highly energetic negative oxygen ions inherent in the sputtering process promotes the growth of the rutile structure. This has been observed by an investigation of the sample profile utilizing new and aged targets, since the distribution of oxygen ion bombardment along the substrate depends on the age of the target. This is supported from measurements of the growth in a HiPIMS process, where the negative oxygen ions with high energies are the dominant species that govern the structure formation. Moreover, pure rutile films have been grown under additional ion bombardment by ion-assisted sputtering at low ion energy. Higher energies have led to the deterioration of the rutile structure. These results also show that the ion bombardment selectively hindered the formation of the anatase phase. The investigation of the structure under the influence of $O^+$ ion and $Xe^+$ ion bombardment has indicated that the nature of the bombarding species does not play a role in determining the film structure. On the contrary, reducing the intensity of the energetic oxygen ion bombardment from the sputter target has enabled the formation of pure anatase structure. It has also been shown that the ion bombardment has a strong influence on the surface topography. Two surface features can be clearly distinguished. Type 1 topography could be described as a regular arrangement of small-grained features which were assigned to rutile grains. Irregular large features (type 2) were referred to as anatase grains. It has also demonstrated that the pure rutile structure grown in the HiPIMS process is thermally stable. The impact of highly energetic oxygen ions to the growing film has led to generation of compressive stress which is dependent on the various process parameters.

The crystal structure as well as the surface topography has been investigated upon variation of the oxygen partial pressure and the film thickness. It has been shown that the anatase phase is preferentially formed at high oxygen flow and at higher film thickness as well. The rutile phase is observed at low oxygen pressure. The surface topography has shown a good correlation with the crystal structure. At high oxygen partial pressure and at high film thickness, the anatase features (type 2) are completely governed the surface structure. The film shows an inhomogeneous distribution of the rutile and anatase phases upon increasing the film thickness. The small angle rocking curve scans have shown that the rutile grows at the substrate interface with a contribution of anatase grains. At high thickness, the anatase phase has overgrown rutile phase and hence governs the structure. This has been confirmed by a simulation of the rocking curve scans for different film structures. Furthermore, TEM measurements have confirmed our postulated model about the structure distribution. The measurements show that the growth of rutile is always observed at the substrate interface with a conical- shape layer of anatase at the surface.

The nucleation of rutile by energetic bombardment was explained by the fact that rutile is the high-energy phase of $TiO_2$. It has been attributed to the existence of oxygen defects at low oxygen partial pressure. On the other hand, nucleation of anatase might be attributed to repair of these defects at high oxygen pressures or by heating. Overgrowth of anatase at high thickness was explained by the lower density of anatase grains than rutile. A structure zone model was established to describe the structure variation of $TiO_2$ thin films under the influence of various process parameters. The nucleation mechanism of anatase and rutile grains can be expressed in term of energetic bombardment as follows:

1- Low energy bombardment promotes the formation of nucleation sites for crystal formation as appeared from the AFM scans at low oxygen flow.

2- Intermediate energy bombardment causes the formation of mixed anatase and rutile. The anatase grains win the competition with the rutile grains due to its lower density as observed from the film thickness results.

3- High energy bombardment: the rutile phase governs the nucleation mechanism as shown from the $O^+$ and $Xe^+$ ions results; this might be due to the formation of high defect densities.

Investigations of the photoconductive properties of $TiO_2$ thin films at different ambient atmospheres have shown significant variations with film structure. It has been demonstrated that the trapping and de-trapping rates are slower for the anatase structure than the rutile phase.

However, the mechanism of the photoconductivity as a function of the film structure has not been completely understood. Determination the concentration of the oxygen vacancies for the different phases from the thermally simulated current (TSC) measurements is required. The presence of the oxygen vacancies can also be observed from the photoluminescence spectra. Therefore, it is required to perform these measurements for the different $TiO_2$ film structures. The role of the temperature on the photoconductive behaviour is not completely clear. In order to figure out the correlation between the photo-induced properties and the structure, the forthcoming experiments in further works on $TiO_2$ should focus on the investigations of the photo-induced properties e.g., the photoconductivity, photoluminescence and the work function at different film structures. In addition, building a model describing the variation of these properties with film structure should also be targeted.

# Bibliography

[1] Mattox D M 1998 Handbook of physical vapor deposition (PVD) processing, Noyes publications Westwood.

[2] Moshfegh A Z et al. 2004 Physics and technology of thin films, World Scientific, Singapore.

[3] Fujishima A, Honda K 1972 Nature ***238*** 37.

[4] Graetzel M, 1991Comment. Inorg. Chem.***12*** 93.

[5] Suhail M H, Mohan Rao G, Mohan S 1992 J. Appl. Phy. ***71*** (3) 1421.

[6] Perry A J, Pulker H K 1985 Thin Solid Films ***124*** 323

[7] Natsuhara H, Matsumoto K, Yoshido M, Sato K, Nonomura S, Fukawa M, Sato K 2006 Sol. Energy Mater. Sol. Cells ***90*** 2867-80.

[8] Wiggnis M D, Nelson M C and Aita C R, 1996 J. Vac. Sci. Technol. ***A 14*** 772.

[9] CRC Handbook of Chemistry and Physics, 78th edn., CRC Press, Boca Raton, NY, p. 4-132, 137.

[10] Richards B S, 2004 Prog. Photovolt: Res. Appl. ***12*** 253-281

[11] Jeong S-H, Kim, J-K, Kim B-S, Shim S-H and Lee B-T ***2004*** Vacuum 76 507.

[12] Battaglin C, Caccavale F, Menelle A, Montecchi M, Nichelatti E, Nicoletti F and Polato P 1999 Thin Solid Films ***351*** 176.

[13] Fujishima A, Rao T N and Tryk D A 2000 Journal of Photochemistry and Photobiology C: Photochemistry Reviews ***1*** 1-21.

[14] Fujishima A, Zhang X, and Tryk D A 2008 Surface Science Reports ***63*** 515-82

[15] Hashimoto K, Irie H and Fujishima A 2005 Jap. J. Appl. Phys. ***44***(12) 8269.

[16] Ahn Y U, Kim E J, Kim H T and Hahn S H 2003 Materials Letters ***57***, 4660-4666

[17] Battiston G A, Gerbasi R, Porchia M and Marigo A 1994 Thin Solid Films ***239***, 186

[18] Mergel D, Buschendorf U D, Eggert S, Grammes R and Samset B 2000 Thin Solid Films ***371***, 218-224

[19] Li C, Zheng Z, Zhang F, Yang S, Wang H, Chen L, Zhang F, Wang X and Liu X 2000 Nucl. Instr. and Methods in Phys. Res. B ***169*** 21-25

[20] Gilo M and Croitoru N 1996 Thin Solid Films ***283*** 84-89

[21] Musil J, Herman D and Sicha J 2006 J. Vac. Sci. Technol. ***A 24***(3) 521

[22] Zeman P and Takabayashi S 2002 J. Vac. Sci. Technol. ***A 20***(2) 388.

[23] Musil J, Sicha J, Herman D and Cerstvy R 2007 J. Vac. Sci. Technol. *A* ***25*** 666

[24] Zeman P and Takabayashi S 2002 Surf. Coat. Technol.***153*** 93–9

[25] Zeman P and Takabayashi S 2003 Thin Solid Films ***433*** 57–62

[26] Kuzel R, Nichtova L, Herman D, Sicha J and Musil J 2007 Z. Kristallogr. Suppl. ***26*** 241

[27] Kuzel R, Nichtova L, Matej Z, Sicha J and Musil J 2008 Z. Kristallogr. Suppl. ***27*** 287–94

[28] Yamagishi M, Kuriki S, Song P K and Shigesato Y 2003 Thin Solid Films ***442*** 227–31

[29] Song P K, Irie Y, Ohno S, Sato Y and Shigesato Y 2004 Japan. J. Appl. Phys. ***43*** L442–5

[30] Song P K, Irie Y, Sato Y and Shigesato Y 2004 Japan. J. Appl.Phys. ***43*** L358–61

[31] Okimura K 2001 Surf. Coat. Technol. ***135*** 286–90

[32] Leprince-Wang Y, Souche D, Yu-Zhang K, Fisson S, Vuye G and Rivory J 2000 Thin Solid Films ***359*** 171-176

[33] Miyata T, Tsukada S and Minami T 2006 Thin Solid Films ***496*** 136-140

[34] Martin N, Santo A M E, Sanjines R and Levy F 2001 Surf. Coat. Technol. ***138*** 77–83

[35] Zywitzki O, Modes T, Sahm H, Frach P, Goedicke K and Glöß D 2004 Surf. Coat. Technol. ***180–181*** 538–43

[36] Miyake S, Honda K, Kohno T, Setsuhara Y, Satou M and Chayahara A 1992 J. Vac. Sci. Technol. ***A 10***(5) 3253

[37] Löbl P, Huppertz M and Mergel D 1994 Thin Solid Films ***251*** 72–9

[38] Stranak V et al 2009 J. Phys. D: Appl. Phys. ***42*** 105204

[39] Linsebigler A L, Lu G, and Yates J T 1995 Chem. Rev. ***95*** (3) 735.

[40]Hoffmann M R, Martin S T, Choi W and Bahnemann D W 1995 Chem. Rev. ***95*** 69.

[41] Sicha J, Musil J, Meissner M and Cerstvy R 2008 Applied Surface Science ***254*** 3793

[42] Kuzel R, Nichtova L, Matej Z, Herman D, Sicha J and Musil J 2007 Z. Kristallogr. Suppl. ***26*** 247–252

[43] Sicha J, Hermann D, Musil J, Stryhal Z 2007 Nanoscale Res Lett ***2*** 123-129

[44] Meng L-J, Andritschky M, Santos M P 1993 Thin Solid Films ***223*** 242-247

[45] Takeda S, Suzuki S, Odaka H and Hosono H 2001 Thin Solid Films ***392*** 338–44

[46] Stranak V et al 2008 J. Phys. D: Appl. Phys. ***41*** 055202

[47] Konstantinids S, Dauchot J P, Hecq M 2006 Thin Solid Films ***515*** 1182-86

[48] Mráz S and Schneider J M 2006 J. Appl. Phys. ***100*** 023503.

[49] Ngaruiya J M, Kappertz O, Mohamed S H and Wuttig M 2004 Appl. Phys. Lett**.** ***85*** (5) 748.

[50] Severin D, Kappertz O, Nyberg T, Berg S and Wuttig M 2007 Thin Solid Films ***515*** 3554.

[51] Wang T M, Zheng S K, Hao W C, Wang C 2002 Surf. Coat. Technol. ***155*** 141-145.

[52] Masahiko Maeda, Teruyoshi Watanabe 2007 Surf. Coat. Technol. ***201*** 9309-9312

[53] Brajsa A, Szaniawska K, Barczynski R J, Murawski L, Koscielska B, Vomvas A, Pomoni K 2004 Optical Materials ***26*** 151-153.

[54] Eppler A M, Ballard I M, Nelson J 2002 Physica E ***14*** 197-202

[55] Golego N, Studenikin S A, Michael Cocivera 2000 Physical Review B 61, N ***12*** 8262

[56] Golego N, Studenikin S A and Cocivera M 2000 J. of Electrochemical Society ***147*** (4) 1592-1594

[57] Golego N, Studenikin S A Michael Cocivera 1999 J. Mater. Res. ***14***, N 3 698-707

[58] Studenikin S A, Golego N, Cocivera M 1998 J. Appl. Phys. ***84*** (9) 5001-4

[59] Takeuchi M 1979 Phys. Stat. Sol. (a) ***55*** 653-658

[60] www.pvd-coatings.co.uk/theory-of-pvd-coatings-magnetron-sputtering.htm

[61] Peter Sigmund 1969 Physical Review ***184*** (2) 383-416.

[62] Thornton J A 1975 SAE Trans. ***82*** 1787.

[63] Keller J H and Simmons R G, 1979 IBM J. Res. Dev. ***23*** 24.

[64] Hosokawa N, 1979 Japan J. Appl. Phys. ***18*** 889.

[65] Chen F F 1974 Introduction to Plasma Physics and Controlled Fusion: Plasma physics, Plenum press.

[66] Braithwaite N S J 2000 Plasma Sources Sci. Technol. ***9*** 517–527

[67] Ohring M 1992 The Material Science of Thin Films, Academic Press.

[68] Venkataraj S, Kappertz O, Weis H, Drese R, Ravayel R, and Wuttig M 2002 J. Appl. Phys. ***92*** 3599.

[69] Musil J, Baroch P, Vlcek J, Nam K H, and Ham J G 2005 Thin Solid Films ***475*** 208.

[70] Berg S, Nyberg T 2005 Thin Solid Films ***476*** 215.

[71] Matsuda Y, Otomo K, and Fujiyama H 2001 Thin Solid Films ***390*** 59.

[72] Berg S, Blom H-O, Larsson T and Neder C 1987 J. Vac. Sci. Technol. ***A5*** (2) 202.

[73] Depla D, Heirwegh S, Mahieu S, Haemers J, De Gryse R 2007 J. Appl. Phys. ***101*** 013301-1.

[74] Depla D, De Gryse R 2003 Surf. Coat. Technol. ***183*** (2-3) 184.

[75] Kouznetsov V, Macák K, Schneider J M, Helmersson U, and Petrov I 1999 Surf. Coat Technol. ***122*** 290.

[76] Alami J, Persson P O A, Böhlmark J, Gudmundsson J T, Music D, and Helmersson U 2005 J. Vac. Sci. Technol. A ***23*** 278.

[77] Glocker D A, Romach M M, Christie D J, and Sproul W D 2004 47th Annual Technical Conference Proceedings of the Society of Vacuum Coaters 183.

[78] Ehiasarian A P, Hovsepian P Eh, Hultman L, and Helmersson U 2004 Thin Solid Films ***457*** 270

[79] Christie D J 2005 J. Vac. Sci. Technol. A ***23*** 330

[80]Sarakinos K, Alami J, Konstantindis S 2009 Surf. Coat. Technol. ***201*** (11) 1661.

[81] Michely T and Krug J 2004 Islands Mounds and Atoms, Springer

[82] Bauer E 1958 Z. Kristallogr. ***110*** 372.

[83] Royer L 1982 Bull. Soc. Fr. Min. ***51*** 7

[84] Ensinger W 1997 Nucl. Instrum. Methods Phys. Res. B ***127/128*** 796.

[85] Chopra K L 1969 Thin Film Phenomena, McGraw - Hill.

[86] Movchan B A, Demchishin A V 1969 Phys. Met. Metallogr. ***28*** 83.

[87] Thornton J A 1974 J. Vac. Sci. Technol. ***11*** 666.

[88] Thornton J A 1975 J. Vac. Sci. Technol. ***12*** 830.

[89] Barna P B, Adamik M 1998 Thin Solid Films ***317*** 27

[90] Köhl D 2006 Der Einfluß von Ionenbeschuß auf Filmeigenschaften beim reaktiven DC-Magnetron-Sputtern, Diplom thesis, RWTH -Aachen

[91] Thornton J A 1986 J. Vac. Sci. technol. A***4*** (6) 3059.

[92] Messier R, Giri A P and Roy R A 1984 J. Vac. Sci. Technol. A***2*** (2) 500.

[93] Tominaga K, Iwamura S, Shintani Y and Tada O 1982 Jap. J. Appl. Phys. ***21*** 688.

[94] Tominaga K, Iwamura S, Shintani Y and Tada O 1982 Jap. J. Appl. Phys. ***21*** 999.

[95] Koch R 1994 J. Phys.: Condense. Matter ***6*** 9519.

[96] Windischmann H 1992 Critical Reviews in Solid State and Materials Sciences ***17*** (6) 547.

[97] D’Heurle F M , Harper J M E 1989 Thin Solid Films ***171*** 81.

[98] Windischmann H 1987 J. Appl. Phys. ***62*** (5) 1800.

[99] Müller K-H 1987 J. Appl. Phys. ***62*** (5) 1796.

[100] Davis C A 1993 Thin solid films ***226*** 30.

[101] Stollenwerk J 1993 Reaktives Sputtern von Oxidfilmen- Herstellung dielektrischer dünner Schichten für technische Anwendungen, Dissertation, RWTH- Aachen, Aachen

[102] Tectra GmbH, www.tectra.de

[103] Bragg W L 1913 "The Diffraction of Short Electromagnetic Waves by a Crystal", Proceedings of the Cambridge Philosophical Society ***17*** 43–57.

[104] Cullity B D 1978 “Element of X-ray Diffraction” 2nd edn, Addison-Wesley publishing company

[105] www.unl.edu/CMRAcfem/temoptic.htm

[106] Azzam A and Bashara N M 1977 Ellipsometry and Polarized Light, North –Holland

[107] http://las.perkinelmer.de/

[108] O’Leary S K, Johnson S R and Lim P K, J. Appl. Phys. ***82*** **(**1997) 3334

[109]W. Thesis 2007 Hard- and Software for Optical Spectroscopy www.wtheiss.com.

[110] Stoney G G, Proc. Roy. Soc. London A ***82*** (1909) 172.

[111] Robert Drese, Thesis, RWTH- Aachen (2005).

[112] Yu Z, Steven S C Chuang 2007 Journal of Catalysis ***246*** 118-126.

[113] Zhang W, Li Y, Zhu S, Wang F 2004 Surf. Coat. Technol. ***182*** 192-198.

[114] Wallin E, Helmersson U, 2008 Thin Solid Films ***516*** 6398-6401.

[115] Sarakinos K, Alami J, Wuttig M 2007 J. Phys. D: Appl. Phys. ***40*** 2108-2114

[116] Severin D, Sarakinos K, Kappertz O, Pflug A and Wuttig M 2008 *J. Appl. Phys.* ***103*** 083306

[117] Mráz S and Schneider J M 2006 Appl. Phys. Lett. ***89*** 051502

[118] Richter F, Welzel T, Kleinhempel R, Dunger T, Knoth T, Dimer M and Milde F 2009 Surf. Coat. Technol. ***204*** 845–9

[119] Fukushima K and Yamada I 1989 J. Appl. Phys**.** ***65***(2) 619–23

[120] Fukushima K and Yamada I 1989 Appl. Surf. Sci**.** ***43*** 32–6

[121] Leprince-Wang Y, Yu-Zhang K, Nguyen Van V, Souche D and Rivory J 1997 Thin Solid Films ***307*** 38–42

[122] Alami J, Sarakinos K, Uslu F, Klever C, Dukwen J and Wuttig M 2009 *J.* Phys. D: Appl. Phys. ***42*** 115204

[123] Tucek J C, Walton S G and Champion R L 1998 Surf. Sci. ***410*** 258

[124] Mahieu S and Depla D 2007 Appl. Phys. Lett. ***90*** 121117

[125] Misina M, Bradley J W, B¨acker H, Aranda-Gonzalvo Y, Karkari S K and Forder D 2003 Vacuum ***68*** 171–81

[126] Drese R J and Wuttig M 2006 J. Appl. Phys. ***99*** 123517

[127] Glöß D, Frach P, Zywitzki O, Modes T, Klinkenberg S and Gottfried C 2005 Surface & Coatings Technol. ***200*** 967-971

[128] Sarakinos K, Alami J, Dukwen J, Woerdenweber J and Wuttig M 2008 J. Phys. D: Appl. Phys. ***41*** 215301

[129] Alami J, Sarakinos K, Mark G and Wuttig M 2006 Appl. Phys. Lett. ***89*** 154104

[130] Bendavid A, Martin P J, Takikawa H 2000 Thin Solid Films ***360*** 241-249

[131] Ottermann C R, Bange K 1996 Thin Solid Films ***286*** 32- 34

[132] Ben Amor S, Baud G; Besse J P, Jacquet M 1997 Thin Solid Films ***293*** 163-169

[133] Thornton J A 1977 J. Vac. Sci. Technol. ***14*** (1) 164-168

[134] Bull S J 1992 Vacuum ***43*** 387-391

[135] Drese R J, Wuttig M 2005 J. Appl. Phys. ***98*** 073514.

[136] Okimura K, Shibata A 1997 Jpn. J. Appl. Phy***.*** ***36*** 313.

[137] Okimura K, shibata A, Maeda N, Tachibana K, Noguchi Y, Tsuchida K 1995 Jpn. J. Appl. Phys. ***34*** 4950.

[138] Dominik Köhl, RWTH-Aachen, personal communication.

[139] Spurr R A, Myers H (1957) Anal. Chem. ***29*** 760-762

[140] Lei Miao, Tanemura S, Jin P , Kaneko K, Terai A, Nabatova- Gabain N 2003 J. Cryst. Growth ***254*** 100-106.

[141] Le Chen, Graham M E, Li G, Gray K A 2006 Thin Solid Films ***515*** 1176-1181.

[142] Fischer S, Schierbaum K-D, Ggpel W 1997 Vacuum ***48*** (7-9) 601- 605

[143] Mayer J T, DieboldU, Madey T E, Garfunkel E 1995 J. Electron. Spectrosc. Relat. Phenom. ***73*** 1-11

[144] Tomaszewski H, Poelman H, Depla D, Poelman D, De Gryse R, Fiermans L, Reyniers M-F, Heynderickx G, Marin G B 2003 Vacuum ***68*** 31-38

[145] Iijima K, Goto M, Enomoto S, Kunugita H, Ema K, Tsukamoto M, Ichikawa N, Sakama H 2008 J. Lumin ***128*** 911-13.

[146] Cheng H, Selloni 2009 Phys Rev B. ***79*** 092101

[147] Weidmann J et al. 1999 Sol. Energy Mater. Sol. Cells ***56*** 153

[148] Vittandini A, Selloni A, Rotzingen F P, Gratzel M 1998 Phy. Rev. Lett. ***81*** 2954-57

[149] Feng Z, Zhihong Z, Yu C, Duo L, Xianghuai L 1998 J. Appl. Phys. ***83*** (8) 4101-05

# List of Figures

# List of figures

# Lebenslauf

## *Persönliche:*

**Name:** Azza Tantawy Amin El-Hamshary
**Date of Birth:** 21. September 1975
**Place of Birth:** El-Gharbia, Egypt
**Nationality**: Egyptian
**Marital status:** Single
**Mail:** aamin@st.tu-darmstadt.de

## *Academic Qualifications*

| | | | |
|---|---|---|---|
| 1993 | High school | Cairo, Egypt | |
| 1993-1997 | Bachelor of Science (Physics) | Ain Shams University, Cairo, Egypt | very good |
| 2000-2006 | Master of Science, (Solid state physics)<br>*Title of thesis:*<br>“Preparation and study of some physical properties of $Pb_XSn_{1-x}Se_Y Te_{1-y}$ semiconducting compounds” | Ain Shams University, Cairo, Egypt | |
| 2007-2011 | Ph. D study in Physics<br>*Title of thesis:*<br>“Influence of reactive sputtering process parameters on the structure and properties of $TiO_2$ thin films | RWTH Aachen, Germany | good |

## *Publications*

1. E. A. El-Sayad, B. S. Farag, I. S. Farag and **A. T. Amin**, J. Phys. D: Appl. Phys. 40 (2007) 5313–5318, “Structural and optical absorption studies on polycrystalline $Pb_xSn_{1-x}Te_{0.5}Se_{0.5}$ thin films”.
2. E. A. El-Sayad, B. S. Farag, **A. T. Amin**, Vacuum 84 (2010) 807–811, “Electrical properties of crystalline $Pb_xSn_{1\_x}Te_{0.5}Se_{0.5}$ thin films”.
3. **A. Amin**, D. Köhl and M. Wuttig, “The role of energetic ion bombardment during growth of $TiO_2$ thin films by reactive sputtering” Journal Phys D: Appl. Phys, 43 (2010), 405303.

# ACKNOWLEDGEMENT

*I kneel humbly to God thanking HIM for showing me the right path, without his help my efforts would have gone astray.*

*First of all, I wish to express my deep gratitude and thanks to my advisor* ***Prof. Dr. Matthias Wuttig*** *for the fact that he gave me the opportunity to work in his group and for several encouraging discussions and suggestions which gave me direction and inspiration.*

*I would like to thank the* ***Egyptian Government*** *for the financial support of my scholarship to carry out this work at the I. Physikalisches Institut der RWTH Aachen, Germany.*

*I would like also to express my sincere thanks to* ***Prof. Dr. Dieter Mergel*** *(Uni. ESSEN-Duisburg) for being the second referee of my thesis and preparation of the valuable report on my work.*

*Deep appreciation and thanks is felt to* ***Dr. Dominik Köhl*** *for his help, fruitful discussions and guidance throughout the work. I consider myself extraordinarily fortunate to have had the opportunity to work closely to him. I benefited extensively from his enormous physical insight and scientific experience.*

*I would like to thank my officemates* ***Janika Boltz*** *and* ***Dr. Gomathi Natarajan****, also the sputter group members for the time that we spent and the nice discussions. I would like also to express my thanks to* ***Dr. Jenni Karvonen*** *for her help and advice. I wish to thank all my colleagues at the institute for the nice time and help.*

*Apart from scientific issues, my sincere thanks to* ***Mrs. Josefine Elbert*** *who was always available and helpful regarding the treatment of administrative issues since I was in Egypt. I'm grateful to* ***Stephan Hermes*** *and* ***Sebastian Mohrhenn,*** *they provided promptly their technical expertise.*

*Last but not least, all my love and thanks to my* ***lovely parents and family*** *for their great support, encouragement during my study and work here alone in Germany. I would like to express my great thanks to my best friend* ***Hend*** *for her support and help from the first day to me in Germany, also my great thanks to my colleagues and friends* ***Dr. Aisha Mostafa*** *(NRC-Egypt) and* ***Dr. Sabbah Ataya*** *(Suez Canal Uni.) for their help and encouragement. I would like to thanks* ***all my friends*** *in Germany and in Egypt.*